UNIVERSITÀ DEGLI STUDI DI PADOVA

Dipartimento di Ingegneria Industriale DII

Corso di Laurea Magistrale in Ingegneria Aerospaziale

Numerical Analysis of Hybrid Rocket Combustion Physics

Analisi Numerica della Fisica della Propulsione a Razzo Ibrida

Relatore: Prof. Francesco Barato

Laureando: Alessandro Rampazzo

Matricola: 2020554

Anno Accademico 2021/2022

Abstract

The objective of this work is to investigate the physics of combustion in hybrid rockets by using RANS simulations run on commercial CFD software (Ansys Fluent) and in particular the role of density in the determination of regression rate in the solid fuel.
Although this technology did important steps in the last decades, many aspects are still not well understood. Here the necessity to conduct a series of virtual experiments, firstly to asses the validity of the employed models, then to extrapolate from the data interesting insights regarding the physics beneath the phenomena in question.
The ability to determine, even only qualitatively, which characteristics of the fuel affect the behavior of the entire system could direct the efforts of the research to a better understanding of the physics or the industry to search for new, highly efficient propellants.
Three types of experiments have been set up: cold-flow isothermal, cold-flow non-isothermal and hot combusting-flow simulations. In the former two the idea that the density of the injected species modify the behavior of the boundary layer has been investigated in a simplified environment.
After a good qualitative understanding of the effect has been built, the work proceed with setting up other simulations of real hybrid rockets to compare the results and prediction of the simplified cases with the ones involving combustion phenomena. The validation of the former two cases has been conducted on the experimental and numerical data provided by Prokein and Wolfersdorf [23], Landis and Mills [15], Romanenko and Kharchenko [24] and Meinert et al. [18]. A good agreement with these data has been found.
The third case, instead, has been verified on the experiments performed at Università Federico II di Napoli by Carmicino and Di Martino ([3], [5], [7]) on two hydrid propulsion systems, one rated 200 N and the other 1 kN, both based on HDPE/HTPB + gaseous oxygen.
For the mesh generation ICEM CFD (Ansys) has been used to create a high quality 2D grid and an UDF (User Defined Function) has been coupled with Fluent to impose the correct boundary conditions to simulate transpiration or blowing.

Sommario

L'obiettivo di questo studio è quello di investigare la fisica della combustione dei razzi ibridi tramite simulationi RANS compiute da un software CFD commerciale (Ansys Fluent), in particolare il ruolo della densità nella determinazione della velocità di regressione dei combustibili solidi. Nonostante questa tecnologia abbia compiuto passi importanti nelle ultime decadi, molti aspetti sono ancora poco compresi. Da qui la necessità di condurre una serie di esperimenti virtuali, prima per assicurarsi della validità dei modelli matematici impiegati, poi per estrapolare dai dati interessanti spunti riguardo la fisica sottostante il fenomeno in questione.
L'abilità di determinare, anche solo qualitativamente, quale caratteristica del carburante influisca sul funzionamento dell'intero sistema potrebbe indirizzare gli sforzi dei ricercatori in comprendere meglio la fisica o l'industria a cercare nuovi ed efficienti carburanti.
Tre tipi di esperimenti sono stati portati a termine: simulazioni a freddo isoterme, non-isoterme e con combustione. Nelle prime due l'idea che la densità della specie chimica iniettata possa avere un'influenza sul comportamento dello strato limite è stata investigata in un caso semplificato. Dopo aver ottenuto una buona comprensione dell'effetto, si è proceduto ad impostare delle simulazioni di veri razzi ibridi per comparare i risultati dei casi con combustione con le predizioni di quelli semplificati.
La validazione delle prime due simulazioni è stata condotta su dati sperimentali e numerici forniti da Prokein e Wolfersdorf [23], Landis e Mills [15], Romanenko e Kharchenko [24] and Meinert et al. [18]. Un buon accordo con questi dati è stato trovato.
Il terzo caso, invece, è stato verificato con test portati a termine all'Università Federico II di Napoli da Carmicino e Di Martino ([3], [5], [7]) su due propulsori ibridi, uno da 200 N e l'altro da 1kN, entrambi basati su HDPE/HTPB e ossigeno gassoso.
Per la generazione della mesh è stato usato ICEM CFD (Ansys) per creare griglie computazionali 2D di alta qualità e una UDF (User Defined Function) è stata accoppiata a Fluent per generare le condizioni al contorno corrette a simulare la traspirazione.

Contents

List of Figures

1 The hybrid technology

1.1 Introduction

Among the many types of chemical endoreactors, three are the main categories: solid-propellant, liquid-propellant and hybrid-propellant rockets.
The former, as the name suggests, employs only propellants in solid phase, often in granular form, where oxidized and fuel are mixed and kept together by a matrix generally of polymeric nature. Solid propellants are all storable at ambient pressure and temperature and for this reason they are largely employed in military circumstances, where the conditions in which the system operates do not allow the use of complex machinery and where simplicity and reliability over efficiency is preferred.
In the second case all propellants are in liquid phase (or gel phase, featuring a liquid in suspension into a solid), they are stored in pressurized dedicated tanks and injected into the combustion chamber where the mixing and combustion process happens. Unlike solid propellants, liquid propellants that are stable at ambient pressure and temperature are harder to find and usually are overcome by cryogenic ones in terms of performances.
In hybrid rockets, instead, one of the two propellants is stored in solid phase (usually the fuel - if not the resulting system is called a reverse hybrid) while the other in liquid form (**Fig. 1**). This case has sparked great interest in the last decades, for it combines the best of the first two technologies in one that could potentially optimally solve many problems in the space industry

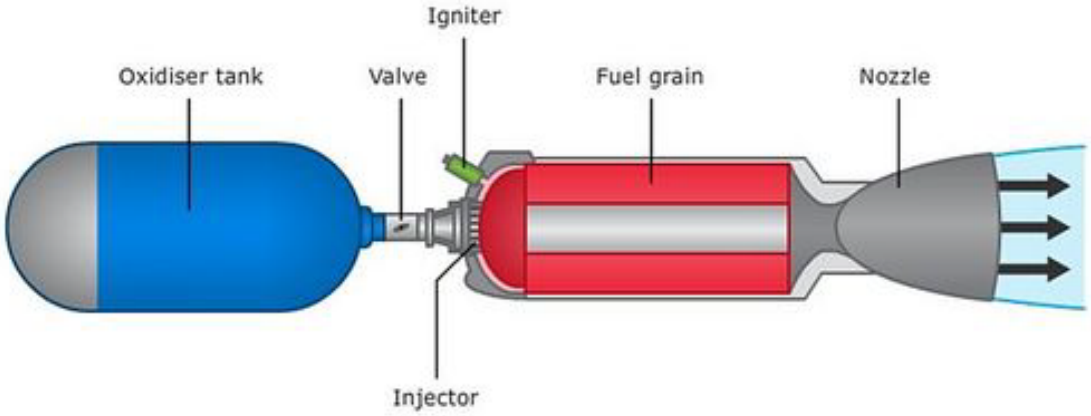

Figure 1. Simplified schematics of a classical hybrid rocket

The main advantages of the hybrid-propellant rocket technology are:

- **Inherent safety**: Most of the fuels used in hybrid rockets are safe to handle, non toxic or harmful to the human body or to the environment, storable at ambient conditions. Unlike solid rocket propellants, they are inert and do not involve oxidizer and fuel already mixed together. This alone ensures that hybrid fuels have an equivalent explosive power of 0.
  In case of an abort, a hybrid engine, like a liquid-propellant one, can be shut down simply by interrupting the flow of liquid oxidizer, while solid rockets must burn all the fuel or be shut down in a semi-catastrophical way, which does not allow successive re-ignitions.
  Grain fracture do not pose a serious problem in hybrid rockets, since the combustion is regulated by fluidodynamic diffusion processes, and not chemical kinetics like solid rockets, which can experience destructive failure if grain cracks appear. Moreover the physics of hybrid combustion if full of negative feedback loops that stabilize the system and make very difficult for a hybrid engine to experience catastrophical failure due to combustion phenomena.

- **Simpler fluidic system**: Having only one propellant in liquid phase halves the amount of pipes, tubes and fluidic elements (valves, pumps, etc.) and simplifies them and the engine diagram.

- **Reliability**: Thanks to the previous two points, the risk of failure of the fluidic system is at least halved. Moreover, as said before, the fuel grain is far more tolerant of defects in its manufacturing process.

- **Cheaper**: Again, thanks to the less complex fluidic system and reduced dry mass a hybrid rocket results in lower costs with respect to a liquid-propellant one. The reliability and inherent safety requires less infrastructures for the propellant and engine management. As said before, the system can tolerate wider design margins, resulting in lower cost.

- **Medium-high specific impulse**: The specific impulse is generally between solid and liquid-propellant rockets (**Fig. 2**), in some cases reaching the latters in terms of performances (**Fig. 3**), especially for doped fuels (with additives like powdered metallic aluminum).

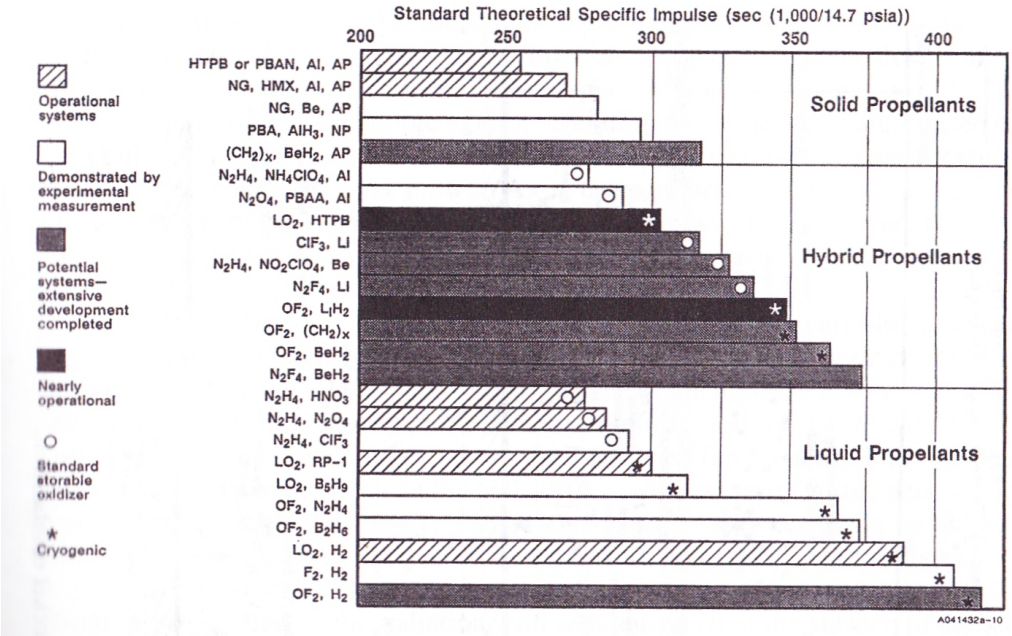

Figure 2. I_{sp} of different propellants belonging to the three main classes of endoreactors

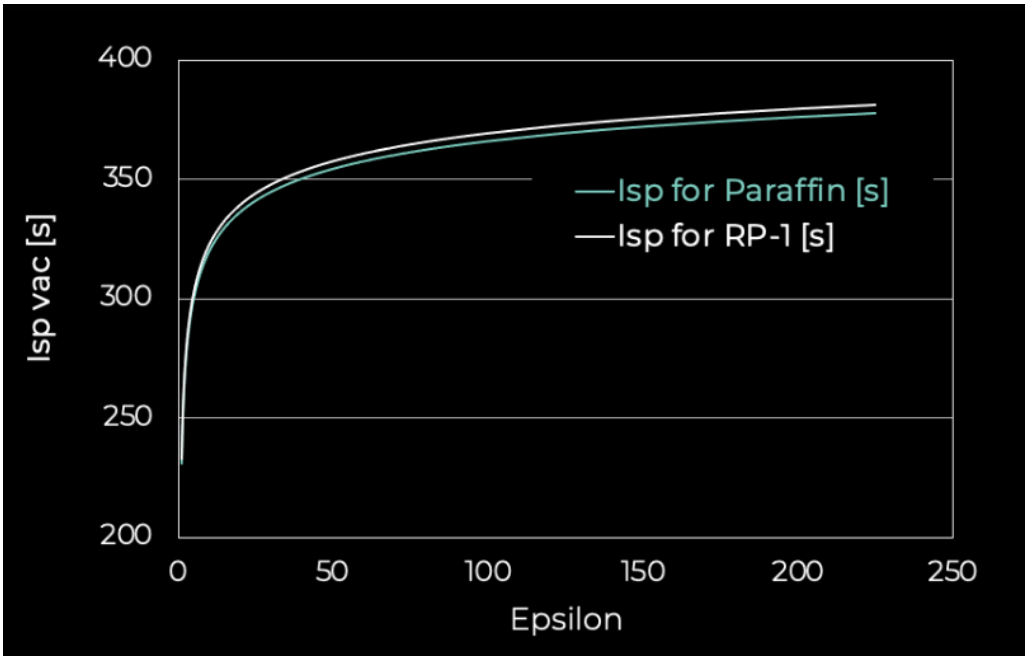

Figure 3. Performances of LOX-Paraffin vs LOX-RP1 [13]

- **Re-ignition**: As said before, hybrid rockets, unlike solid-propellant ones, can be re-ignited in a controlled manner if the system is designed to do so.

- **Throtteability**: It's possible to control the thrust of a hybrid engine simply by acting on the oxidizer flux directed to the combustion chamber.
  Solid rockets cannot be throttled dynamically but they are built at design-time to match a certain thrust profile, which limits their usability in environments where versatility is a fundamental requirement.
  Liquid rockets, on the other hand, can be throttled but the process is much more difficult, for they have to control two different mass flow rates which, in some cases, can depend on each other.

- **Temperature sensibility**: Temperature variation at ignition do not affect heavily the combustion process, unlike solid propellants where small changes in temperature can induce great variations in the combustion velocity of the grain.
  In case of an auto-pressurized system the temperature has anyway an effect on the equilibrium pressure of the propellant in the tank.

- **Propellant versatility**: The propellant choice is generally much wider than liquid propulsion systems, although the research has focused its attention on a limited subset of them. The addition of additives like metallic powders to the solid fuel is easy and do not results in sedimentation, problems for the atomization or for the whole fluidic system like in liquid rockets.

Hybrid rockets, however, do show some drawbacks, most of which are being tested right now for innovative solutions:

- **Low regression rates**: Due to the cited stabilizing negative feedback loops, hybrid rocket motors lie in the low-end spectrum for regression rate, requiring large burning areas and resulting eventually in long combustion chambers and low system performace parameters, like volumetric efficiency. For big hybrid boosters the problem gets worse, as regression rate is much lower and burning time scales slower than thrust does, aggravating the aspect ratio of the grain. Its length, indeed, depends on the thrust while its thickness (web) depends on the burning time.
  Many solutions have been proposed, which range from multiport grains (**Fig. 4**), to new classes of fuels, to additives with the aim to increase artificially the regression rate and other combustive properties.

Multiport grain, however, often add several difficulties like complex design, manufacturing, structural problems, shift in oxidizer-fuel ratio O/F and change of grain port with time, all factors that contribute to a decrease in the accuracy of predictions of the engine behavior and to an increase in the overall cost of the system.

Regarding new fuels, nowadays the research is particularly focused in the so-called "liquefying fuels" such as paraffins. These classes of fuels show an interesting phenomenon called "entrainment" which bypass some of the physics behind the classical hybrid combustion and increase intrinsically the regression rate of the fuel.

Additives, already very famous in solid rocket motors, are being use with increasing certainty and reliability also in the hybrid rocket industry.

However, although several designs featuring some of these solution have been proposed and tested, none has reached the maturity stage and has been used extensively in the commercial sector.

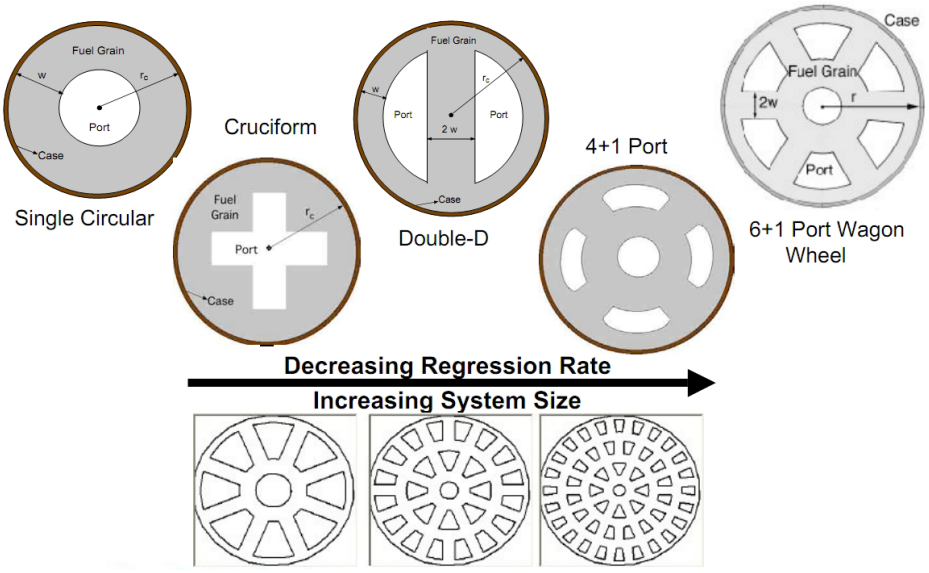

Figure 4. Some examples of multiport grain

- **Low design versatility**: Liquid and solid rockets are relatively versatile in terms of design allowance in their applications. The formers store the liquid propellants in tanks, which can be adapted in size and geometry to fit the specific need.

  The latters, on the other hand, are backed up by an extensive literature that provides several combination of propellants and additives to have full control on the combustion of the grain.

  In hybrids, instead, due to complex (and some still unknown) dependencies between oxidizer mass flux and regression rate, the design constraints, especially for the solid fuel, are particularly tight.

Combining all the parameters to reach a good performance level for the application can be sometimes difficult or leading to combustion chamber length to diameter ratios L/D really high or high performance shifts during operation (i.e. O/F).
In hybrid rockets, for example, fuel mass flow rate can change with time even if the grain is designed to have a constant burning area (star grain is neutral in solid rockets, but strongly regressive in hybrids[21]).

- **Combustion efficiency**: Combustion in hybrid rockets tends to be less complete, leading to greater I_{sp} losses if compared to liquid or solid-propellant propulsive technologies. As said before, using additives can improve the combustion efficiency and lower these losses.

- **Variable** O/F: Keep fixed the O/F at its optimal value is practically impossible, leading to losses that, fortunately, a careful design can contain under a few percentage points.

- **Slower transients**: Initial transient and throttle response is slower in hybrids with respect to liquids. Moreover the combustion chamber internal volume increase with time, reaching the maximum at the end of the burning and overall reducing the accuracy and repeatability of the system.

1.2 Classical theory of hybrid rockets

The classical theory of hybrid rockets was introduced by Marxman et al. in the early 60's and became immediately popular thanks to its inherent simplicity and its capacity to capture the main phenomena in play in a classical hybrid motor.
This theory, however, often fails to predict accurately more complex systems. Anyway it is fundamental for the comprehension of hybrid rocket propulsion and to build a solid base to support further propositions, for this reason a brief introduction has been made in the following paragraphs.

In a classical hybrid motor, as already said before, the pressurized oxidizer is injected into the combustion chamber, where it starts to burn after coming in contact with the fuel grain surface. The combustion happens in a thin flame region inside the boundary layer (**Fig. 5**), which from experimental data and analytical works we know to be about 10% of the boundary layer thickness[28].
This will be essential later on when some expression will be derived assuming

the flame to be infinitely thin, postulate that goes under the name of "flame-sheet hypothesis".

The flame keeps burning because a constant flow of oxidizer from above it comes in contact with a flux of pyrolyzed fuel from underneath. The heat released by the combustion is the source of the energy that drives the decomposition of the fuel, which is injected perpendicular into the main stream. This phenomenon has been called "blowing" and it is the main effect that determines the internal workings of the combustion of a hybrid rocket motor.
The transport phenomena that carry oxidizer and fuel into the flame and regulate it are mainly of diffusive nature, either turbulent (i.e. convective) or molecular (generally less significant than the first). Both of them are determined by the internal fluid dynamics of the engine, unlike in solid rocket motors where, instead, the combustion is regulated by chemical kinetics and it is much more sensible to thermodynamic conditions like initial temperature and chamber pressure.

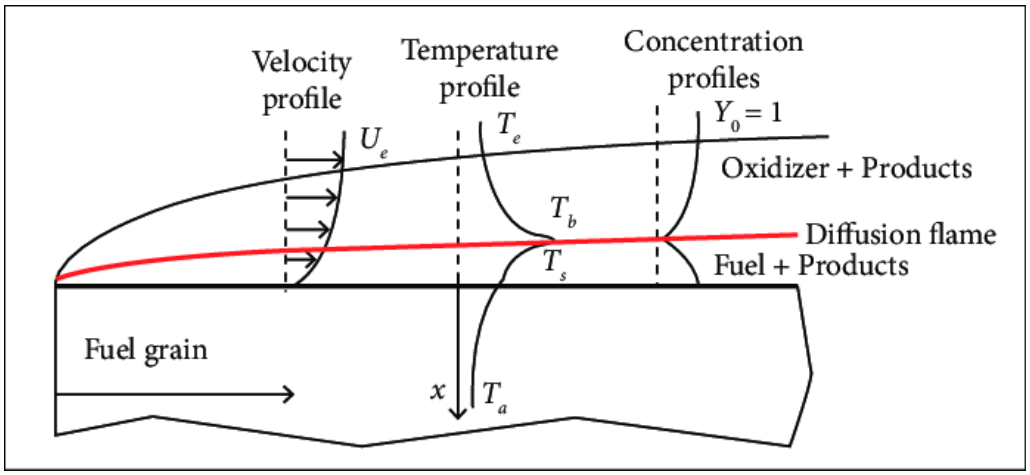

Figure 5. Diagram showing the boundary layer above the fuel grain of a typical hybrid rocket motor[11]

To determine which of these two phenomena is more relevant, an adimensional number called Damkohler Number $Da = \tau_c/\tau_k$ is defined, where τ_c is the characteristic time of convective fluid dynamics while τ_k is the one of chemical kinetics. In most hybrid rockets the $Da >> 1$ assumption is used.
A consequence of postulating that the chemical reactions are infinitely fast is that the flame collapses into a infinitely thin sheet located in the point where the oxidizer-fuel ratio O/F assumes its stoichiometric value, separating abruptly the boundary layer in two zones: beneath-flame fuel-rich zone and above-flame oxidizer-rich zone. The result just obtained, as said before, is compatible with experimental data.

To obtain his theory Marxman started with the following energy balance at the wall:

$$\dot{Q}_w = \dot{Q}_c + \dot{Q}_{in} + \dot{Q}_{rad} \tag{1.1}$$

Where $\dot{Q}_w$ is the total wall heat flux, $\dot{Q}_c$ the heat transferred by convection from the flame, $\dot{Q}_{rad}$ the radiative heat and $\dot{Q}_{in}$ the heat lost by conduction towards the inside the fuel grain. In his first theory Marxman neglects the radiative and conduction heats since they are less relevant than the convective one in normal operative conditions and to simplify the calculations.
If Prandtl Number Pr and Lewis Number Le are assumed to be unitary then the convective term could have been written in the following straightforward way:

$$\dot{Q}_c = -\left(\frac{k}{c_p}\frac{\partial h}{\partial y}\right)_w$$

But for our purposes the following form of equation 1.1 is needed:

$$\dot{Q}_w = \rho_{fuel}\,\dot{r}\,h_v = \dot{Q}_c \tag{1.2}$$

Where the left term associated with the fuel pyrolysis has been developed. $\dot{r}$ is the regression rate and h_v the effective vaporization enthalpy, defined by the formula beneath:

$$h_v = \int_{T_0}^{T_l} c_p(T)\,dT + L_l + \int_{T_l}^{T_v} c_p(T)\,dT + L_v + L_p + \int_{T_v}^{T_w} c_p(T)\,dT \tag{1.3}$$

The effective vaporization enthalpy is basically the total energy required to heat up the fuel, liquefy, pyrolyze and vaporize it, transforming the solid at ambient temperature into the decomposition products which are blown into the combustion chamber. In the balance integrals of specific heats and latent heats L_l, L_v e L_p (fusion, vaporization and pyrolysis latent heats respectively) appear.

Anther hypothesis is introduced by Marxman at this point, the so-called Reynolds

analogy, which states that every boundary layer is similar (for our purposes we only need this for the momentum and enthalpy boundary layers). Sufficient condition for this to happen is that $Pr = 1$. Mathematically this pose the following:

$$\frac{\dot{Q}}{\frac{\partial h_{tot}}{\partial y}} = \frac{\tau}{\frac{\partial u}{\partial y}}$$

Equation that, integrated between wall (*w* for "wall") and flame (*b* for "burning gas"), assuming the velocity of the gas sufficiently low to have $h_{tot} \simeq h$, gives:

$$\frac{\dot{Q}}{\Delta h_{w-b}} = \frac{\tau_w}{u_b}$$

Flipping equation 1.2 and introducing what found in the previous expression we can obtain:

$$\dot{r} = \frac{\tau_w}{\rho_{fuel}\, u_b} \frac{\Delta h_{w-b}}{h_v} = \frac{1}{2} \frac{\rho_e\, u_e^2}{\rho_{fuel}\, u_b} \frac{\Delta h_{w-b}}{h_v} C_f \tag{1.4}$$

Where the wall friction coefficient $C_f = \frac{\tau_w}{\frac{1}{2}\rho_e\, u_e^2}$ has been extracted and where the subscript *e* represents the main external stream.

To predict the C_f of a wall with blowing Marxman then proceeds in the following way:

$$C_f = C_{f0} \frac{C_f}{C_{f0}} = \frac{0.06}{Re_x^{0.2}} \frac{C_f}{C_{f0}}$$

Where C_{f0} is the wall friction coefficient without blowing and Re_x is the Reynolds Number calculated at a distance x from the leading edge of the grain. The expression used in the previous formula was introduced by Pradtl in 1927 and it is widely used in completely developed turbulent flows.
The ratio $\frac{C_f}{C_{f0}}$ is called blowing correction and has been estimated by Marxman with the expression beneath, derived by a momentum balance inside the boundary

layer.

$$\frac{C_f}{C_{f0}} = \left(\frac{ln(1+B)}{B}\right)^{0.8} \left(\frac{1+\frac{13}{11}B+\frac{4}{11}B^2}{(1+B)(1+\frac{B}{2})^2}\right)^{0.2} \tag{1.5}$$

$$B = \frac{u_e}{u_b}\frac{\Delta h}{h_v}$$

B is called thermodynamic blowing parameter and it measures the effectiveness of blowing mass into reducing the friction coefficient. Often, under the assumptions that $Pr = Le = 1$, it is confused with the aerodynamic blowing parameter $B_a = \frac{2\rho_w v_w}{C_f \rho_e v_e}$ for they assume the same value.

If $\frac{\Delta h}{h_v}$ can surely be estimated from the physical properties of the propellant combination, $\frac{u_e}{u_b}$, on the other hand, is less evident. Integrating the oxidizer and fuel mass flow rates, however, Marxman managed to found the following expression for that term:

$$\frac{u_e}{u_b} = \frac{K_{ox_e} + (O/F + K_{ox_e})(\Delta h/h_v)}{O/F\,(\Delta h/h_v)}$$

Where K_{ox_e} is the molar concentration of the oxidizer species in the free stream and O/F the oxidizer to fuel ratio of the flame.

Being the equation 1.5 somewhat complex and difficult to handle, often it is substituted by the following one, generally more accurate for ranges of B of our interests.

$$\frac{C_f}{C_{f0}} = 1.2\,B^{0.77}$$

Then substituting what found in the last steps into equation 1.4, we get:

$$\dot{r} = \frac{1}{2} \frac{\rho_e u_e^2}{\rho_{fuel} u_b} \frac{\Delta h_{w-b}}{h_v} \frac{0.06}{Re_x^{0.2}} 1.2 B^{-0.77} =$$

$$0.036 \frac{\rho_e u_e}{\rho_{fuel}} B \left(\frac{\rho_e u_e x}{\mu_e} \right)^{-0.2} B^{-0.77} =$$

$$0.036 \frac{G^{0.8}}{\rho_{fuel}} \left(\frac{x}{\mu_e} \right)^{-0.2} B^{0.23} \tag{1.6}$$

$$G = \rho_e u_e$$

Where G is the free stream mass flux, which varies along the fuel grain length because mass is added into main stream by the wall.

Marxman then proceeds combining all the constant or slightly variable terms ($\Delta h / h$ is probably independent from Re_x) under a parameter called a_1, giving a much simpler expression:

$$\dot{r} = a_1 G^{0.8} x^{-0.2} \tag{1.7}$$

And finally, applying the spatial-temporal average to the previous equation we obtain the Marxman famous relation for hybrid rockets:

$$\overline{\dot{r}} = a_2 G^n \tag{1.8}$$

Where G, as said before, varies along the grain, but after applying the mean it is taken to be its initial value, i.e the mass flux of oxidizer $G_0 = G_{ox} = \frac{\dot{m}_{ox}}{A_{port}} = 4 \frac{\dot{m}_{ox}}{\pi D_{port}^2}$ to ease the calculations.
a_2, often just called a, is a constant linked to the chosen combination of oxidizer and fuel, as well as the exponent n. As vaguely suggested from equation 1.7: $0 < n < 1$, often for classic combination it assumes values around 0.5 - 0.7.

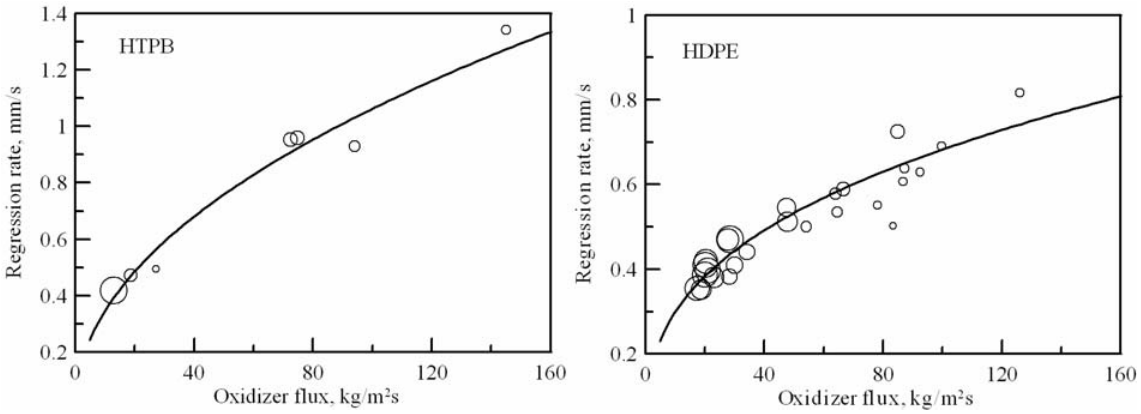

Figure 6. Interpolation of experimental data using the formula 1.8 [5]

Often, however, to have more predictive capabilities and to include phenomena that are not treated by Marxman theory a variation of formula 1.8 is used when interpolating experimental data:

$$\dot{r} = a_2 G^n L^m p^q \tag{1.9}$$

Where similarly to n, m e q are the exponent for the combustion chamber length and pressure (generally 0 < q < 0.5 and m < 0, since bigger motors tend to have lower $\dot{r}$).

There are, however, many more variables and parameters that influence the combustion in hybrid rockets, which can go from the geometry of the injector, to the shape of combustion chamber and fuel grain, to the presence or not of the pre and post-chamber, etc. .
In the next paragraphs some of these factors, especially the most important ones, will be explained briefly to give a wider view of what has been discovered and what has not regarding the hybrid combustion physics.

1.3 Non-ideal effects

1.3.1 Radiation

An effect that Marxman neglects already in the first steps to derive his theory is the radiation contribution to the total wall heat transfer. Despite being treated in a small appendix at the end of his article his model is quite raw and probably not completely correct.

The necessity of this correction is rather important when the combustion chamber conditions are not typical, for example when G is low, since depends on the pressure and it can contribute to a somewhat large fraction of the total wall heat transfer. What Marxman did was to add a grey body radiation term to the regression rate equation 1.6 obtaining [17]:

$$\dot{r} = 0.036 \frac{G^{0.8}}{\rho_{fuel}} \left(\frac{x}{\mu_e} \right)^{-0.2} B^{0.23} + \frac{\sigma \varepsilon_w (\varepsilon_g T_b^4 - T_w^4)}{h_v \rho_{fuel}}$$

Where ε_g is the gas emissivity inside the combustion chamber, ε_w is the one of the wall and σ is the Stefan-Bolzmann constant. This approach, however, does not take into account the strong coupling between heat transfer and blowing effect (called "blocking" effect), i.e. the more heat is absorbed by the grain the stronger will be the blowing of fuel into the main stream, resulting in the flame location to shift away from the wall and reducing the convective heat transfer.
This is one of the cleanest example of negative feedback loops that make a hybrid motor very stable but at the same time very difficult to design it in a high regression rate regime.
Marxman himself realized this and tried to solve the problem in later articles by introducing a corrective factor in this form:

$$\frac{B_{rad}}{B} = 1 + \frac{\dot{Q}_{rad}}{\dot{Q}_c} \left(\frac{B_{rad}}{B} \right)^{0.77}$$

With:

$$\dot{Q}_c = 0.036 G^{0.8} \left(\frac{x}{\mu_e} \right)^{-0.2} B^{0.23} h_v \quad \text{and} \quad \dot{Q}_{rad} = \sigma \varepsilon_w (\varepsilon_g T_b^4 - T_w^4)$$

Which does not have an explicit solution, but it can be adequately approximated by the following expression:

$$\frac{B_{rad}}{B} = e^{1.3 \frac{\dot{Q}_{rad}}{\dot{Q}_c}}$$

Which lead equation 1.6 to the following form:

$$\dot{r} = \frac{\dot{Q}_c e^{-\frac{\dot{Q}_{rad}}{\dot{Q}_c}} + \dot{Q}_{rad}}{h_v \rho_{fuel}}$$

When $\dot{Q}_{rad} << \dot{Q}_c$ the classical formula can be used accepting a small error. When the radiative transfer, one the other hand, is much more relevant and accounts, for example, for the 75% of the total heat transferred the regression rate predicted by equation 1.3.1 is only 35% higher.
This results should be taken with a grain of salt, for the radiative transfer is extremely dependent on the internal geometry of the motor combustion chamber and potentially on other variables neglected by the simplified treatment.

Other researchers have tried to estimate other expressions for the radiative transfer obtaining not better results than Marxman's.
Chiaverini et al. [14] proposes the following formula to keep into account the radiation emitted by soot produced by some types of fuels (HTPB for example) in non negligible amount.

$$\dot{Q}_{rad,soot} = \sigma T_g^4 (1 - e^{-k_s})$$

Where T_g is the themperature of the gas, taken to be 95% of the flame equilibrium temperature at the given O/F ratio and k_s the absorption/emissivity coefficient of the soot, calculated int he following manner:

$$k_s = 0.51 - 0.113\ O/F \tag{1.10}$$

To be noted that this treatment depends mainly on the O/F ratio unlike the previous one where the heat transfer was primarily driven by the pressure (the density and emissivity of a gas are functions of its pressure). Moreover the soot emissivity is an order of magnitude larger than the one of the gas ($\varepsilon_{soot} \sim 0.12 - 0.23$ vs. $\varepsilon_g \sim 0.013 - 0.033$), accounting in some cases more than 80% of the total wall heat transfer.
Chiaverini et al. declares, however, that the equation 1.10 could be not applicable

for different types of fuels, but only for HTPB, since they could show different tendencies for soot production.
Other formulas have been introduced to keep into account the radiation produced by the addition of metallic powders into the grain. Metal, indeed, raise dramatically the soot and particulate emissivity.

Both treatments just explained tend to be not very accurate or specific to certain kinds of combination of propellants, failing to describe the real physics beneath the phenomenon. Anyway, as said before, this effect is negligible for normal conditions, but becomes significant for small values of G (**Fig. 7**), range in which the pressure starts to be have an increasing role in determining the regression rate.

Given the stage of the research, in general the classical formula 1.8 is used and the resulting errors are accepted, shifting the attention to correlating it to experimental data the best it can be done.

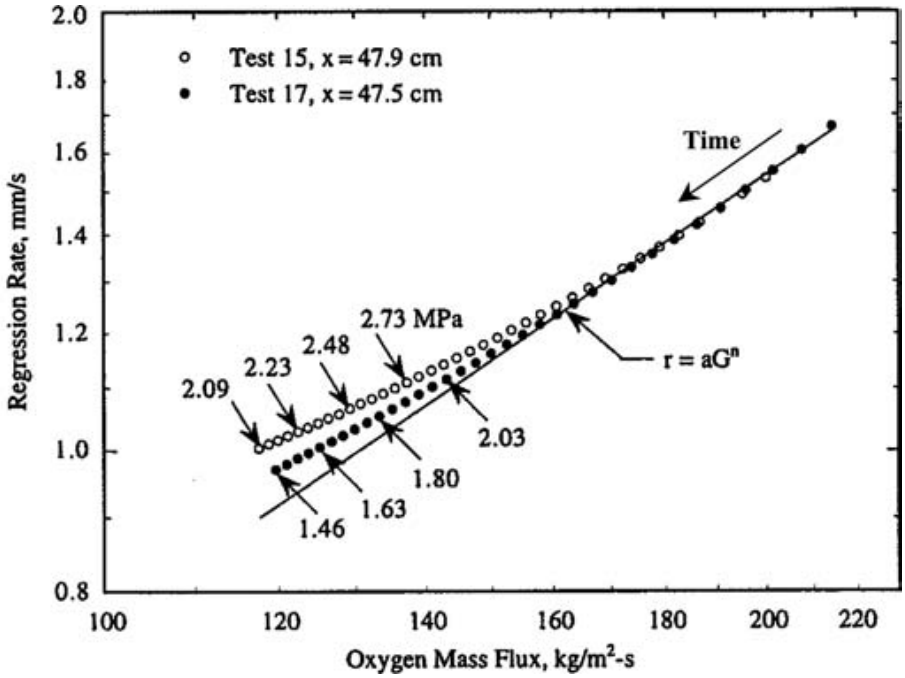

Figure 7. Experimental data vs. classical hybrid rocket formula for regression rate at low values of G [14]

1.3.2 Prandtl Number

Potentially the $Pr = 1$ hypothesis can be relaxed to $Pr = const$, operation that generally is verified for the kind of turbulent stationary flow present into a hybrid rocket combustion chamber. In this case the blowing parameter is modified in as in the next expression [17]:

$$B' = B\,Pr^{-0.67} \tag{1.11}$$

And equation 1.6 becomes:

$$\dot{r} = 0.036 \frac{G^{0.8}}{\rho_{fuel}} \left(\frac{x}{\mu_e}\right)^{-0.2} B^{0.23}\, Pr^{-0.15}$$

For gases and turbulent flows $Pr \sim 1$, so this correction practically always neglected, being Pr raised to the power of -0.15.

1.3.3 Chemical kinetics

Chemical kinetics, assumed infinitely fast in the classical theory, is relevant for high values of G, range in which it becomes the main factor limiting the combustion velocity. In these conditions the chamber pressure starts again to be significant in determining the regression rate, since the speed of a reaction is faster the higher temperature and pressure are. Combining this effect with the one already described regarding radiation heat transfer that dominates the low G regimes we can obtain the qualitative graph below (**Fig. 8**).

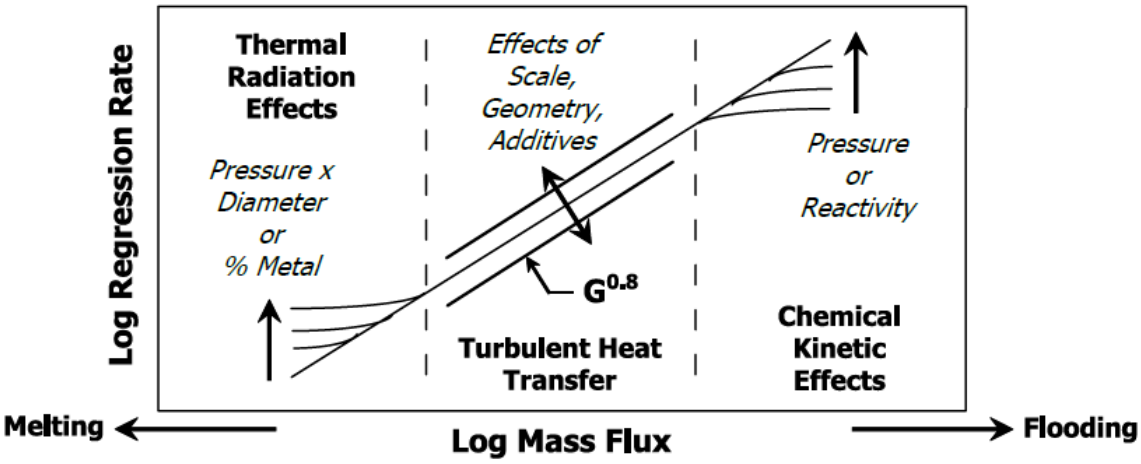

Figure 8. Regression rate in hybrid rockets as a function of G [14]. Three regimes can be distinguished depending on the value of the mass flux

1.3.4 Injection

Another factor that can heavily alter the internal fluid dynamics in hybrid rockets is the injector type. Several geometries have been tested, spanning from simple axial injectors, to swirl or radial injectors (**Fig. 9**) which generally tend to raise the regression rate.

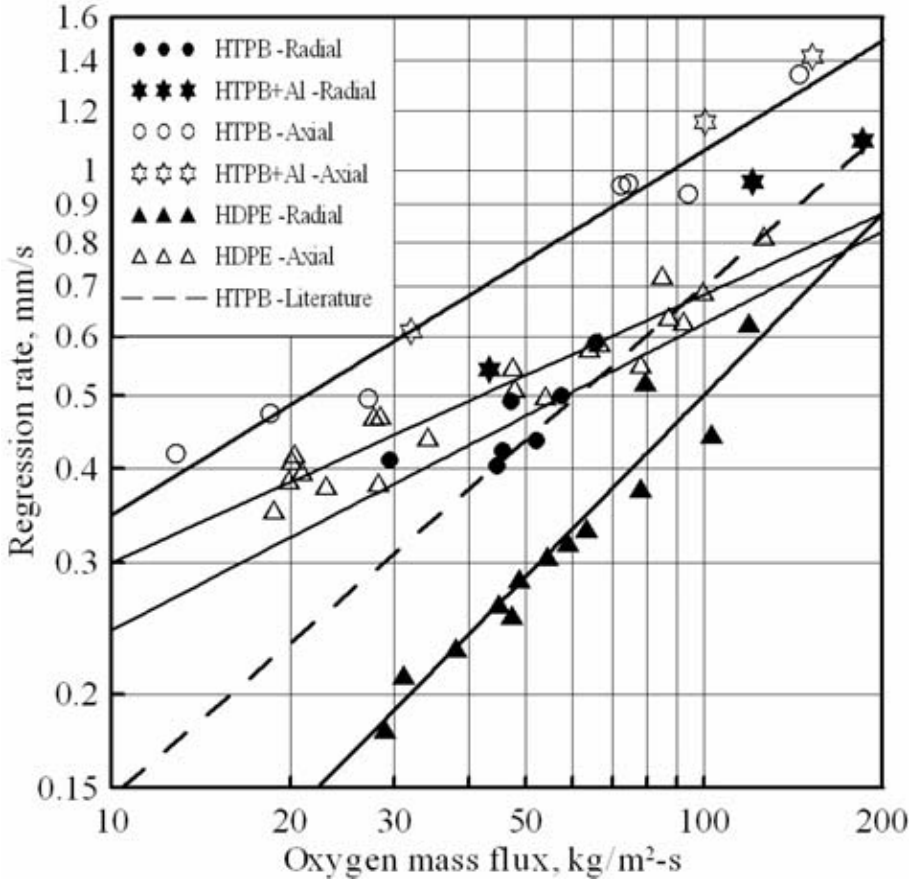

Figure 9. Mean regression rate vs. mass flow rate for different fuels and injectors [5]

An exception seems to be the conical axial injector used by Carmicino and Di Martino in their tests and simulations in [5], [3], [6] and [7]. Despite being axial type, tests showed greatly increased regression rate, probably due to alteration of the fluid dynamic field in the pre-chamber and grain leading edge. Large eddies are created by the free-shear flow right after the injector that contribute heavily to the transport of hot gases near the wall and to the mixing of oxidizer and fuel, raising also the combustion efficiency.

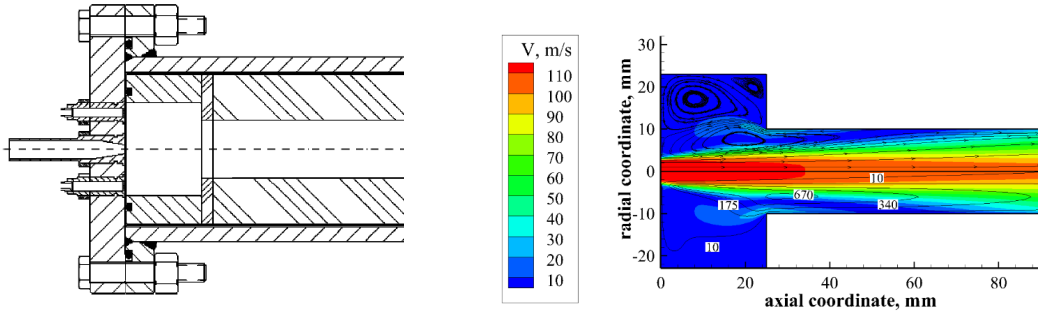

(a) Detail of the Carmicino conical axial injector [4]

(b) Detail showing the CFD analysis of the injector [7]. Two large eddies are clearly visible in the prechamber and near the grain leading edge

Figure 10. Images showing the Carmicino's injector and a CFD analysis of it

1.3.5 Entrainment

Some new discovered fuels like paraffins fall under the class of the so-called "liquefying fuels", which demonstrates a peculiar effect that consists in the phase transition from solid to liquid before being blown into the main stream as a pyrolysis gas. Being exposed to a fast flow of gas, the liquefied fuel starts to produce roll waves and small droplets detach from its free surface, overcoming the flame and burning outside the fuel rich zone (**Fig. 11**).
This droplets do not generate blowing, basically making some of the total fuel mass flow rate bypass the classic negative feedback loop (called the "blocking effect") that limits the regression rate in hybrid rockets. This effect alone can increase the speed at which the fuel burns by a factor of 3-4 with respect to classical polymeric fuels.

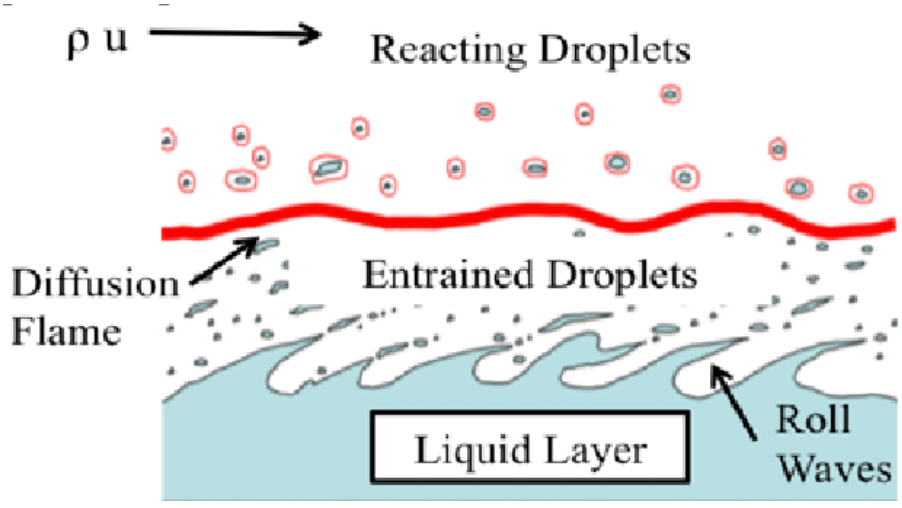

Figure 11. Images showing the entrainment effect [25]

1.3.6 Fluid properties

Another effect often little discussed in literature is the influence of changing fluid properties through the boundary layer thickness on the determination of convective wall heat transfer and regression rate.
Marxman classical theory do not account for this but as his team realized, it could play an important role, being the variation either due to the internal gasdynamics of the engine or to the blowing of decomposition products from the fuel with different molecular properties.

Many researchers, including Chiaverini [14] (pag. 65-69) have identified the variation of the density as a particularly important factor in determining the heat transfer to the wall. According to the classical Marxman theory, two polymeric fuels such as HDPE and HTPB, very similar in terms of physical properties (density of the solid fuel, effective vaporization enthalpy, heat of combustion, etc.), should show similar regression rates given a fixed free stream mass flux G. In fact this is not true: HTPB produces a regression rate almost double with respect to HDPE. To date this discrepancy does not have an official and proven explanation. For this reason the aim of this work is to collect as much data as possible about the matter and try shed some light on the phenomenon, hoping that further down the line someone manages to gather everything under a single and powerful model for hybrid rockets.

Paul et al. [22] have been the first to experimentally investigate the influence of density variation in the boundary layer way back in 1982. The study starts with realizing that the data collected by Wooldridge and Kier [28] about the regression rates of several fuels are too different to be explained by classical theory or any of the proposed corrections.
Subsequently Paul et al. conduct a series of experiments on a rubber based fuel being burned in a free stream of oxygen and nitrogen, finding by interpolation of the data that the exponent of B in the formula 1.6 is 0.5 instead of 0.23, suggesting therefore a stronger dependence of $\dot{r}$ on the blowing parameter.

Finally Paul et al. propose a new theory and a new predictive formula for the regression rate 1.12 (whose derivation will be omitted for brevity) by interpolating the experimental data.

$$\rho_{fuel}\,\dot{r} = 0.056\,G^{0.8}\left(\frac{x}{\mu}\right)^{-0.2}\left(\frac{\rho_b}{\rho_e}\right)^{-0.71}\left(\frac{\rho_w}{\rho_e}\right)^{0.14} B\,(1+B)^{-0.73+0.002\frac{\rho_w}{\rho_e}} \tag{1.12}$$

In the equation above ρ_w, ρ_b and ρ_e are the density at the wall, the one at the flame and the one of the free stream respectively. The strange exponent of $(1+B)$ caused, however, many researchers to raise doubts about its validity and correctness.

Previous failed attempts added corrective terms too, like the following:

$$\rho_{fuel}\,\dot{r} = 0.056\,G^{0.8}\left(\frac{x}{\mu}\right)^{-0.2} B^{0.23}\left(\frac{\overline{\rho}}{\rho_e}\right)^{0.6} \tag{1.13}$$

In which $\left(\frac{\overline{\rho}}{\rho_e}\right)^{0.6}$ can be estimated with a formula omitted for brevity and simplicity (available in [22]).

Because of the specificity of Paul et al. experiments (rubber-based fuel and oxygen-nitrogen free stream is not a common propellant combination) and the strange exponent of $(1+B)$ appearing in the formula 1.13 their results raised doubts in many researchers about the validity and correctness of the work.
Their theory, however, could explain the problem introduced at the beginning of this section. To investigate this, RANS simulations have been set up, first verifying the correctness and applicability of the mathematical models used by comparing the results with pre-existing experimental and numerical data by Meinert et al. [18], Prokein and Wolfersdorf [23], Romanenko and Kharehenko [24], Landis and Mills [15] and then trying to superimpose Paul et al's correction to see if the predictions are plausibile.

The first series of simulation has been conducted on the isothermal injection of different gases in a main stream of air with different blowing rates. For this part we relied upon data from Prokein and Wolfersdorf [23] who set up several tests with helium and argon transpiration backed up by numerical simulations on OpenFOAM.

2 Cold-flow isothermal simulations

2.1 Setup

The setup traces exactly the one employed in [23] (**Fig. 12**), in which a stream of air in a wind tunnel of length 800 mm and cross section 100 x 100 mm sees a perpendicular flow of foreign gas being transpired at about half the domain.
The simulation has been set up in 2D using ICEM CFD to save time and computational resources.

The inlet mass flux has been chosen to be $\rho_e u_e = 85\, kg/sm^2$ to get a comparable velocity ($u_e \simeq 70\, m/s$) with respect to the free stream shown in **Fig. 5** in [23]. The total inlet temperature has been chosen to be $293.15\, K$ but because of the high velocity the static temperature is $290.65\, K$ (anyway $M < 0.2$ to avoid compressibility effects).
All fluid properties have been set up to a constant value and equal to the one built-in in Fluent, since we do not expect great variations of them along the domain.

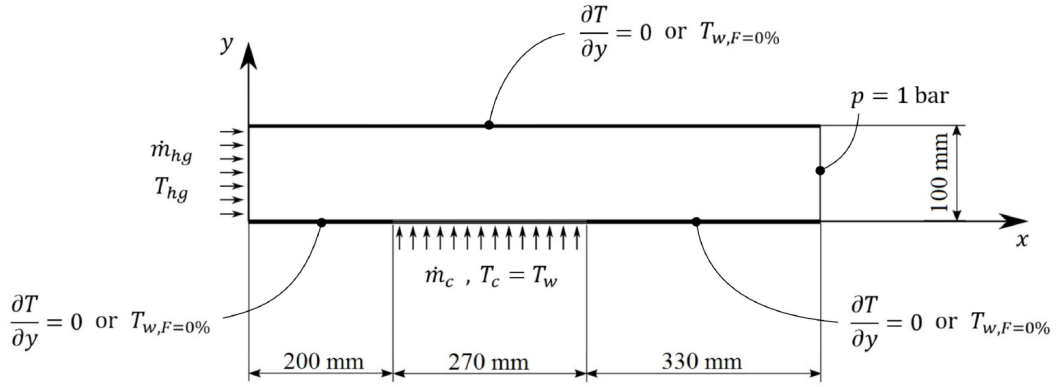

Figure 12. Computational domain and boundary conditions for the selected case [23]

Employed models are the followings:

- **Fluid**: Ideal gas. Although the whole problem is practically incompressibile, the ideal gas model has been used to improve the accuracy of the results and to uniform it to the next batch of simulation where non-isothermal injection is explored.

- **Chemical species**: Fluent's "Species Transport", which generates a scalar field for every chemical species and simulates their convection and diffusion.

- **Turbulence**: $SST\ k-\omega$, and in particular the "Low-Re correction" formulation, developed by Menter et al. [19]. Since its introduction the model has been widely used to simulate very accurately the behavior of the fluid both near and far away from the wall by combining the best of $k-\varepsilon$ and $k-\omega$ models.

The "Coupled" solver and "Second Order Upwind" discretization scheme have been employed.

The following conditions have been set on their respective boundaries:

- **Main inlet** - Mass flux inlet:
  - Mass flux = $85\,kg/sm^2$
  - Species = air
  - Total temperature = $293.65K$
  - Turbulence Intensity = 2% (from [23])
  - Hydraulic diameter = $4\frac{S}{2p} = 0.1$, Where S is the cross sectional area of the duct and $2p$ is its perimeter

- **Outlet** - Pressure outlet:
  - Pressure = 1 bar with "avereage-pressure specification"

- **Side transpirating inlet** - Wall + Source (UDF, see "Mathematical model of injection"):
  - Mass flux = $\rho_{inj}\,v_{inj} = F\,\rho_e\,u_e$, where F is called blowing rate and represents the ratio between the blown mass flux with respect to the main stream mass flux. F is variable from simulation to simulation to adjust the blowing and perform various experiment with different rates.
  - Species = dependent on the simulation
  - Total temperature = $290.65\,K$ (Chosen to be equal to the static temperature of the main stream)

- **Walls** - Fixed wall:
  - Adhesion condition $u_w = 0$
  - Impermeability condition $v_w = 0$
  - Adiabatic $\frac{dT}{dy} = 0$

2.2 Mesh

The computational grid, as said before, has been developed using ICEM CFD, which is an excellent software to build 2D high quality meshes.
Many grids have been tried to find the best one in terms of trade-off between computational speed and accuracy. The end results chosen after a convergence analysis is a structured mesh composed of $\simeq 65'000$ quadrilateral cells, uniform everywhere except for a denser region at the bottom and another one at the top of minor importance. At the former a good grid resolution has been used, with the first cell above the wall being $1\,\mu m$ thick to satisfy the $y^+ < 1$ condition.
At the latter region the grid density has been chosen so to activate the wall functions, which start to be employed by Fluent as soon as $y^+ > 11.225$. From $11.225 < y^+ < 30$ (the so-called "buffer layer"), however, they are not accurate enough to provide a precise modelization of the flow near the wall, so y^+ has been taken $\simeq 100 - 200$

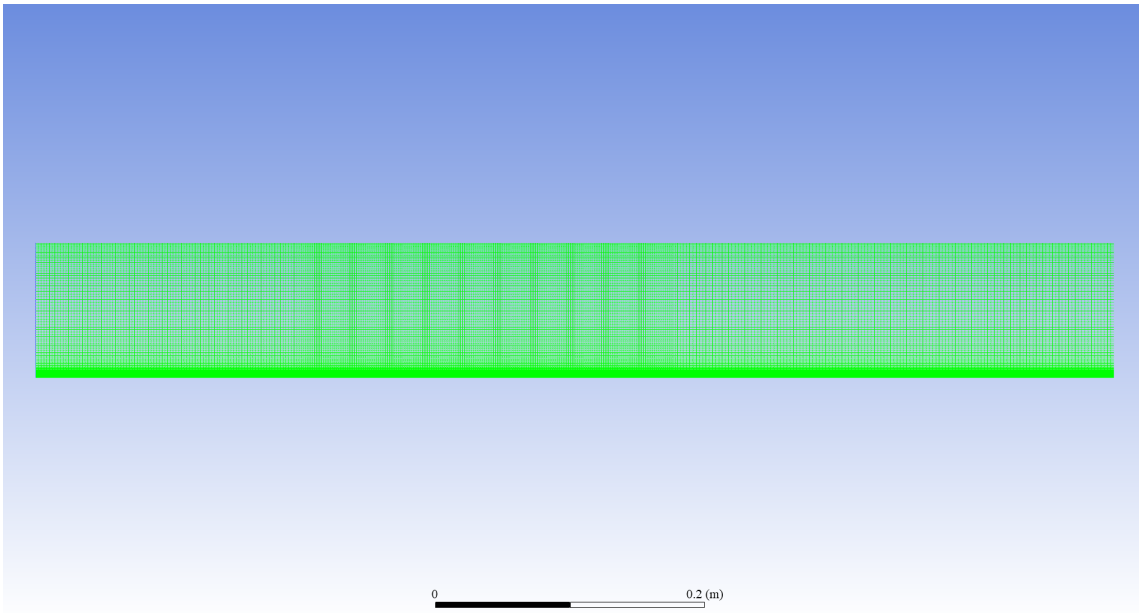

Figure 13. Mesh employed for cold-flow isothermal simulations

2.3 Mathematical model of injection

The side inlet has been modeled, differently from [23] that use a mass flow inlet, as a wall + continuous source (through an UDF). The reasons behind this choice are multiple:

- Defining a wall allows to impose automatically the turbulence boundary conditions for k and ω, contrary to Prokein and Wolfersdorf that, instead, set

manually $k = 0$ and $\omega_{SST} = \frac{6\nu_w}{0.075\Delta y^2}$, with ν_w being the kinematic viscosity at the wall and Δy half of the first cell thickness. This avoids also errors linked the estimation of the kinematic viscosity that is not known a priori, since the species concentration is also unknown, and can depend on the the choice of turbulence boundary condition.

- Turbulence model $SST\ k-\omega$ activates the near-wall treatment using $k-\omega$. At an inlet, however, the matter is doubtful, and to not risk a wrong modelization of the turbulence the safe approach to set a real wall has been chosen.

- The mass flux inlet in Fluent requires to define a mass fraction (or molar fraction) concentration of every chemical species, which, as said before, are unknown a priori. Imposing a mass fraction of the injected species equal to 1 ("Dirichlet" condition) is not feasible, since it will diffuse more of that species into the main flow than physically correct.
  A possible solution to this problem could be the use of another UDF which imposes a "Eckert-Schneider" condition at the boundary to account for the diffusive species trasport near the wall. Mathematically this condition assumes the following form ([6], [23]):

$$\left(\rho\, v\right)_{inj} Y_{w,inj} - \left(\frac{\mu_t}{Pr_t}\frac{\partial Y_{inj}}{\partial n}\right)_w = \frac{\dot{m}_c}{A}$$

  Where Pr_t is the turbulent Prandtl number, A is the injection area and Y_{inj} is the injected species mass fraction. Imposing the Y_{inj} that solves the above equation allows us to simulate correctly the diffusion process into the free stream.
  However, due to numerical problems linked with Fluent, this solution has not been followed. Instead a source at the first cells near the wall has been set up. The temperature at the wall in this model is fixed to be a value defined beforehand.
  All this is much easier to implement and debug since every added term is constant and the UDF does not require to assume Pr_t or invert an equation which needs to access the field data to be solved. To define the sources the following expression have been used:

– **Continuity equation [8]:**

$$\frac{\partial \rho}{\partial t} + \vec{\nabla} \cdot (\rho \, \vec{v}) = S_m \quad \text{with} \quad S_m = \rho_{inj} \, v_{inj}$$

– **Conservation of momentum in y direction [8]:**

$$\frac{\partial (\rho \, v)}{\partial t} + \vec{\nabla} \cdot (\rho \, v \, \vec{v}) = -\vec{\nabla} p + \vec{\nabla} \cdot \vec{\vec{\tau}} + S_v \quad \text{with} \quad S_v = \rho_{inj} \, v_{inj}^2$$

– **Energy conservation [9]:**

$$\frac{\partial (\rho \, E)}{\partial t} + \vec{\nabla} \cdot (\rho \, \vec{v} \, E) = -\vec{\nabla} \cdot (\vec{v} \, p) + \vec{\nabla} \cdot \left(k_{eff} \vec{\nabla} T - \sum_j h_j \vec{J}_j + \vec{\vec{\tau}}_{eff} \cdot \vec{v} \right) + S_h$$

$$\text{with} \quad h_j = \int_{T_{ref}}^{T} c_{p,j} \, dT \qquad E = h - \frac{p}{\rho} + \frac{v^2}{2}$$

$$S_h = \rho_{inj} \, v_{inj} \, E = S_m \, E$$

– **Species transport equation for j-th species in case of "Species Transport" model [10]:**

$$\frac{\partial \rho \, Y_j}{\partial t} + \vec{\nabla} \cdot (\rho \, \vec{v} \, Y_j) = -\vec{\nabla} \cdot \vec{J}_j + R_{Y_j} + S_{Y_j}$$

$$\text{with} \quad S_{Y_j} = \rho_{inj} \, v_{inj} \, Y_j = S_m \, Y_j$$

2.4 Validation

The first step for the validation is to simulate the same case that Prokein a Wolfersdorf [23] conduct for air isothermal injection into a free stream of air with $F = 0.5206\%$

The results displayed as the velocity profile measured at $x = 0.442\,m$ (where the turbulent boundary layer is completely developed) are the following:

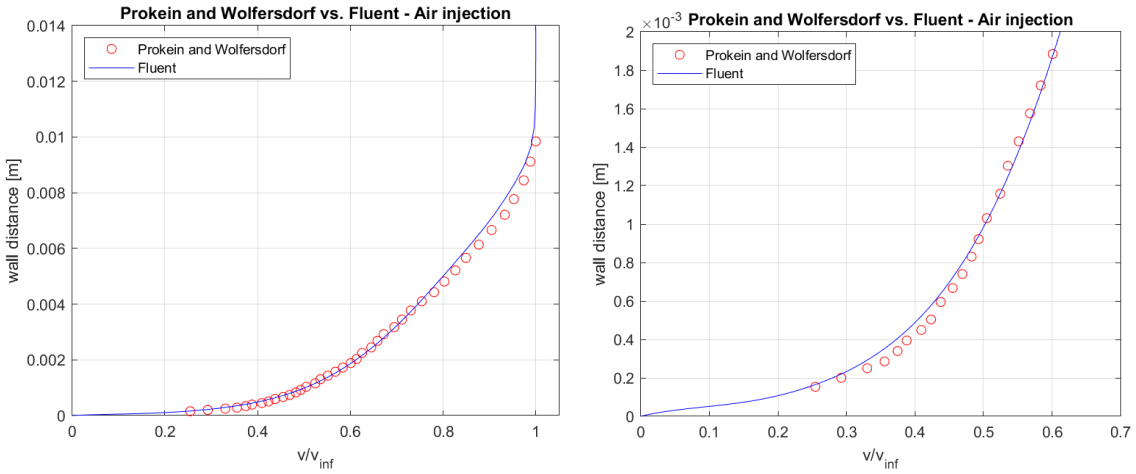

(a) Velocity profile

(b) Detail of the left graph

Figure 14. Velocity profile of a boundary layer with blowing at $F = 0.5206\%$ obtained with Fluent and compared with the experimental data from [23]

While the C_f as a function of x ($C_{f,x}$) over all the bottom wall is:

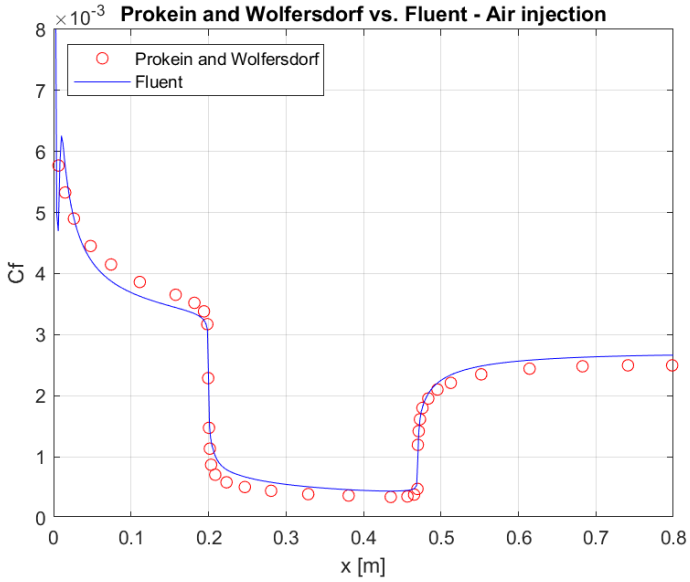

Figure 15. C_f Profile over all the bottom wall with blowing at $F = 0.5206\%$ obtained with Fluent and compared with the OpenFOAM results from [23]

From figures **Fig. 14a** and **Fig. 14b** above we can notice a good agreement with data in velocity profiles. The slight shift can be due to a combination of measurement errors and inherent small inaccuracies of a RANS simulation.
Similarly in **Fig. 15** the results agree with numerical data quite well, this time shifting from them probably because the use of different numerical solvers coupled with different definition of $C_{f,x}$

$$\text{Prokein and Wolfersdorf} : C_{f,x} = 2\frac{\tau_w}{\rho_\infty U_{x,\infty}^2}$$

$$\text{This study} : C_{f,x} = 2\frac{\tau_w}{\rho_\infty U_\infty^2}$$

Where $U_{x,\infty}$ is the free stream velocity at a given x along the duct, while in this work for the calculation of the friction coefficient the inlet velocity U_∞ (at $x = 0\,m$) has been used basically for simplicity. The viscous shear stress in both cases is:

$$\tau_w = \mu_w \left(\frac{\partial u}{\partial y}\right)_{w,x}$$

After terminating the validation on isothermal blowing of air the work proceeds by simulating transpiration of foreign gases. In this case argon and helium and as before at the same temperature of the free stream to limit the influence of heat transfer. The results (collected at $x = 0.442\,m$) are shown here in **Fig. 16a** e **Fig. 16b**.

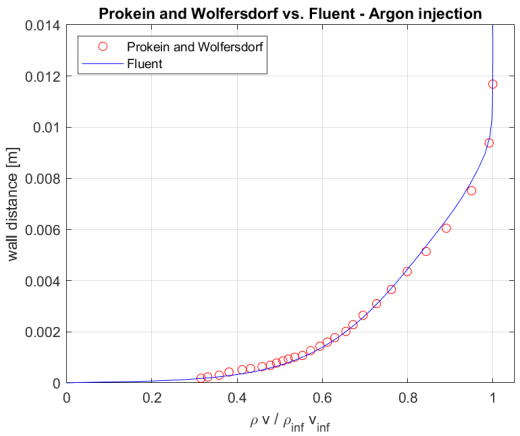

(a) Comparing the mass flux profiles for argon injection at $F = 0.5570\%$

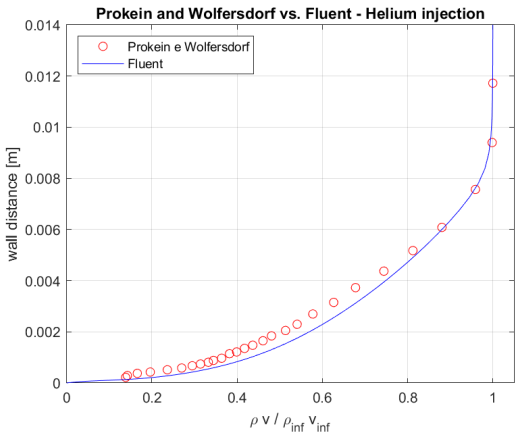

(b) Comparing the mass flux profiles for helium injection at $F = 0.0852\%$

Figure 16. Validation of mathematical models for isothermal injection of helium and argon into a free stream of air

For foreign gas injection we obtain good results as well if compared to the experimental data, showing that the injection model is accurate enough to simulate the physics behind this phenomenon, allowing us to proceed and analyze more complex cases.

2.5 Wall shear stress analysis

To validate and explore the general behaviour of the boundary layer for different blowing rates, other simulations have been set up changing the F parameter. The characteristics of the main stream have been kept like in the previous simulations, allowing to minimize discrepancies eventually linked to the variation of Re. Freon12 (CCl_2F_2) was added to these cases to have a wider range of molecular masses (and as a consequence densities) and collect more complete data.

Some results are shown in the following images (as always, sample distance is $x = 0.442\,m$ from inlet):

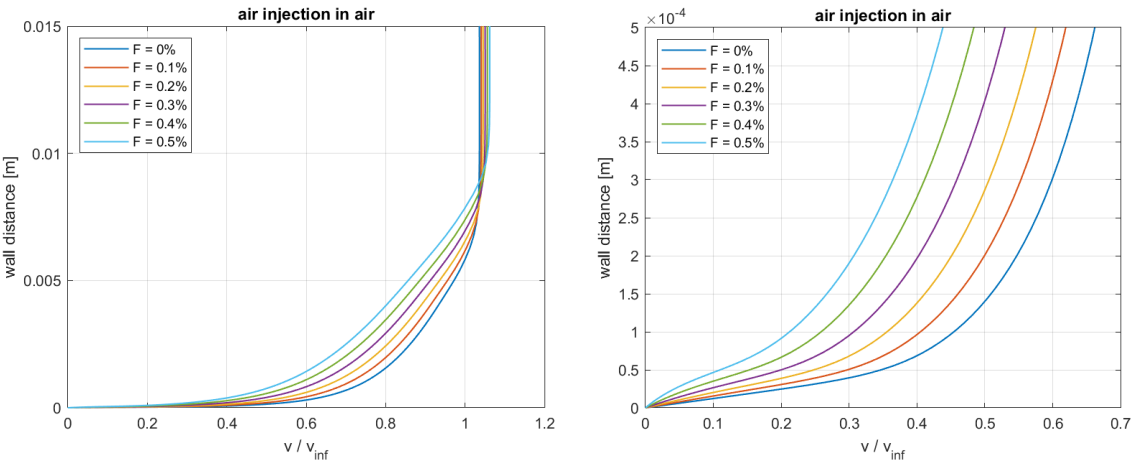

(a) Velocity profiles

(b) Detail of the left graph

Figure 17. Velocity profiles for air injection in a main stream of air

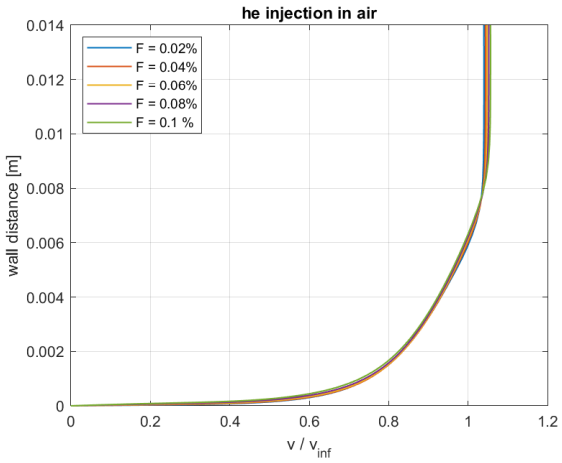

(a) Velocity profiles

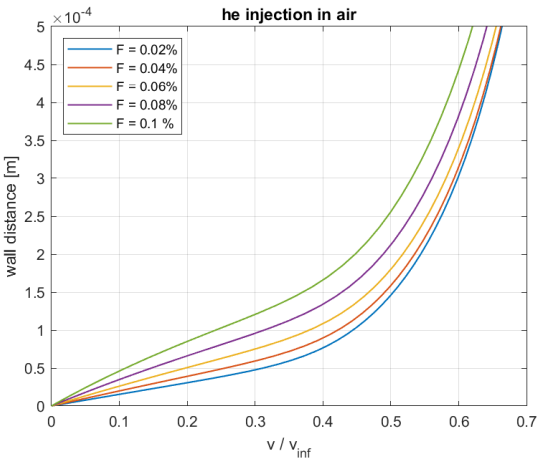

(b) Detail of the left graph

Figure 18. Velocity profiles for helium injection in a main stream of air

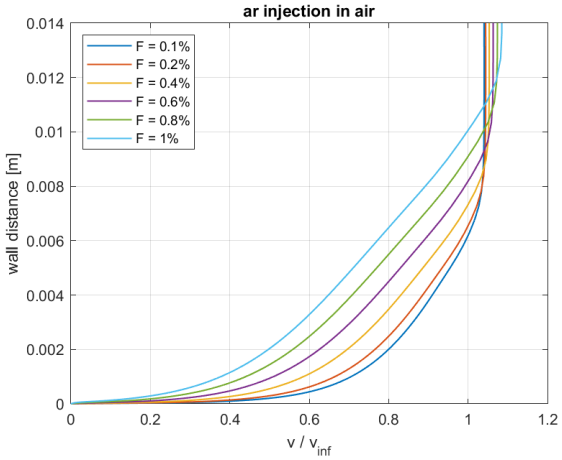

(a) Velocity profiles

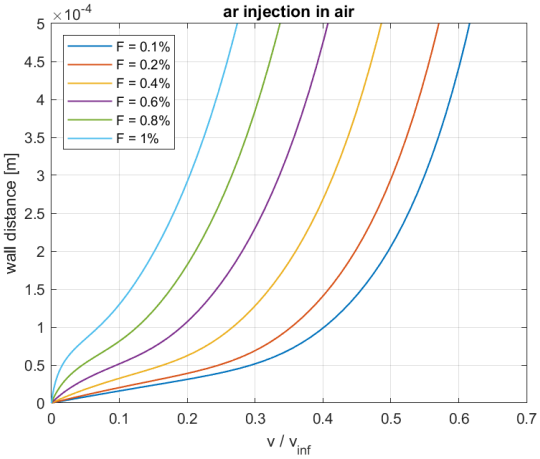

(b) Detail of the left graph

Figure 19. Velocity profiles for argon injection in a main stream of air

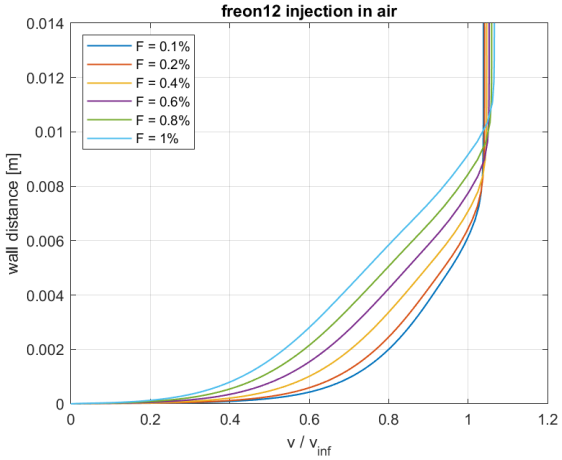

(a) Velocity profiles

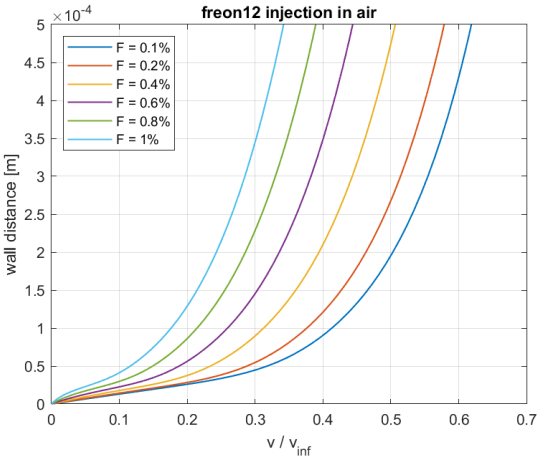

(b) Detail of the left graph

Figure 20. Velocity profiles for freon12 (CCl_2F_2) injection in a main stream of air

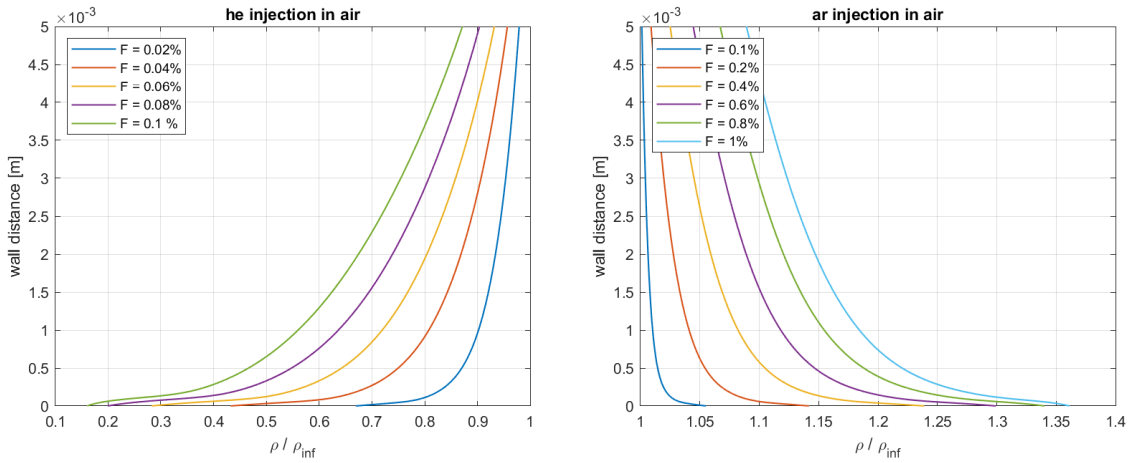

(a) Density profiles for helium injection

(b) Density profiles for argon injection

Figure 21. Some density profiles with varying F and gas injection

From above graphs we can extrapolate some important observation. First of all by increasing F the velocity profile tends to slow down, coupled with an increase in thickness of the boundary layer, although hardly visible in some graphs due to the superposition of multiple lines.
Another, less intuitive, aspect is the small acceleration of the free stream flow, present in all of the above figures. The velocity in the core, indeed, reach a value which is slightly higher than u_∞.
After a careful analysis, however, this appears to be expected. Since the boundary layer slows down and increase in thickness, the external flow must accelerate to met the conservation of momentum and mass.
The main flow acceleration also is proportional to the blowing strength. This effect has been observed in external aerodynamics too.
Another subtle detail we observe is that the blowing, be it of foreign gas or the same species of the main flow, introduce a flex into the velocity profile. This flex increase in intensity by raising F and reduces strongly the wall friction coefficient (proportional to the derivative of v at $y = 0$).

Lastly is interesting to see the effect of different gases being blown at the same F. In the above analysis the F range has been chosen to match the wider interval that didn't lead to the boundary layer separation ("blow-off" happens when $\frac{\partial u}{\partial y} \sim 0$) already suggesting a different influence of these substances on the flow.

In the figure below some profile have been compared at $F = 0.4\%$ for air, argon and freon12 injection (blowing helium at $F = 0.4\%$ lead indeed to blow-off and data were not relevant anymore to the current analysis).

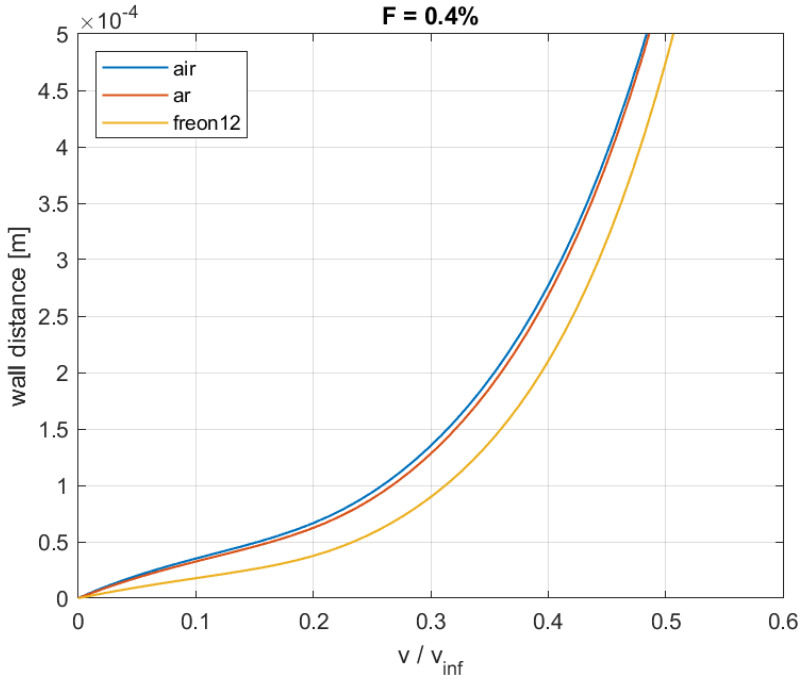

Figure 22. Comparing different velocity profiles when blowing air, argon and freon12 at $F = 0.4\%$ in an air free stream

Although only three data points have been compared, we can clearly see a trend: given an F, blowing heavier gases (in terms of density or mean molecular mass) tend to have smaller effects on the boundary layer and viceversa.

Many researchers ([15], [18], [23], [24]) tried to investigate the phenomenon, and discovered that it is particularly evident when plotting the $\frac{C_f}{C_{f0}}$ vs. $2\frac{F}{C_{f0}}$ graph, where C_{f0} is the friction coefficient without blowing, all other conditions being equal. The abscissa has been chosen this way to remove possible dependencies on the geometry of the problem between different tests.
The cited diagram has been plotted for the four previous cases and superimposing data from Prokein and Wolfersdorf [23], Meinert et al. [18], Romanenko and Kharehenko [24], Landis and Mills [15] obtaining a good agreement, except for freon12, for which, however, physical properties and main stream velocity (and related compressibility effects) may differ from author to author (and indeed its spread is much grater than, for example, helium).
Romanenko and Kharehenko, moreover, collected their data for non-isothermal injection in a pre-heated main flow.

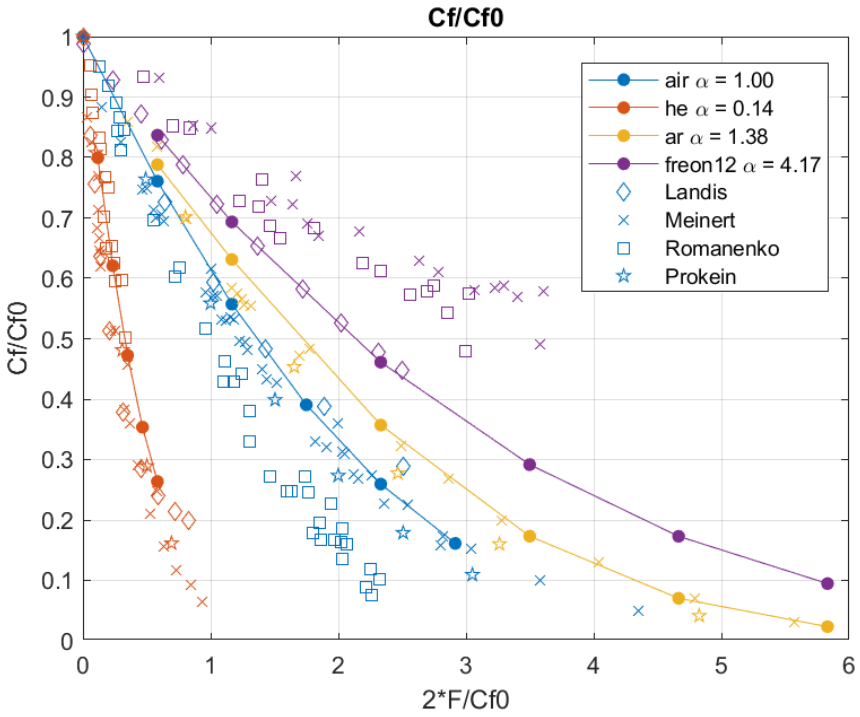

Figure 23. $\frac{C_f}{C_{f0}}$ from Fluent compared with different authors. $\alpha = \frac{MM_{blowing}}{MM_{stream}}$

From figure **Fig. 23** we can see in the most clear way the different effect of foreign gas injection on the wall friction coefficient. Lighter gases with respect to the main flow, such helium in air, reduce greatly the C_f if compared to heavier substances.

This could explain the reason two polymeric fuels such as HTPB and HDPE could display such different regression rates. They, indeed, tend to decompose into their respective fundamental monomers, which in the case of HDPE, as its acronym suggests (High Density PolyEtyhlene), is ethylene C_2H_4. Similarly butadiene C_4H_6 should be the main decomposition product of HTPB (Hydroxil Terminated PolyButadiene **Fig. 24**).

Even in the case they do not decompose into the just described way, the carbon and hydrogen atoms conservation impose that for every heavy species, a lighter one must be created. This law enforces the mean molecular weight of the decomposition products to be around the molecular mass of the fundamental monomer of the fuel.

Following this theory, we can compare the molecular masses of butadiene and etilene and obtain a ratio very close to 2, when the ratios between the regression rates of the two fuels is somewhere between 1.5 and 2.1 (**Fig. 25a**, **Fig. 25b**)[29]:

$$\frac{MM_{C_4H_6}}{MM_{C_2H_4}} = \frac{54}{28} = 1.9286 \qquad 1.5 \lesssim \frac{\dot{r}_{C_4H_6}}{\dot{r}_{C_2H_4}} \lesssim 2.1$$

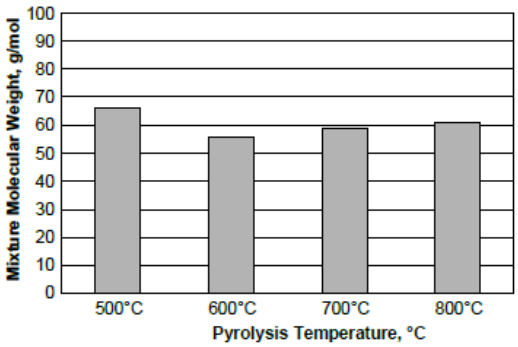

Fig. 12 HTPB pyrolysis product mixture molecular weight vs. temperature.

Table 2 HTPB pyrolysis product mass fraction vs. temperature

Major pyrolysis product species M_i, chemical formula	Heat of formation ΔH_f^o, J/g	Mass fractions of pyrolysis products at various temperatures, K			
		773	873	973	1073
Ethene, C_2H_4	1865.69	——	5.59	3.05	6.58
Propene, C_3H_6	485.49	——	——	4.90	10.99
1,3–Butadiene, C_4H_6	2037.27	77.4	89.06	66.1	41.07
3–Pentene–1–Yne, C_5H_6	2119.82	——	——	9.20	10.28
Benzene, C_6H_6	1062.29	——	——	10.3	22.02
Toluene, C_7H_8	542.97	——	——	6.41	9.06
4-Vinyl–cyclohexene, C_8H_{12}	280.78	22.6	5.35	——	——

Figure 24. Decomposition products and mean molecular mass of HTPB by Chiaverini [14] pag. 69

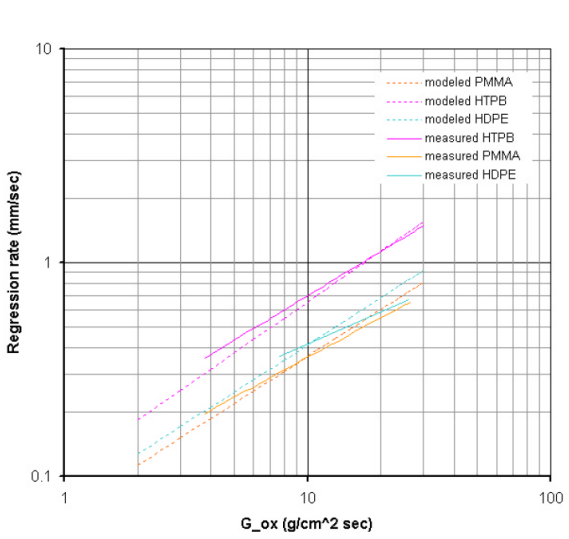

(a) Measured regression rates vs. Modeled regression rates by Zilliac e Karabeyoglu [29]

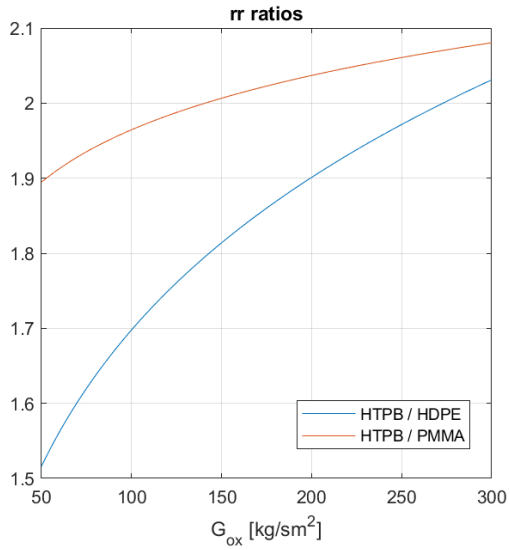

(b) Ratio between measured regression rates of the fuels from the left graph

Figure 25. Regression rates of HTPB, HDPE and PMMA by Zilliac e Karabeyoglu [29]

From the figure **Fig. 25b**) we observe that HTPB has a regression rates almost double with respect to PMMA (PolyMetilMetAcrylate) too, another less common hybrid rocket fuel. PMMA is the polymer of Metil Metacrylate ($C_5O_2H_8$), which is a extremely heavy monomer. However, is contains a non-negligible amount of oxygen, which at decomposition could help generate lighter products such as H_2O or CO_2, lowering the density of the injected gas. Lacking of reliable data regarding the PMMA pyrolysis this hypothesis has not being investigated further.

The phenomenon is, however, far from being so simple and several factors may play a role in determining the difference in regression rate (one of them could be the higher tendency of HTPB to soot production and increase radiation heat transfer as a consequence [14]). These data suggests nonetheless a non-trivial correlation. In the next paragraphs and chapters we will collect more data on the matter and we will try to validate this hypothesis in other contests.

2.6 Other simulations

Before proceeding however, other blowing simulations with varying F have been set up to extend the domain of this analysis. In particular two other batches were made:

- Injection of *airh* ($MM = 4 \cdot MM_{air}$) and *airl* ($MM = 0.25 \cdot MM_{air}$). These fictitious substances have all the other properties equal to the air to see if molecular viscosity, for example, interferes with the effect.

- Injection of C_2H_4 and C_4H_6 into a main stream of oxygen to compare the results with the later simulations of rockets.

All the data are displayed in **Fig. 26** and **Fig. 27**:

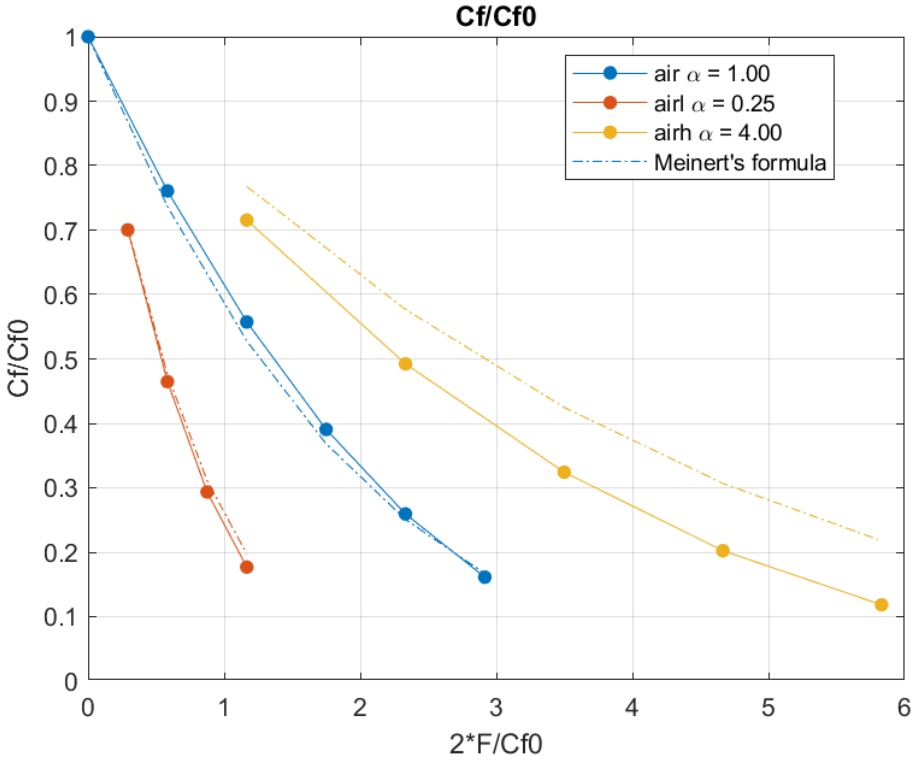

Figure 26. Light air (*airl*) and heavy air (*airh*) injection in an air main stream

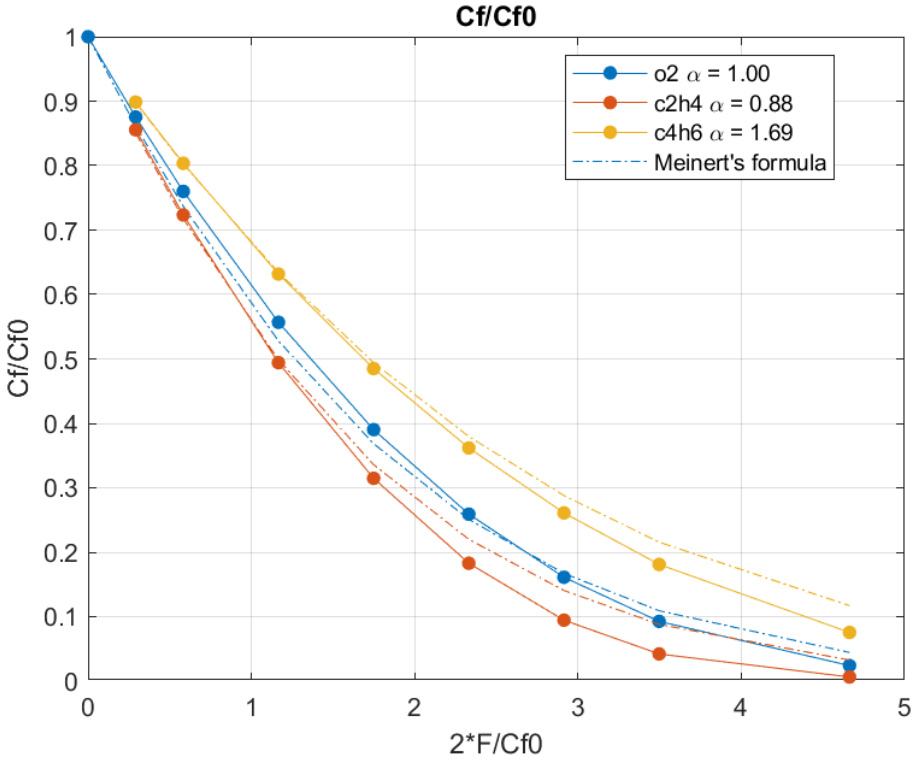

Figure 27. Ethylene C_2H_4 and butadiene C_4H_6 injection in an oxygen main stream

In which the Meinert's formula [18] has been superimposed for comparison, given the fact that no other experimental or numerical data are available for these cases.

The cited formula in case of isothermal transpiration is the following [18]:

$$\frac{C_f}{C_{f0}} = \frac{\frac{2F}{C_{f0}} k_M}{e^{\frac{2F}{C_{f0}} k_M} - 1}$$

Where $k_M = (\frac{MM_\infty}{MM_{inj}})^{0.6}$ is the ratio between the molecular mass of the main stream vs. the blown gas. Meinert uses an exponent of 0.8, however in our case the ratio raised to the power of 0.6 interpolated better the data.

As shown the two images above, the model predicts with acceptable accuracy until $\frac{C_f}{C_{f0}}$ drops under about 0.3, where the blow-off of the boundary layer start to be an issue. The only exception being *airh* which for some reason Fluent gives lower C_f than predicted by Meinert's formula (or viceversa).

Moreover, from the first batch we excluded the possibility that other fluid properties such as viscosity could play a role into determining the observed reduction of friction coefficient. From the second batch, instead, we verified the independence from the substance of the main flow (which, however, seems to slightly alter the behaviour for high blowing rates since the difference between Fluent's data and Meinert's formula are higher for the oxygen free stream).

The previous case shown in **Fig. 23** was compared similarly with this formula and similar results were obtained, which are not displayed for brevity (the curves are equivalent to Meinert's data points).

3 Cold-flow non-isothermal simulations

Continuing the foreign gas injection simulations, the case of non-isothermal injection has been set up. The reason for this is that the regression rate in hybrid rockets does not depend really on $\frac{C_f}{C_{f0}}$ as equations 1.4 and 1.5 could suggest, but rather on $\frac{S_t}{S_{t0}}$, where S_t is the Stanton Number, defined in the following way:

$$S_t = \frac{\dot{Q}_c}{\rho_b \, u_b \, \Delta h}$$

With $\dot{Q}_c$ the wall convection heat transfer and Δh the difference in enthalpy between the free stream (flame in case of hybrids) and wall.
In the classical theory the friction coefficient ratio is used because the Reynolds analogy allows it. But it is an assumption after all, even if widely used in the field, especially the general form involving a corrective factor based on the Prandtl Number (1.11).
The regression rate equation would appear in this form:

$$\dot{r} = \frac{\rho_b u_b}{\rho_f} \frac{\Delta h}{h_v} \frac{St}{St_0} St_0$$

In this chapter we will explore the influence of the temperature and if the assumption $\frac{S_t}{S_{t0}} \simeq \frac{C_f}{C_{f0}}$ holds by employing a setup similar to the one used in previous chapter, but involving a heated main flow to study the heat transfer as described in [23].
Similarly to before, we will start by validating the mathematical models comparing the results with the same authors as the previous chapter and proceed to analyze the data of wall shear stress and wall heat transfer.

3.1 Setup

The fluid domain and computational grid for this series of simulations are the same of isothermal ones. The air main flow temperature has been chosen to be $300\,°C$ and the side porous wall has been set to $25\,°C$ as well as the injected gas.
The temperature of the transpirating wall should be determined by the simulation, imposing a certain thermal resistance between the interior of the duct and the exterior. This however couldn't be done without assuming an arbitrary value for the resistance, so putting no resistance at all has been preferred (setting the temperature directly to the exterior, i.e. $25\,°C$). This shouldn't alter heavily the Stanton Number ratio, since it is adimensionalized with the enthalpy difference.
The mass flux $\rho_e\, u_e$ has been reduced to $40\,kg/sm^2$ to avoid compressibility effects ($M > 0.2$).

All other mathematical models are the same, except for the physical properties that have been assumed variable with temperature with the law presented below, some obtained by Fluent database and other by interpolating data from NIST [20]. All the following formulas are valid in the interval $273.15\,K \div 1000\,K$ and the unit of measure are J/kgK, kg/ms and W/mK respectively for C_p, μ and λ.

- **Air**:

$$\begin{aligned} C_p = 1161.482 &- 2.368819\,T + 0.01485511\,T^2 - 5.034909\cdot 10^{-5}\,T^3 \\ &+ 9.92857\cdot 10^{-8}\,T^4 - 1.111097\cdot 10^{-10}\,T^5 \\ &+ 6.540196\cdot 10^{-14}\,T^6 - 1.573588\cdot 10^{-17}\,T^7 \end{aligned}$$

$$\mu = \mu_0 \left(\frac{T}{T0}\right)^{\frac{3}{2}} \frac{T0 - S_\mu}{T - S_\mu} \qquad T0 = 273.11\,K \qquad S_\mu = 110.56\,K$$

$$\mu_0 = 1.716\cdot 10^{-5} Pa\cdot s$$

$$\begin{aligned} \lambda = -6.43678\cdot 10^{-4} &+ 1.08844\cdot 10^{-4}\,T - 7.55315\cdot 10^{-8}\,T^2 \\ &+ 4.6561210^{-11}\,T^3 - 1.15844\cdot 10^{-14}\,T^4 \end{aligned}$$

- **Argon**:

$$C_p = 5.32104 \cdot 10^2 - 7.87593 \cdot 10^{-2}\, T + 2.20657 \cdot 10^{-4}\, T^2 - 3.12325 \cdot 10^{-7}\, T^3 + 2.20115 \cdot 10^{-10}\, T^4 - 6.13995 \cdot 10^{-14}\, T^5$$

$$\mu = 8.72874 \cdot 10^{-7} + 8.46321 \cdot 10^{-8}\, T - 4.30911 \cdot 10^{-11}\, T^2 + 1.33075 \cdot 10^{-14}\, T^3$$

$$\lambda = 6.31225 \cdot 10^{-4} + 6.67018 \cdot 10^{-5}\, T - 3.43142 \cdot 10^{-8}\, T^2 + 1.05901 \cdot 10^{-11}\, T^3$$

- **Helium**:

$$C_p = 5193.1$$

$$\mu = 4.16888 \cdot 10^{-6} + 6.06934 \cdot 10^{-8}\, T - 3.12662 \cdot 10^{-11}\, T^2 + 1.33336 \cdot 10^{-14}\, T^3$$

$$\lambda = 3.01283 \cdot 10^{-2} + 4.88739 \cdot 10^{-4}\, T - 2.65744 \cdot 10^{-7}\, T^2 + 1.14089 \cdot 10^{-10}\, T^3$$

- **Freon12**:

$$C_p = 1.06137 \cdot 10^3 - 8.65692\, T + 4.96790 \cdot 10^{-2}\, T^2 - 1.24987 \cdot 10^{-4}\, T^3 + 1.51788 \cdot 10^{-7}\, T^4 - 7.27125 \cdot 10^{-11}\, T^5$$

$$\mu = -2.02923 \cdot 10^{-6} + 5.14943 \cdot 10^{-8}\, T - 1.73501 \cdot 10^{-11}\, T^2 + 9.71442 \cdot 10^{-16}\, T^3$$

$$\lambda = -1.83270 \cdot 10^{-3} + 2.43886 \cdot 10^{-5}\, T + 6.91157 \cdot 10^{-8}\, T^2 - 6.14941 \cdot 10^{-11}\, T^3$$

3.2 Validation

Before proceeding, a validation has been conducted, as before, on data provided by Prokein and Wolfersdorf [23] for non-isothermal injection of argon and helium in a heated stream of air respectively at $456\,K$ and $550\,K$. Results have been normalized on free stream values to remove small errors that could be caused by slight differences in boundary conditions (some of them have been estimated by graphs in Prokein and Wolfersdorf's paper)

The cited validation is the following:

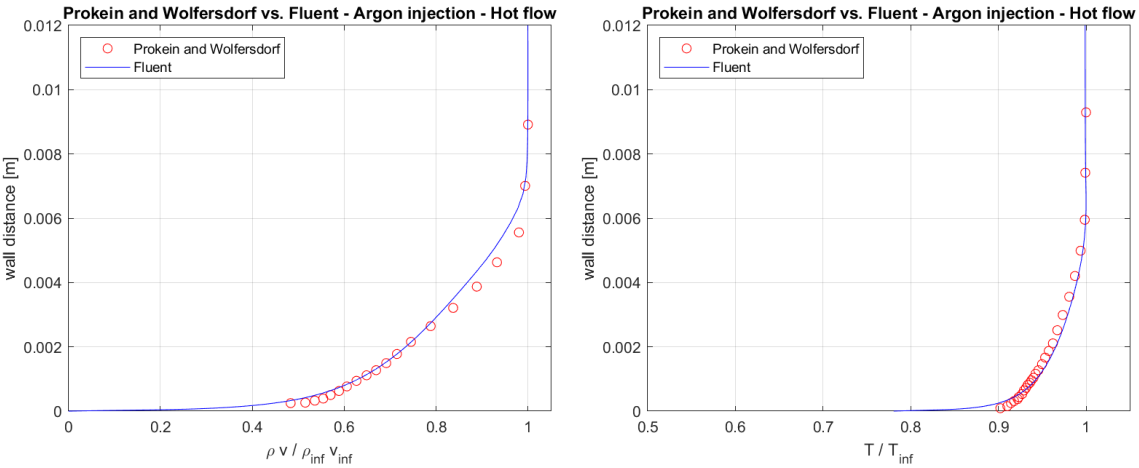

(a) Comparison between mass flux profiles for argon injection at F=0.5342%

(b) Comparison between temperature profiles for argon injection at F=0.5342%

Figure 28. Validation of mathematical models for non-isothermal blowing of argon in a heated main stream of air collected at $x = 0.342\,m$

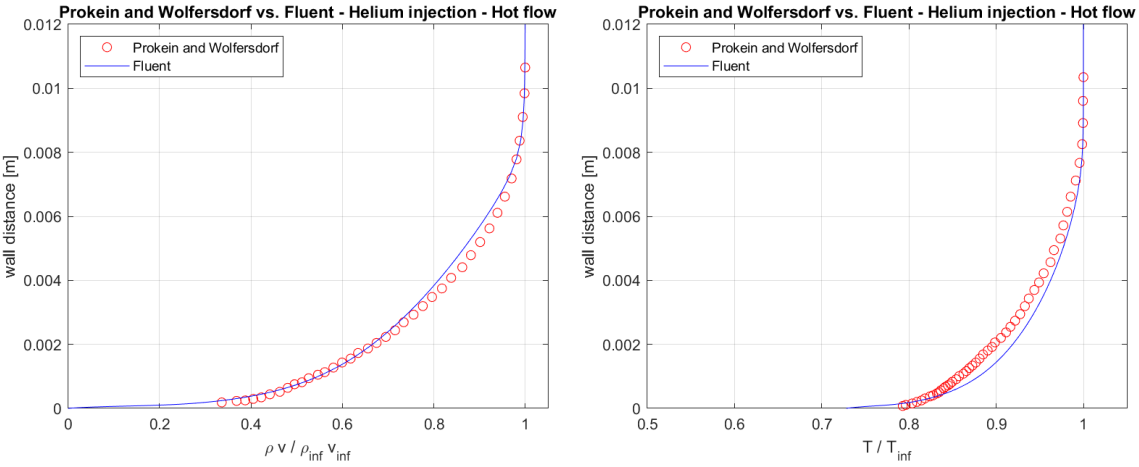

(a) Comparison between mass flux profiles for argon injection at F=0.0742%

(b) Comparison between temperature profiles for argon injection at F=0.0742%

Figure 29. Validation of mathematical models for non-isothermal blowing of helium in a heated main stream of air collected at $x = 0.442\,m$

The results, as the isothermal simulations, predict with acceptable accuracy the behaviour of the boundary layer in these conditions.

3.3 Wall shear stress and heat transfer analysis

As said before, in obtaining the classical hybrid regression rate theory we postulated the Reynolds analogy to transform a heat transfer in a momentum one, which is far easier to handle and estimate with empirical formulas.
In this section we will demonstrate the validity of the assumption for non-combusting flows (equivalent to the below-flame zone) by firstly showing that velocity and temperature profiles follow the same trend with varying F and then comparing $\frac{C_f}{C_{f0}}$ e $\frac{S_t}{S_{t0}}$ curves for the chosen gases.

Just cited graphs are the following (only argon injection has been shown for brevity):

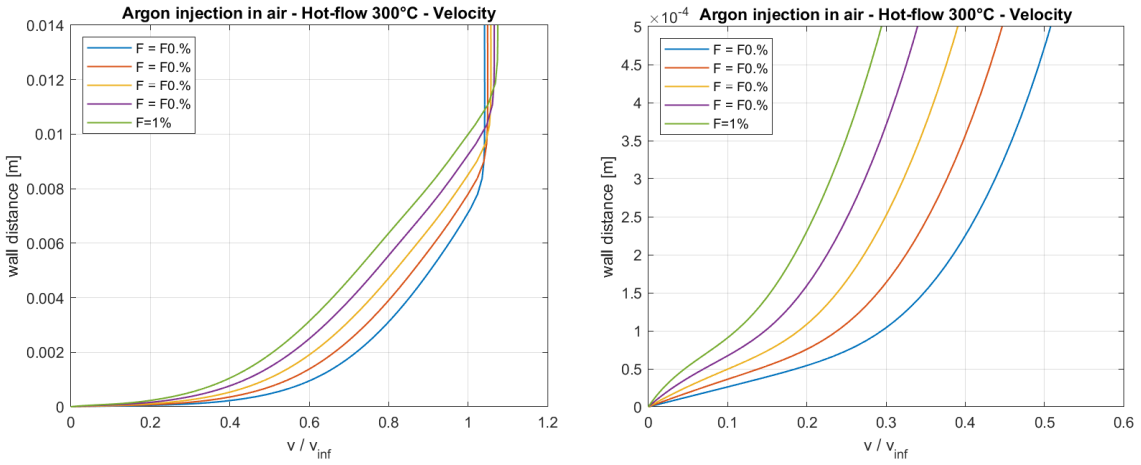

(a) Velocity profiles

(b) Detail of the left graph

Figure 30. Velocity profiles for argon injection in a heated main flow of air

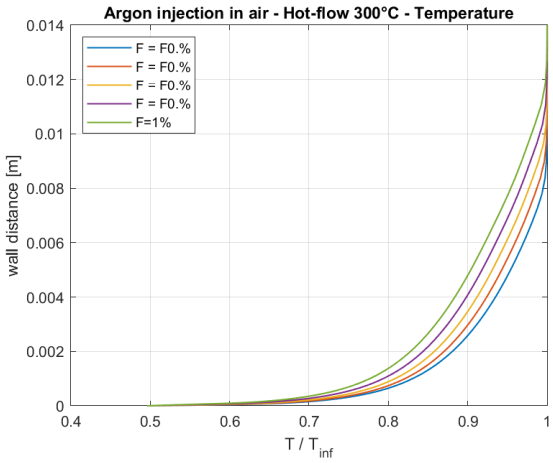

(a) Temperature profiles

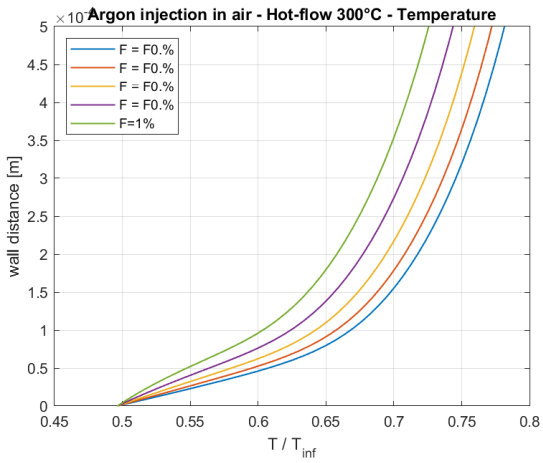

(b) Detail of the left graph

Figure 31. Temperatures profiles for argon injection in a heated main flow of air

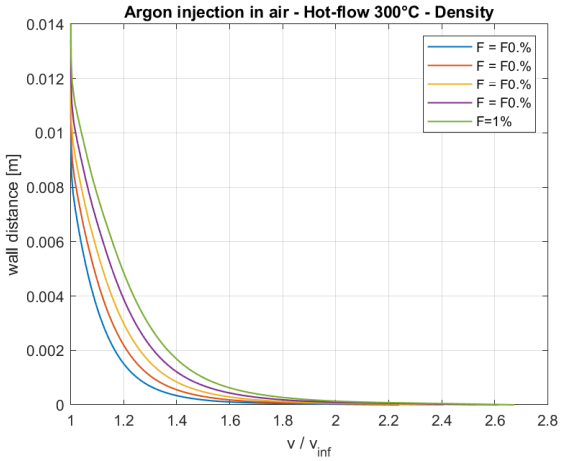

(a) Density profiles

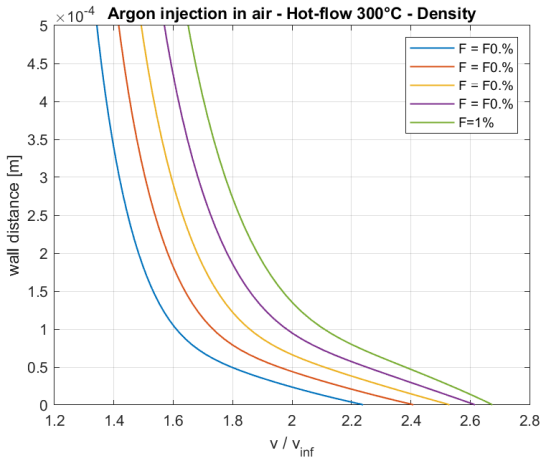

(b) Detail of the left graph

Figure 32. Density profiles for argon injection in a heated main flow of air

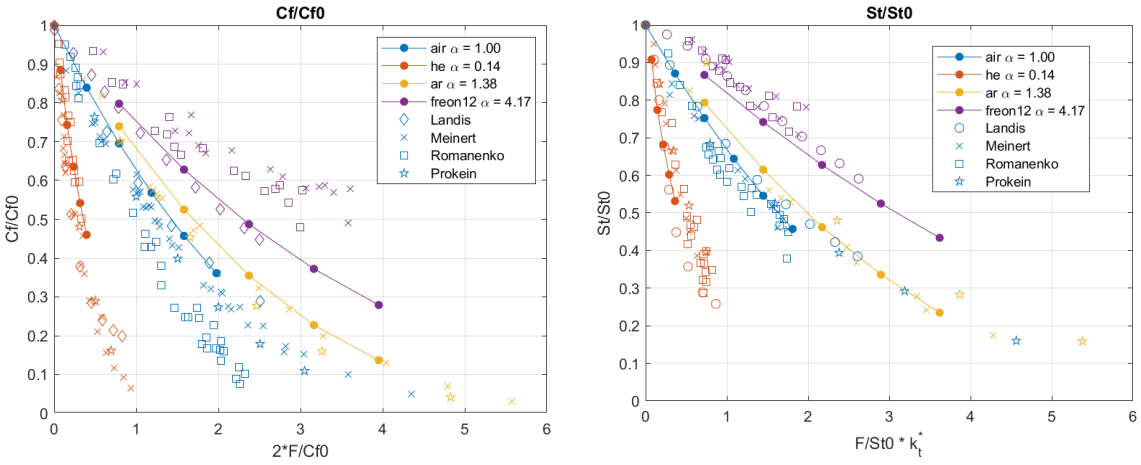

(a) $\frac{C_f}{C_{f0}}$ vs. $2\frac{F}{C_{f0}}$ (b) $\frac{S_t}{S_{t0}}$ vs. $\frac{F}{S_{t0}} \cdot k_t^*$

Figure 33. Ratios between friction coefficients and Stanton numbers for foreign gas injection into heated main stream of air. $\alpha = \frac{MM_{blowing}}{MM_{stream}}$

As we can see from the graphs above, the velocity and temperature profiles follow the same trend. The latter ones show also the near-wall flex already present in velocity profiles in isothermal simulations. The only real difference is that in the core flow it reaches 1 instead of a slightly higher value.
Regarding density profiles it seems that a heated flow increases the gradient but makes it more consistent with varying F (**Fig. 32** vs. **Fig. 21**).
The wall friction coefficient and Stanton Number ratios show a very good similarity without, however, being exactly equal. This discrepancy could be caused by the choice of zero thermal resistance at the wall which slightly alters the density profile or due to other effects such as the Prandtl Number Pr not being equal to 1. The important observation is, nonetheless, that the two graphs have the same trend, despite being produced by two separate phenomena (momentum transfer vs. heat transfer).
The Stanton number abscissa has been normalized using $k_t^* = (T_{stream}/T_{wall})^{0.3} \simeq 1.23$ as suggested by Meinert et al. [18].

As for isothermal simulations, other cases have been tested and they are shown here below:

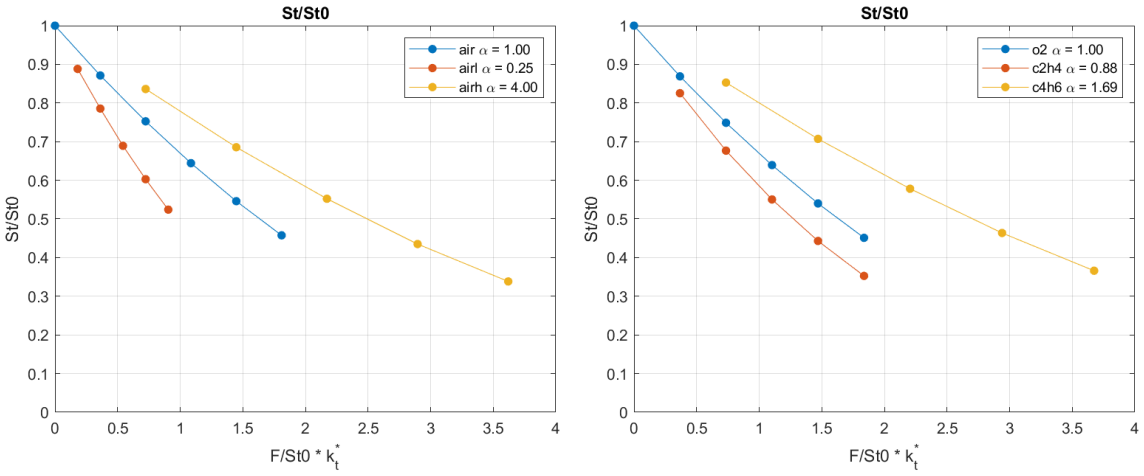

(a) $\frac{S_t}{S_{t0}}$ vs. $\frac{F}{S_{t0}} \cdot k_t^*$ in air heated main flow (b) $\frac{S_t}{S_{t0}}$ vs. $\frac{F}{S_{t0}} \cdot k_t^*$ in O_2 heated main flow

Figure 34. Ratios between Stanton numbers. $\alpha = \frac{MM_{blowing}}{MM_{stream}}$

An interesting observation that can be raised is that the curve relative to C_4H_6 injection in O_2 is higher than the curve associated to *airh* when the latter shows a density ratio higher than the former. This is probably due to difference in other molecular properties of the substances that are not, however, the focus of this work.

$\frac{C_f}{C_{f0}}$ authors' data in **Fig. 33a** are the same used in isothermal simulations, since $275\,°C$ of difference between main flow and transpirating wall seems to be too low to make an observable difference. Differences in temperature, however, could play an important role they are high enough or in case of combustion.
Paul et al. [22], for example, provide evidences for the strong correlation between main flow temperature and $\frac{C_f}{C_{f0}}$. In the next section we will explore this hypothesis keeping, the same setup as non-isothermal simulations.

3.4 Variable free stream temperature

In this section we will try to demonstrate the influence of the main stream temperature on the ratio of friction coefficients. Following the density hypothesis, the temperature difference could produce a higher or lower density ratio responsible for the increase or decrease of the $\frac{C_f}{C_{f0}}$.

To conduct this analysis some simulations have been set up with the same setup as before but with a variable free stream temperature, which in this case assumes

the following values: $300\,K$, $600\,K$, $1000\,K$ and $2000\,K$. Mass flux has been reduced to $20\,kg/m^2$, as always to avoid compressibility issues.

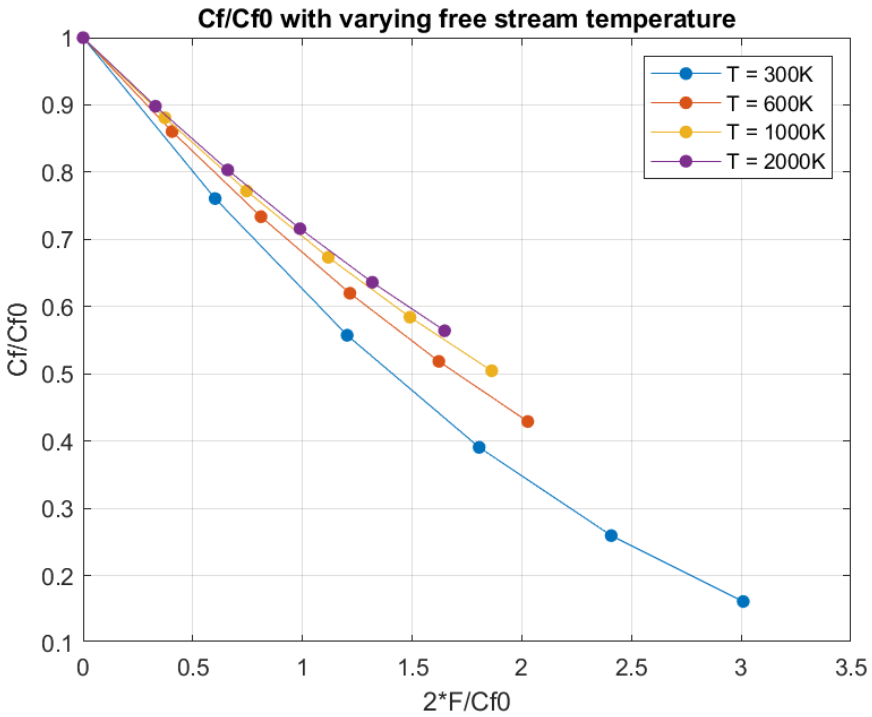

Figure 35. Friction coefficient as a function of blowing rate and main stream temperature, injection of air in air

As is clearly visible from **Fig. 35** the temperature variation has a non-negligible effect. In particular, as expected, an increase in free stream temperature raises the density ratio $\frac{\rho_{blowing}}{\rho_{stream}}$ and as a consequence the blown gas appears heavier and its blowing effect is reduced. Moreover, the variation of $\frac{C_f}{C_{f0}}$ seems to be small if compared to the one imposed by a foreign gas injection. The reason could be that a temperature increase speeds up the main gas stream, changing as a consequence C_{f0} which could have a small effect on the graph, or the heavy variation of molecular properties effect the phenomenon in ways we are not currently understanding.

4 Comparison with Paul et al.'s theory

In this chapter we will try validating or confuting Paul et al.'s theory, relying on the data obtained in previous sections.

During the derivation of equation 1.12, an estimate of the wall friction coefficient ratio is extracted [22]:

$$\frac{C_f}{C_{f0}} = \varphi^2$$

$$\varphi = \int_0^1 \sqrt{\frac{\rho}{\rho_e}\frac{1}{1+B\zeta}}\,d\zeta \tag{4.1}$$

Where, however, $\frac{\rho}{\rho_e}$ must be assumed. Paul et al. propose the following distribution postulating that, without combustion, the mass concentration of the injected species is a linear function of the velocity (equivalent to the below-flame zone). This is a consequence of the Reynolds analogy applied to momentum and species mass fraction transfer.

$$\frac{\rho}{\rho_e} = \left(\left(1 - \frac{1+B\,\rho_{ei}}{1+B}\right)\frac{u}{u_e} + \frac{1+B\,\rho_{ei}}{1+B}\right)^{-1}$$

With $\rho_{ei} = \frac{\rho_e}{\rho_{inj}}$. Comparing the formula just shown and the numerical density distribution obtained with a Fluent simulation we observe a non-negligible discrepancy (**Fig. 36**)

The reason for this could be the assumption of perfect proportionality between momentum and species mass fraction transfer. Although it is true that the concentration of the injected species follows the same trend of velocity (in reality the opposite is true, the velocity reaches a minimum at the wall while the concentration a maximum), the relation could be slightly superlinear or sublinear.

Moreover the effect is exacerbated by eventual temperature differences through the boundary layer.

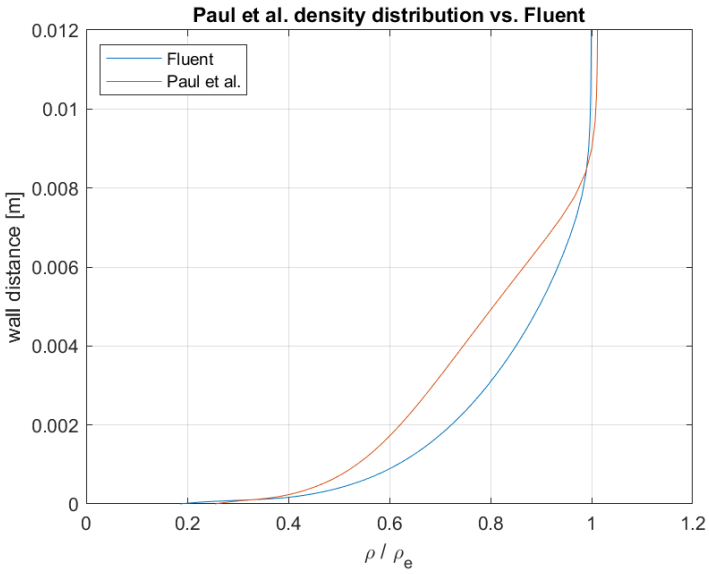

Figure 36. Comparison between the density profile from Fluent and the one assumed by Paul et al. in this work in the case of isothermal blowing of helium at $F = 0.0852\%$

Despite the density assumption is not quite accurate, the equation 4.1 shouldn't be discarded right away. Introducing the numerical density profile into it we obtain promising results showed in the figure below. The law, however, still do not capture the importance of the density difference, giving exceedingly high values for helium and low for argon and freon12.

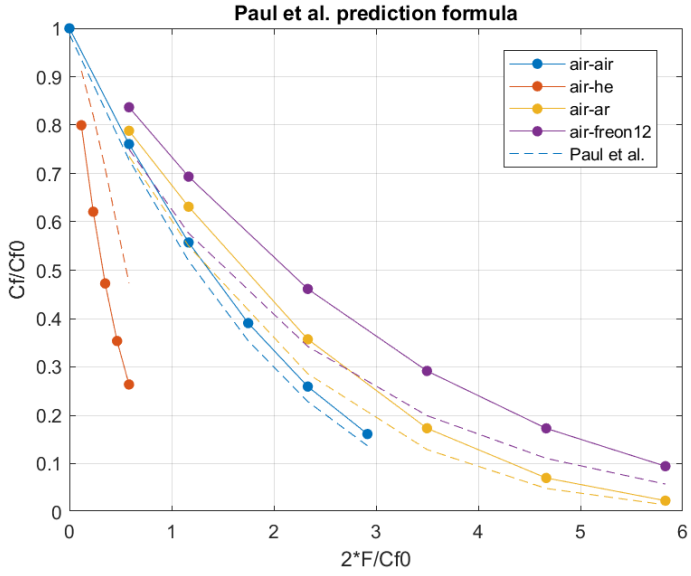

Figure 37. Comparison between real distribution of $\frac{C_f}{C_{f0}}$ with respect to the one obtained by introducing the real density profile into Paul et al.'s formula for cold-flow isothermal air injection

Regarding this, we propose a simple correction of expression 4.1 based on this work's data:

$$\varphi' = \int_0^1 \sqrt{\frac{\rho}{\rho_e} \frac{1}{1+\sqrt{\alpha}B\zeta}} d\zeta$$

$$\alpha = \frac{MM_{blowing}}{MM_{stream}}$$

$$\frac{C_f}{C_{f0}} = \varphi'^2$$

By adding a simple term at the denominator of the function in the integral we are able to make coincide very well the results. Errors are quite low for an analysis of this type, considering also the spread of the data in **Fig. 23**, especially for air and freon12.

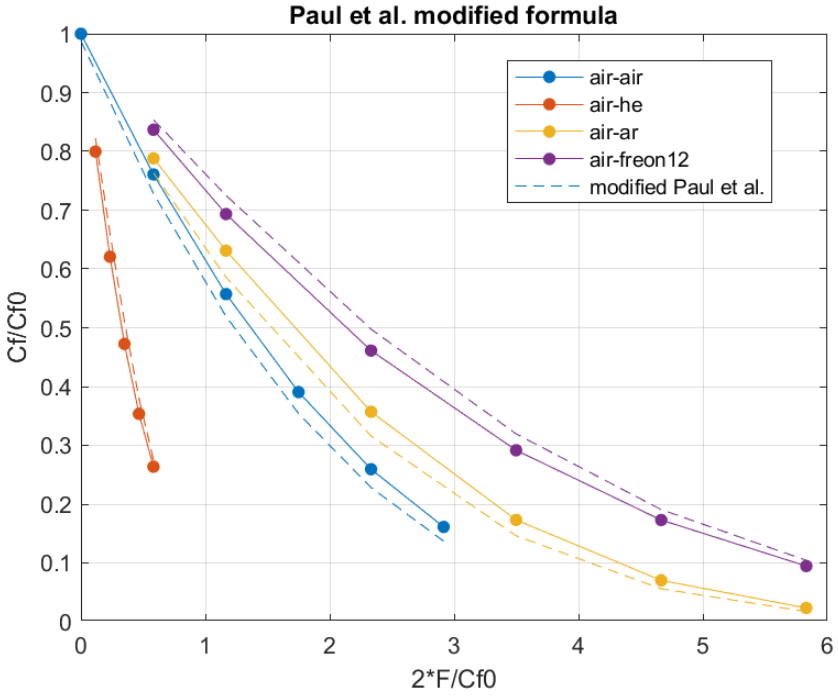

Figure 38. Graph $\frac{C_f}{C_{f0}}$ using the modified formula and numerical density distribution

If a good analytical estimate of the density profile is provided, at this point, one

could easily calculate the friction coefficient ratio. Unfortunately, this task if far from being easy. Here below a better formula than Paul et al.'s is proposed:

$$\frac{\rho - \rho_w}{\rho_e - \rho_w} = \frac{1}{(1-a)\frac{u_e}{u} + a} \tag{4.2}$$

With a being a function of F for which a good analytical expression has not been found. Its value, however, can be extracted by least-square fitting the data collected through the previous simulations (**Fig. 41**)

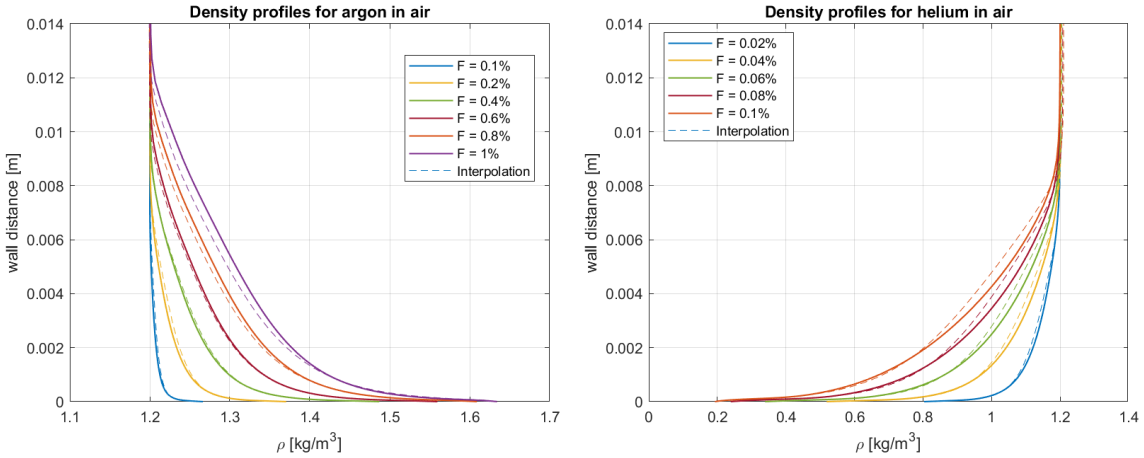

(a) (b)

Figure 39. Density profiles for argon (a) and helium (b) injection with interpolation using formula 4.2

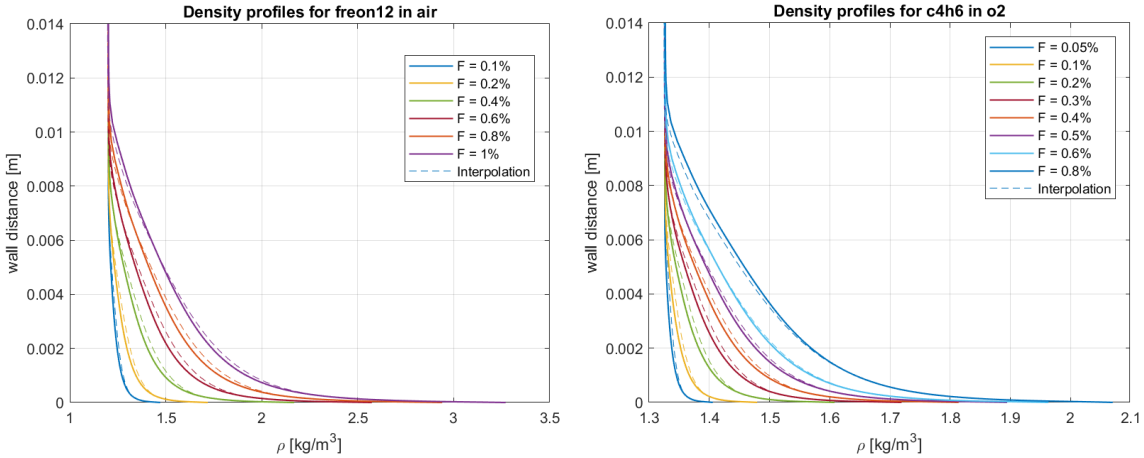

(a) (b)

Figure 40. Density profiles for freon12 (a) and c4h6 (b) injection with interpolation using formula 4.2

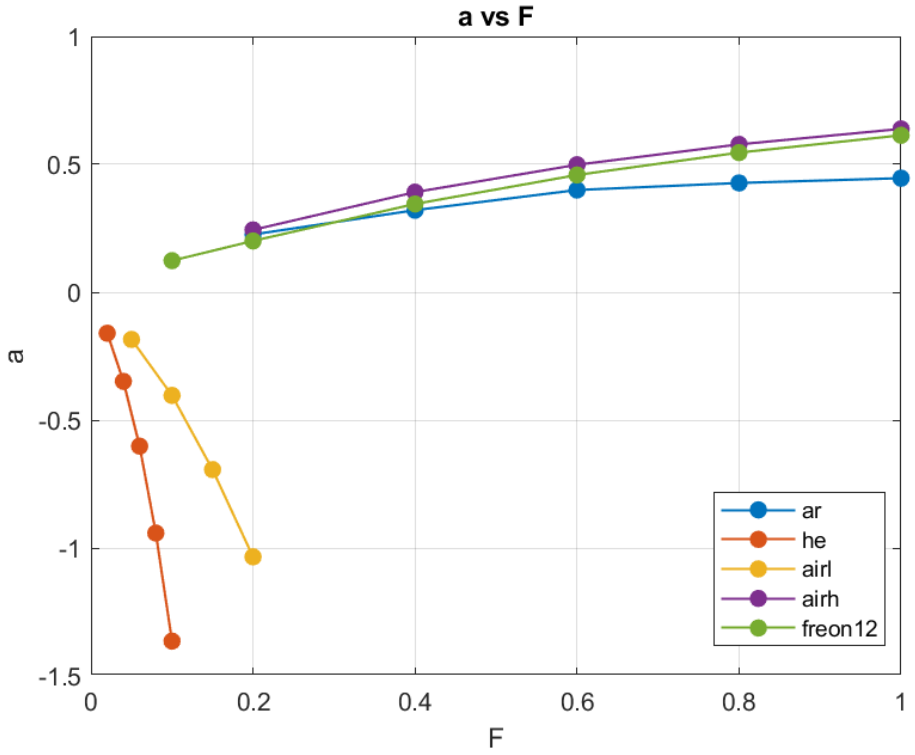

Figure 41. a parameter vs. blowing rate

As for a, an analytical expression has not been found for ρ_w too, so we just show its trend for some isothermal cases (**Fig. 42**).

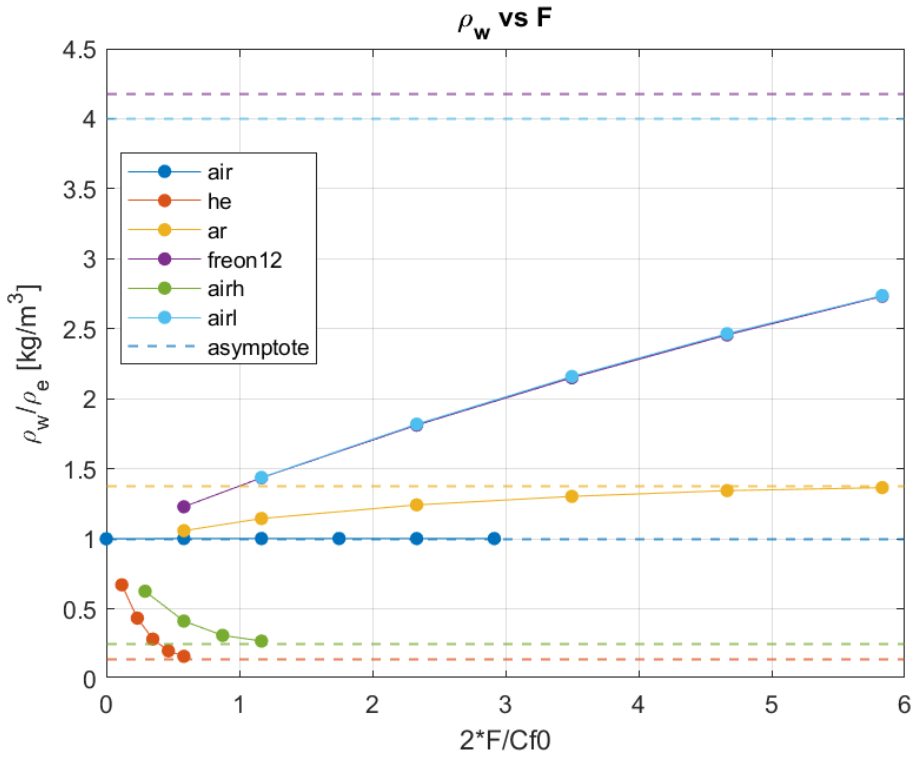

Figure 42. $\frac{\rho w}{\rho e}$ parameter vs. blowing rate

5 Combustion simulations

As a coronation of the work done in the previous chapters we propose also hybrid rockets simulations to assure that the discovered effect do not fail in presence of combustion or chemical reactions.
In the next sections we will describe the setup, the mathematical models and the results for this batch of simulations, from which we will draw our final conclusions.
The validation has been performed on the Carmicino et al. and Di Martino works ([3], [5], [7]), whose experiments at the Università Federico II di Napoli allowed them to have extremely good data on which compare our results.
Before proceeding to the implementation of physical model of the fuel grain a series of simulation with fixed mass flow rate have been conducted to assure the correct working of Fluent combustion.

5.1 Geometry and Mesh

Two main geometries were considered: The first relative to a hybrid 200 N rocket described in [7], while the second in [3] and [5] rated 1 kN (**Fig. 43**).
Thanks to the abundance of tests on the latter, many more simulations have been conducted on that one compared with the former. The reason for the choice of the first one is the extensive simulations conducted by Di Martino which are convenient for our validation.

The main difference between the two geometries is the dimension, while other details such as injector, prechamber and postchamber shape have been left unaltered by the authors.
Employed fuels are the already cited HTPB and HDPE, while the oxidizer is gaseous oxygen injected into the combustion chamber through a small conical injector.

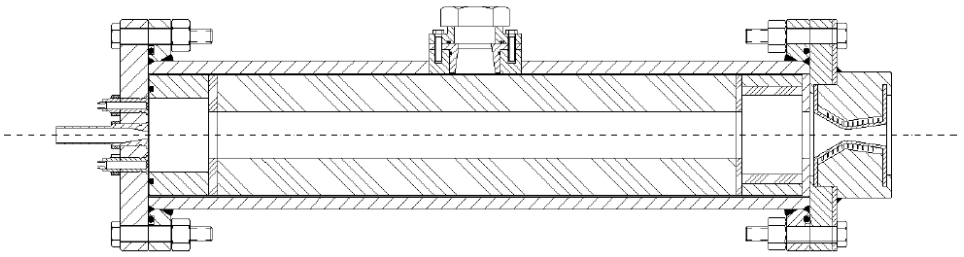

Figure 43. Cross section of the 1kN rocket used by Carmicino et al. in his experiments

General dimensions both rockets are tests data are listed here below:

	Test						
	200 N	5	7	10	1	2	12
Fuel	HDPE	HDPE	HDPE	HDPE	HTPB	HTPB	HTPB
L_{grain} [mm]	220	560	560	560	572	574	572
$\overline{D}_{port}$ [mm]	19.40	41.38	54.73	42.33	38.88	42.42	58.00
D_{pre-cc} [mm]	46.0	80.0	80.0	80.0	80.0	80.0	80.0
L_{pre-cc} [mm]	25.0	65.0	65.0	65.0	65.0	65.0	65.0
$D_{post-cc}$ [mm]	60.0	80.0	80.0	80.0	80.0	80.0	80.0
$L_{post-cc}$ [mm]	40.0	65.0	65.0	65.0	65.0	65.0	65.0
D_{inj} [mm]	6.0	8.0	8.0	8.0	8.0	8.0	8.0
$\overline{D}_{throat}$ [mm]	10.1	16.0	16.0	16.0	16.0	16.0	16.0
$\overline{p}_{cc}$ [bar]	6.49	15.67	19.21	20.51	4.51	16.16	24.56
t_b [s]	11.4	40.3	50.4	21.2	27.9	18.7	8.2
$\overline{O/F}$	5.63	2.76	2.83	3.02	0.97	1.942	2.06
$\overline{\dot{m}_{ox}}$ [kg/s]	0.027	0.124	0.157	0.177	0.032	0.133	0.197
$\overline{\dot{r}}$ [mm/s]	0.390	0.630	0.590	0.817	0.496	0.931	0.961
$\overline{c^*}$ [m/s]	1615	1892	1805	1748	1393	1615	1689
c^*_{th} [m/s]	1719	1853	1850	1830	1493	1807	1811
$\overline{\eta}_c$	0.952	1.021	0.976	0.955	0.934	0.894	0.933

Regarding the mesh ICEM CFD has been employed once again to create 2D computational grids (3D effects have been neglected to facilitate mesh generation, to ease the UDF implementation and to save computational resources). These grids trace the shape of the combustion chamber claimed by Carmicino et al. except for the port diameter, which to simulate the mean operating condition of the motor has been set to the average port diameter of the specific firing.
Prechamber and postchamber details of 1 kN meshes can be seen in **Fig. 44a** and **Fig. 44b**. All of them have been built making sure that y^+ near every wall was < 5, especially the one near the fuel grain. The height of the first cell in that region has been chosen $1\,\mu m$ and the total number of cells sums up to about 130'000, as before obtained after a mesh convergence analysis.

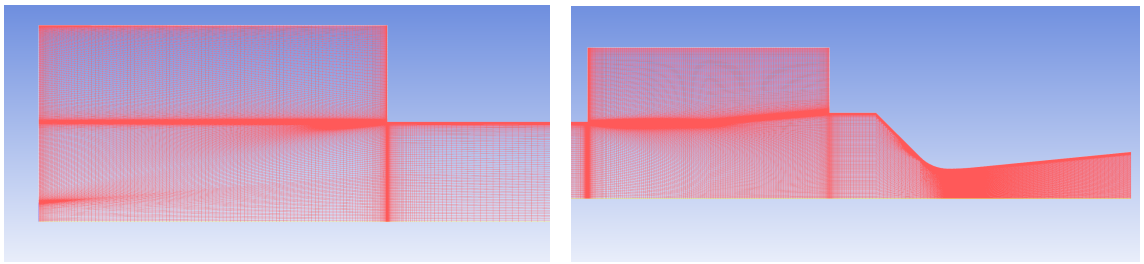

(a) Prechamber mesh detail (b) Postchamber mesh detail

Figure 44. Computational grid used in the 1 kN rocket simulations

Before proceeding at the next section, an important detail of the Carmicino et al.'s design must be noted, which is significant in determining the regression rates in their rockets: the conical injector (**Fig. 45**).
As already described in the first chapter, his team discovered that by injecting gaseous oxygen through a small conical aperture in a relatively large grain port, a strong turbulence is created and as a consequence hot gases are transported more easily near the wall. For this reason the following regression rate data for HTPB and HDPE are higher than classical rocket and shouldn't be taken as standard.

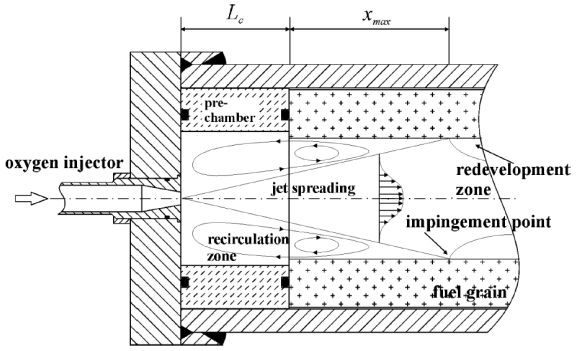

Figure 45. Detail of the conical injector used by Carmicino's team

5.2 Setup

Most of the mathematical models are similar to the previous chapter, with the exception of that this batch of simulations involves combustion and non-uniform blowing coupled with the wall heat flux. In the next sections we will describe in detail all the aspects pertinent to the work just described.

5.2.1 General setup and boundary condition

As said before, the used geometry is the same in all cases, with the exception of the port diameter, which is changed every time to match mean operative conditions. This procedure is not quite correct, however, for the regression rate claimed by Carmicino et al. is the space-temporal mean, which can be different from the spatial mean at the average port diameter (calculated using the initial and final value). Thanks to a fast and crude analysis that for brevity here will not be explained we estimated that this assumption can lead to an extra maximum 5% error, added to the pre-existing errors of the experimental setup

The employed boundary conditions are the following:

- **Injector** - Mass flow rate inlet:
  - Mass flow rate = average mass flow rate of oxygen of the test
  - Species: gaseous O_2 mass fraction = 1
  - Total temperature = $300\,K$
  - Turbulence intensity = 5%
  - Turbulence viscosity ratio = 10

- **Outlet** - Pressure outlet:
  - Pressure = 1 bar with "avereage-pressure specification"

- **Grain wall (fixed flow rate)** - Mass flow inlet:
  - Mass flow rate = average mass flow rate of fuel of the test
  - Species: gaseous C_2H_4 or C_4H_6 mass fraction = 1
  - Total temperature = $950\,K$
  - $\omega_{SST} = \frac{6\nu_w}{0.075\Delta y^2}$
  - $k = 0$

- **Grain wall (UDF)** - Wall + source:
  - Injection of C_2H_4 for HDPE or C_4H_6 for HTPB with an UDF (see "Grain pyrolysis model")

- **Wall** - Fixed wall:
  - Adhesion condition $u_w = 0$
  - Impermeability condition $v_w = 0$
  - Adiabatic $\frac{dT}{dy} = 0$

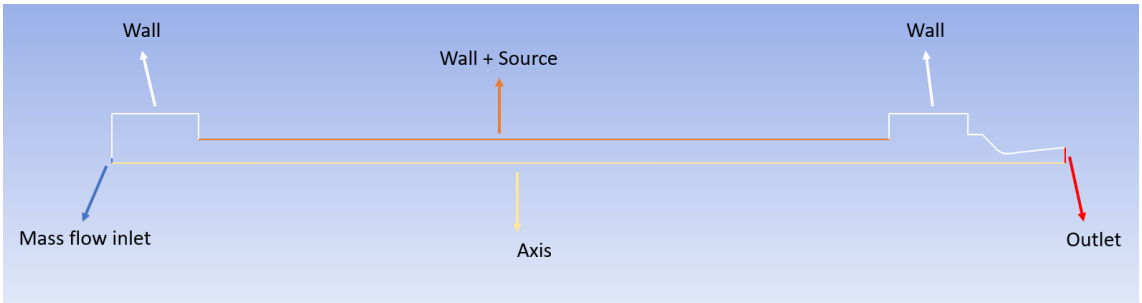

Figure 46. Boundary conditions for the combustion simulations

5.2.2 Combustion model

Despite being possible to implement chemical reactions (manually) even in the "Species Transport" model (SP), it has been preferred the use of the "Non-Premixed Combustion" model (NP), which is automatic and gives far more accurate results. The NP model does the following assumptions:

- Reactions are infinitely fast (in our case this is satisfied since $Da >> 1$)

- All chemical species have the same mass diffusion rate

- Lewis Number $Le = 1$, i.e. mass diffusivity = thermal diffusivity

Last two statements are valid in case of fully turbulent flows (as in fact the one in a rocket motor) and allow the introduction of a new variable called "Mean Mixture Fraction" f_{mix}, which represents the relative abundance of fuel over the oxidizer (1 = only fuel, 0 = only oxidizer). Substituting every species mass fraction field with the f_{mix}, beyond saving a lot of computational resources, paves the path for the use of a more complex chemical solver.
Since every f_{mix} value is linked to a defined reactants amount, the final state is determined. The model couples the Mean Mixture Fraction field with a look-up table (called PDF) calculated using a CEA solver before starting the simulation.

The generation of a PDF requires, however, some parameters:

- Operative pressure: Chosen as the experimental combustion chamber pressure of the specific test. It does not need to be precise but at least near the expected pressure (chemical equilibrium depends lightly on the pressure, so small differences are not critical)
- Fuel Rich Flammability Limit (FRFL): Imposed at 200% of stoichiometric f_{mix}. This value has been chosen as such in that minimizes the errors of the simulations. It dictates the maximum fuel concentration (given as a f_{mix} value) over which chemical equilibrium calculations are interrupted (most of the time it saves computational time and capture better the physics of the problem). The chosen values are FRFL = 0.452 for C_2H_4 and FRFL = 0.47 for C_4H_6
- Initial fuel temperature, set to $950\,K$ (classic wall temperature for polymeric fuels).
- Initial oxidizer temperature = $300\,K$
- Non-adiabatic (activation of heat transfer to the grain wall)

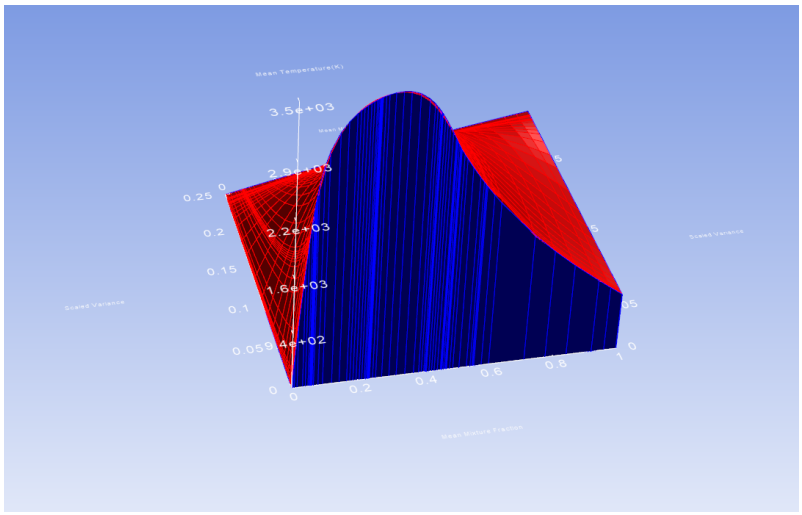

Figure 47. Example of a PDF for the Non-Premixed Combustion model

5.2.3 Grain pyrolysis model

The main jump in complexity when going from a cold to a hybrid rocket simulation is the solid-fluid interface and the associated grain pyrolysis law.
In particular, an UDF has been applied at the grain wall to simulate the fuel decomposition and injection that solves the system of equation below, whose unknowns are regression rate $\dot{r}$ and wall temperature T_s:

$$\dot{r} = \frac{Q_{tot}}{h_v \rho_{fuel}} \tag{5.1}$$

$$\dot{r} = A e^{-\frac{E_a}{2RT_s}} \tag{5.2}$$

The first is the 1.2, while the second is an Arrhenius law, derived from mathematical steps that for brevity here are omitted but that are available in [14].
Equation 5.2 links the combustion speed to the wall temperature, allowing us to find the latter. A and E_a are two parameters called pre-exponential factor and activation energy respectively, both obtainable through measure or from the physical properties of the material and the characteristics of the chemical reaction in play.
For HTPB and HDPE these are the values used in the simulations ([1], [14]):

	A [m/s]	E_a [J/mol]
HDPE	4780	251040
HTPB	0.01104	41086.88

A is not a constant as it may seems but varies slightly with the temperature (with a $\sqrt{T}$ dependence). However for simplicity and because this correction is very small (**Fig. 48**) we decided to employ anyway the equation 5.2.

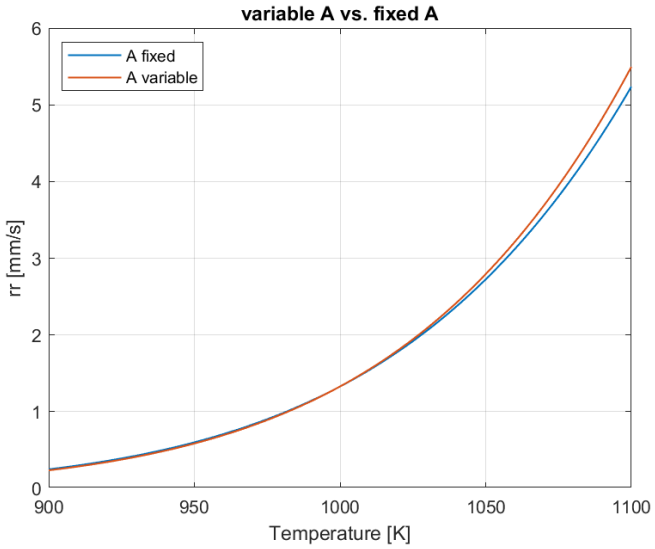

Figure 48. Comparison between regression rate predicted assuming A fixed vs A variable with $\sqrt{T}$

Regarding the fuels density ρ_{fuel}, the value claimed by Carmicino et al. has been chosen ([3], [5]), which is equal to $960\,kg/m^3$ for HDPE and $930\,kg/m^3$ for HTPB.
The effective vaporization enthalpy h_v was obtained from the equation 1.3 assuming for HDPE the C_p as follows:

$$C_p(T) = \begin{cases} -1040 + 9T & \text{if} \quad T <= 407\,K \quad \text{(solid)} \\ 370 + 5.1T & \text{if} \quad 407\,K < T < 650\,K \quad \text{(liquid)} \\ -255.32 + 8.29T - 1.00 \cdot 10^{-2} T^2 + 8.25 \cdot 10^{-6} T^3 - 2.89 \cdot 10^{-9} T^4 & \\ \qquad\qquad \text{if} \quad T > 650K \quad \text{(gaseous } C_2H_4\text{)} & \end{cases}$$

With the transition to gaseous decomposition products fixed at $650\,K$. Products which are assumed to be composed by only ethylene C_2H_4. Liquefaction, vaporization and pyrolysis latent heats have been taken respectively as $225\,kJ/kg$, $485\,kJ/kg$ and $3335\,kJ/kg$ [7] obtaining the h_v showed in **Fig. 49a**

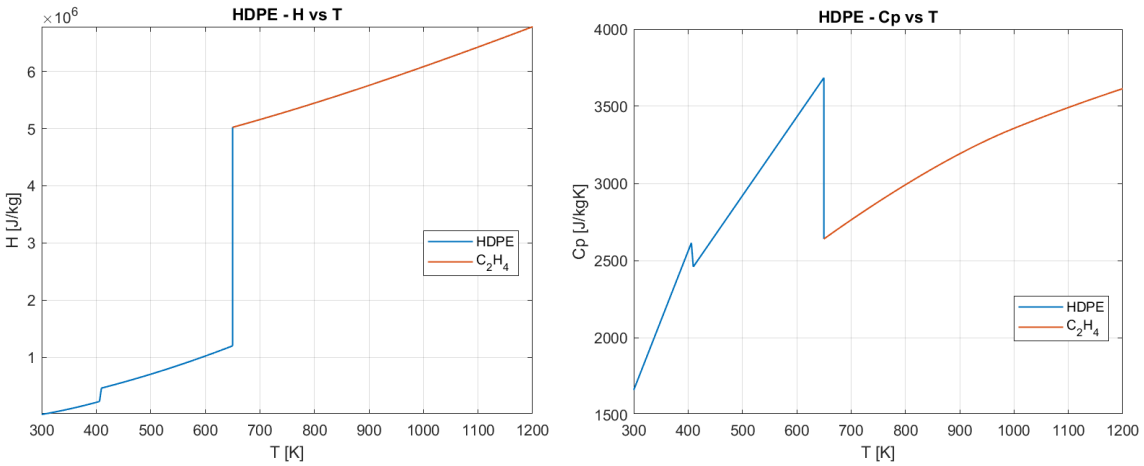

(a) h_v vs T (b) C_p vs T

Figure 49. Modeling of h_v and C_p of HDPE as a function of temperature

These values are compatible with experimental measurements in [26], which for temperatures between $700\,K$ and $850\,K$ claims effective vaporization enthalpies around $4000 \div 5500\,kJ/kg$, dependent on the type of polyethylene.

Since the temperature of the wall will be surely above $650\,K$, a polynomial interpolation of h_v has been found in the range $650\,K < T < 1200\,K$:

$$h_v = 4 \cdot 10^6 + 2.926 \cdot 10^2 T + 2.305 T^2 - 5.151 \cdot 10^{-4} T^3 \qquad (5.3)$$

For HTPB, unfortunately, no reliable and complete data have been found regarding its effective vaporization enthalpy or that allowed its calculation. Since, however, HTPB and HDPE are similar fuels which display many comparable thermodynamic properties ([16], [14]), the same h_v of the latter has been chosen.
This has two consequences: it probably produces errors in simulations of HTPB based rockets, adding up to the already present ones, but removes a variable in play in the determination of the regression rate, which makes our analysis more significant and focused towards the density effect.

Regarding the thermal conductivity and viscosity of C_2H_4 and C_4H_6, they have been chosen constants calculated at $950\,K$, since they are relevant only under the boundary layer where the temperature is similar to the one of the wall. The exact values are the following:

	μ [Pa · s]	λ [W/mK]
C_2H_4	3.02E-05	0.13491
C_4H_6	2.44E-05	0.1456

Summing up, the UDF implements the following pseudocode:

Main Fluent loop

```
for Faces f in Fuel_Surface
    Ts = T(f);
    dTdy = T_GRADIENT_Y(f);
    lambda_eff = K_EFF(f);
    Q_tot = -lambda_eff * dTdy;
    Tnew = Ts;
    do
        Told = Tnew;
        hv = [Eqn 5.3];
        rr = Q_tot / (rho_fuel * hv);          [Eqn. 5.1]
        Tnew = Ea/(2 * R * log(A/rr));         [Eqn. 5.2]
        error = abs(Tnew - Told);
    while error < tolerance
```

```
        Ts = Ts + URF * (Tnew - Ts);
        rr = A * exp(Ea/(2 * R * Ts));                    [Eqn. 5.2]
        T(f) = Ts;
        m_fuel(f) = rho_fuel * rr;
    end for
end loop
```

5.3 Results

5.3.1 Fixed mass flow rate

Here below the results regarding fixed mass flow rate simulations are shown. As said before, the imposed value of mass flow rate is the temporal average of the specific test claimed by Carmicino et al..

	Test						
	200 N	5	7	10	1	2	12
Fuel	HDPE	HDPE	HDPE	HDPE	HTPB	HTPB	HTPB
$\overline{p}_{sperim}$ [bar]	6.49	15.67	19.21	20.51	4.51	16.16	24.56
p_{sim} [bar]	6.56	15.32	18.30	21.46	4.34	15.50	23.21
p_{sim} relative error [%]	0.98	-2.23	-4.75	4.63	-3.65	-4.10	-5.52
c^*_{sim} [m/s]	1652	1820	1736	1829	1393	1615	1689
η_{sim}	0.961	0.982	0.938	0.999	0.900	0.857	0.882

Globally we can see a good agreement with experimental data. The current modelization of the problem is then able to predict correctly the combustion chamber pressure and as a consequence c^* and the combustion efficiency η_c.

For the 200 N test images of the flowfield are available from the PhD thesis of Di Martino [7] on which compare further the data.

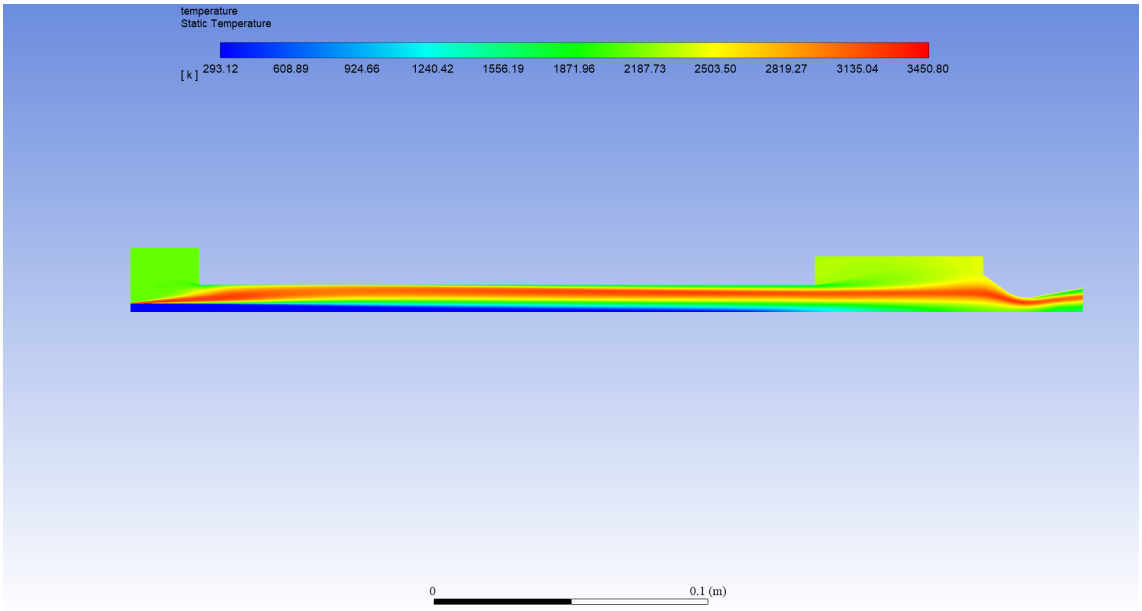

Figure 50. Temperature - 200 N test - Fluent simulation

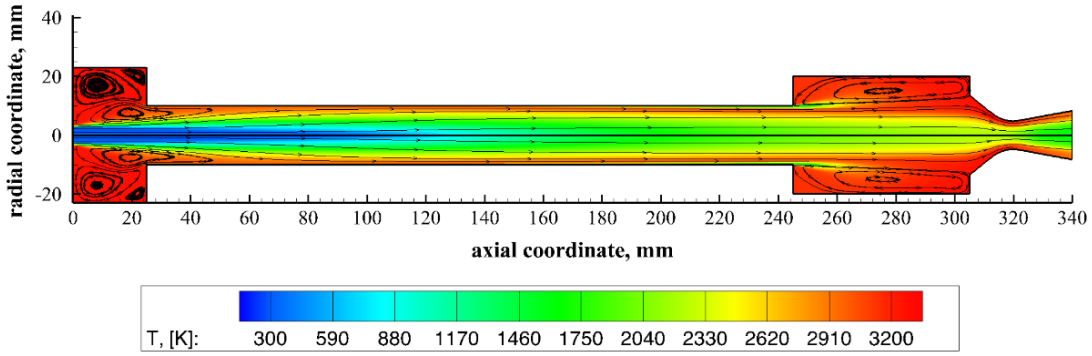

Figure 51. Temperature - 200 N tes t - from [7]

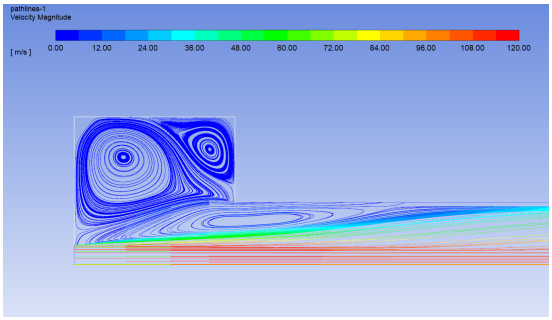

(a) Velocity colored streamlines from Fluent simulation

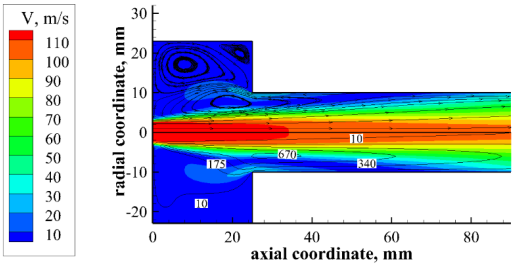

(b) Streamlines and velocity field from [7]

Figure 52. Pre-chamber streamlines and velocity for 200 N test

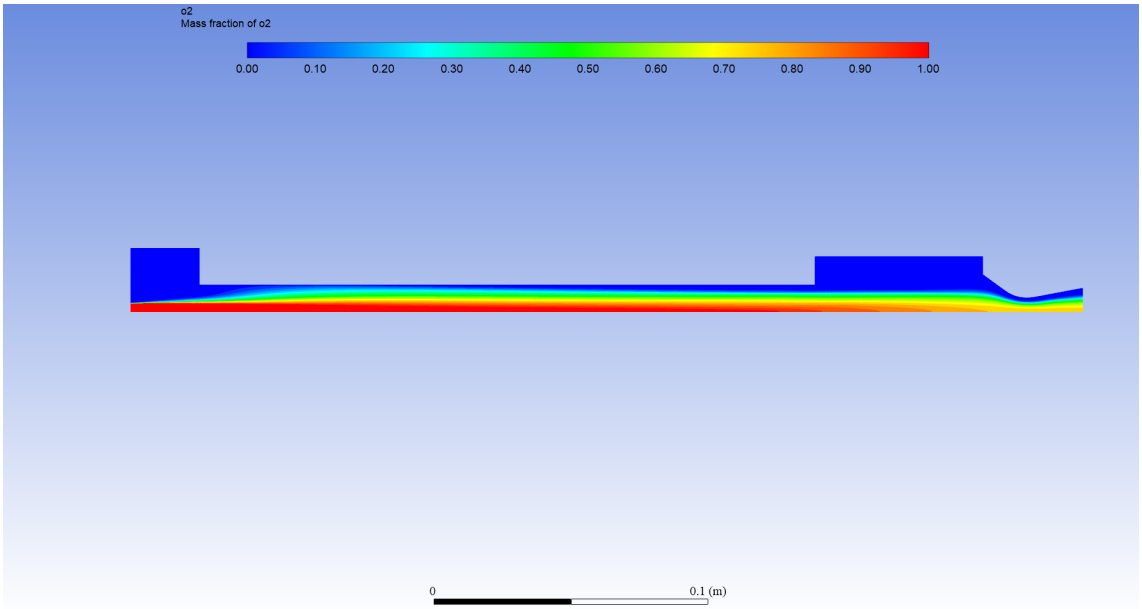

Figure 53. O_2 mass fraction of - 200 N test - Fluent simulation

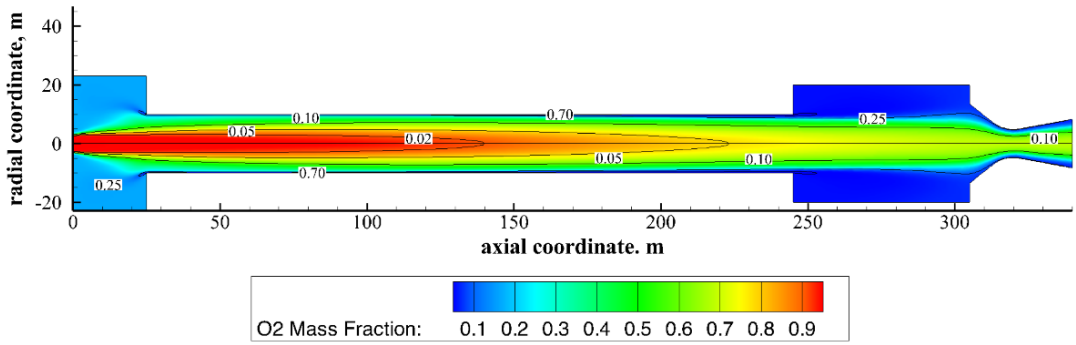

Figure 54. O_2 mass fraction of - 200 N test - from [7]

As evident from the above figures the fluid field is more or less accurate, with the major differences located in pre-chamber and post-chamber, which are far colder than the one from [7]. This however is not a significant problem, since it is negligible on the main flow and it is probably due by the adiabatic wall boundary condition, which does not allow the reach of a thermal equilibrium.
Another notable difference is in the main oxidizer jet, as it seems more long and coherent than in the comparison data, probably accentuated by slightly different colormaps.

In figures **Fig. 52a** and **Fig. 52b** pre-chamber eddies are visible. Even in this aspects, the two simulations seems to give coherent results despite $k-\omega SST$ being famous for losing accuracy in free-shear flows such the one immediately after the conical injector (flows in which big shear stresses are created not by a wall but by steep fluid velocity gradients).

5.3.2 Autoconsistent mass flow rate

Having tested the combustion model in the previous section, we proceeded implementing the grain pyrolysis UDF and attaching it to the correct domain boundary. Running the same cases as before with the new modelization, we managed to obtain the following results:

	Test						
	200 N	5	7	10	1	2	12
Fuel	HDPE	HDPE	HDPE	HDPE	HTPB	HTPB	HTPB
$\overline{p}_{sperim}$ [bar]	6.49	15.67	19.21	20.51	4.51	16.16	24.56
p_{sim} [bar]	6.09	14.90	20.06	21.98	4.35	16.65	25.52
p_{sim} relative error [%]	-6.29	-4.94	4.38	7.15	-3.43	3.04	3.89
$\overline{\dot{r}}_{sperim}$ [mm/s]	0.390	0.630	0.590	0.817	0.496	0.931	0.961
$\overline{\dot{r}}_{sim}$ [mm/s]	0.362	0.560	0.599	0.751	0.414	0.784	0.905
$\dot{r}_{sim}$ relative error [%]	-7.19	-11.03	1.47	-8.13	-16.46	-15.84	-5.78
$\overline{T}_{s,sim}$ [K]	919.6	966.2	969.3	984.2	752.3	931.8	984.4

Like before, the errors on pressure are generally contained in $\pm 5\%$, while for regression rate they are a bit larger $\pm 15\%$. For HTPB-based rockets, the latter seems to be on average lower than for HDPE-based rockets. This can be the consequence of assuming its h_ν equal to the one of the other fuel, or, instead, the fact that the radiative transfer has not been accounted, when for HTPB it can sum up to a significant portion of the total one, since its soot production is higher. Results, however are excellent considering the complexity involved.

The mean grain surface temperature is, as expected, around 950 K (the one assumed in fixed mass flow rate simulations), with the only exception being the test 1, which however is characterized by a oddly low regression rate and oxidizer mass flux.

In the next pages other results are shown (test 7 has been taken as sample).
The fluid field seems plausible, with high temperatures in most of the domain that produce the high experimentally measured characteristic velocities and combustion efficiencies.
In the pre-chamber we can see also a strange phenomenon: the development of the flame before the oxidizer jet comes in contact with the fuel grain, as visible in the 200 N simulations too. This is not the case for all hybrids, but it is probably an effect caused by the use of the Carmicino et al.'s conical injector and the creation of the cited recirculation eddies that transports gasified fuel against the main flow, helping greatly the mixing.

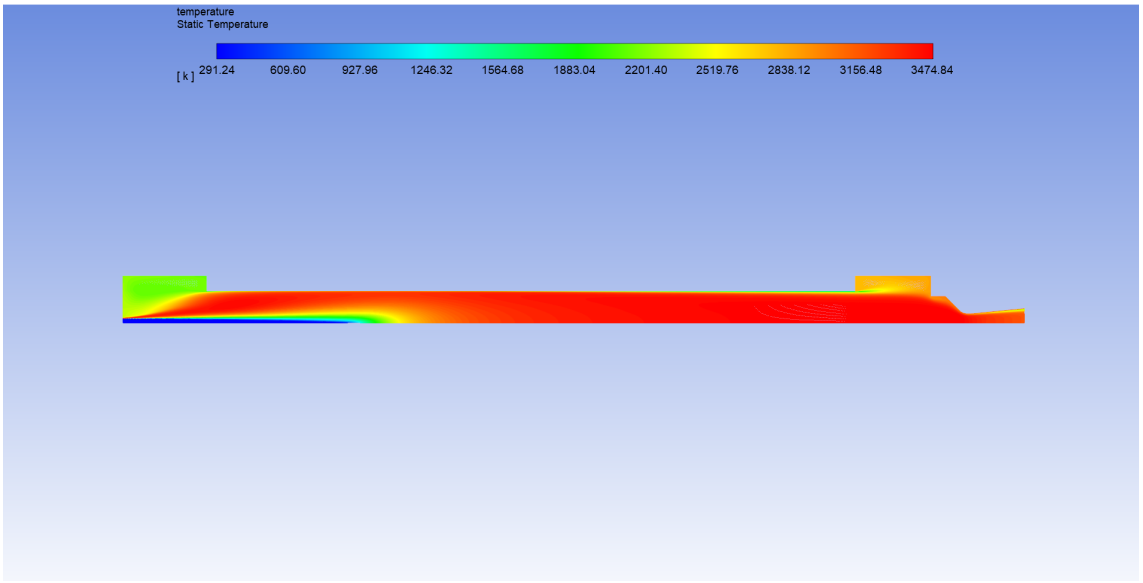

Figure 55. Temperature - test 7

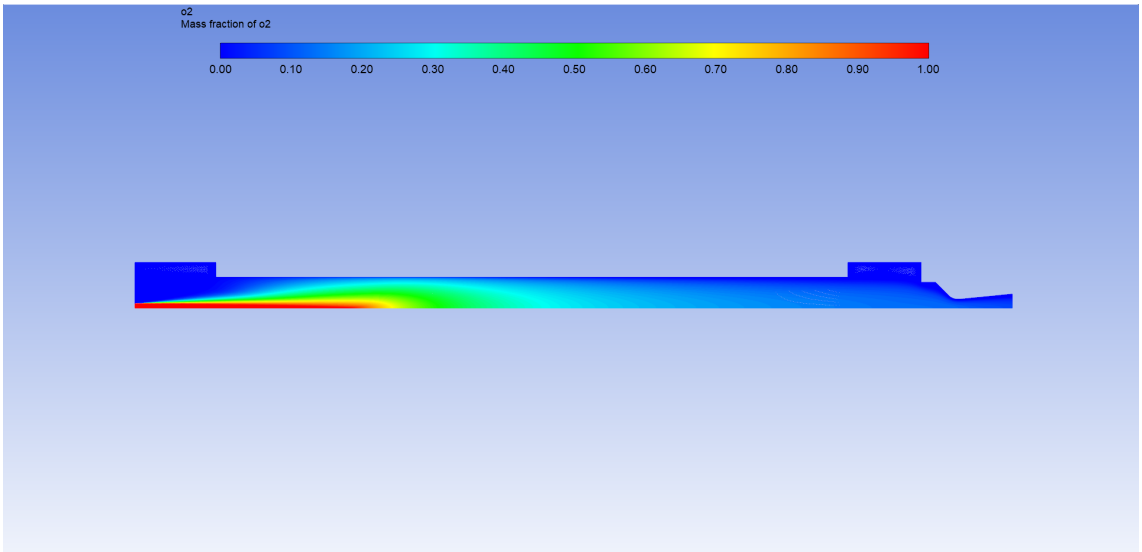

Figure 56. O_2 mass fraction - test 7

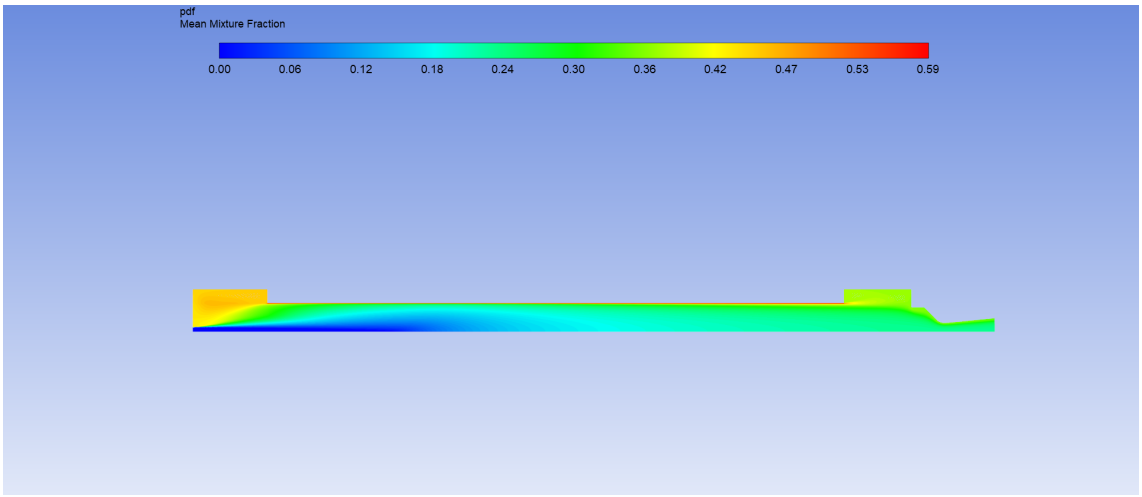

Figure 57. f_{mix} - test 7

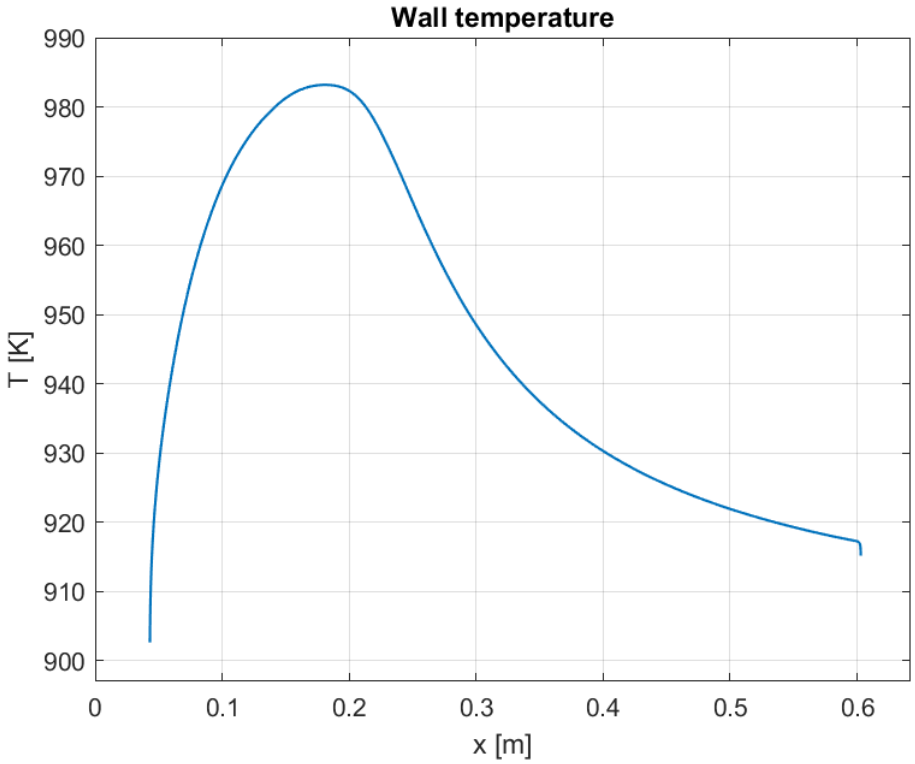

Figure 58. Grain surface temperature as a function of longitudinal coordinate - test 7

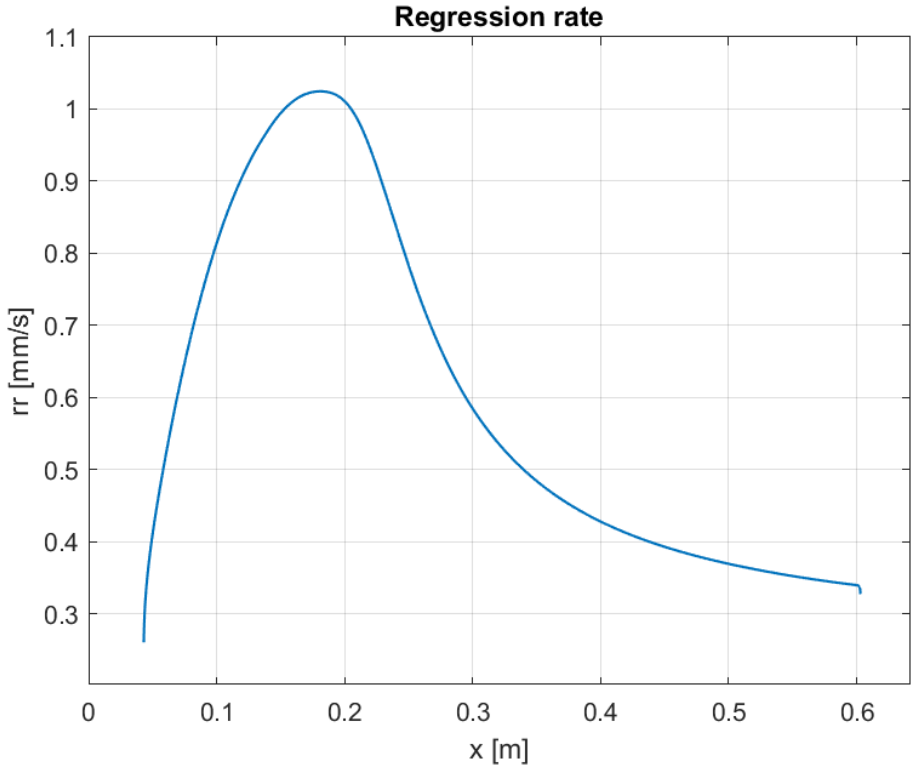

Figure 59. Predicted Fluent regression rate as a function of longitudinal coordinate - test 7

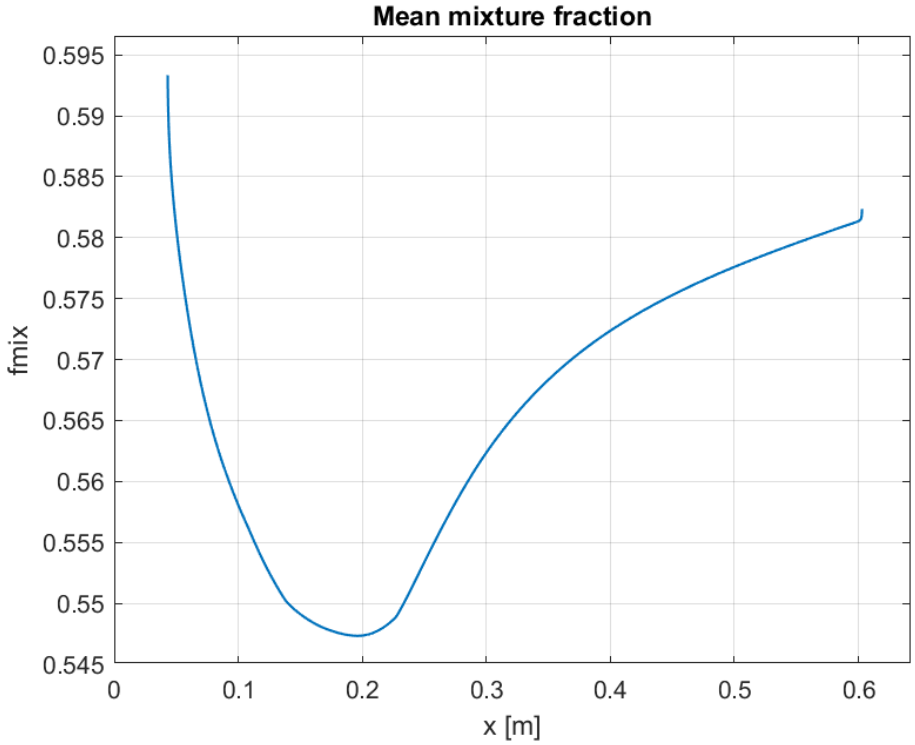

Figure 60. Wall mean mixture fraction as a function of longitudinal coordinate - test 7

Various variables are shown too, sampled vertically along the rocket length for test 7 (HDPE) and 12 (HTPB) at x = $300\,mm$, $400\,mm$, $500\,mm$ and $600\,mm$.

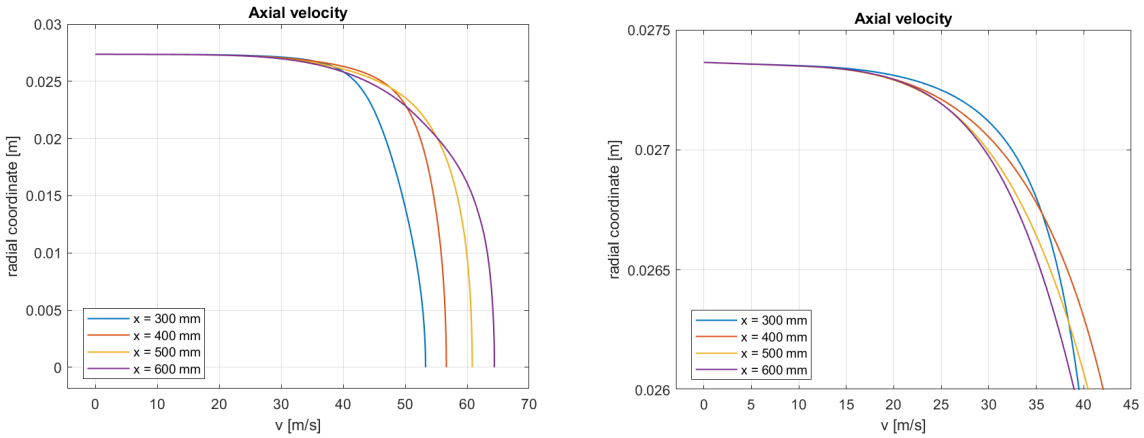

(a) Axial velocity vs. radial coordinate

(b) Detail of the left graph

Figure 61. Velocity profiles - test 7

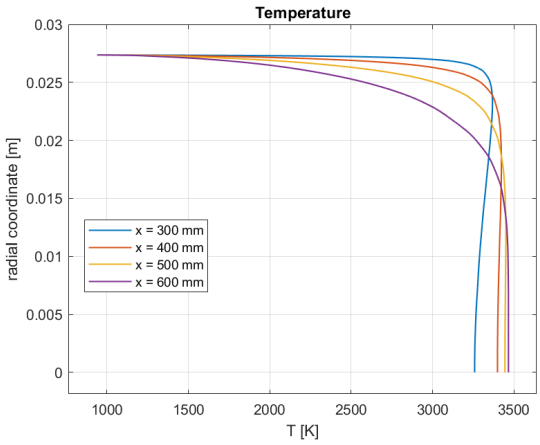

(a) Temperature vs. radial coordinate

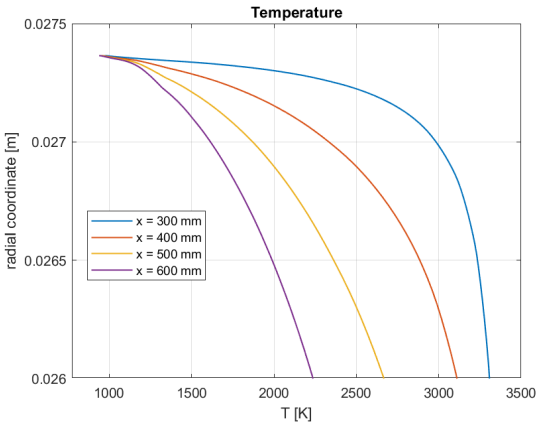

(b) Detail of the left graph

Figure 62. Temperature profiles - test 7

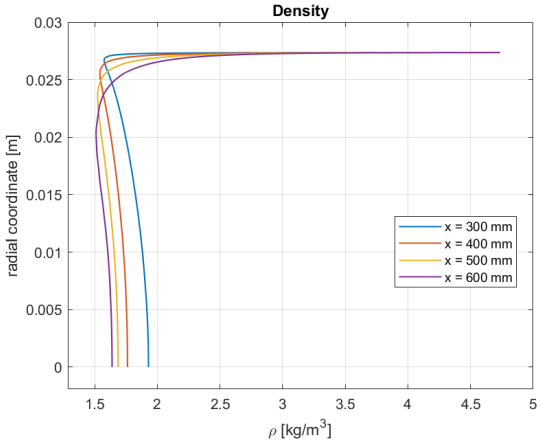

(a) Density vs. radial coordinate

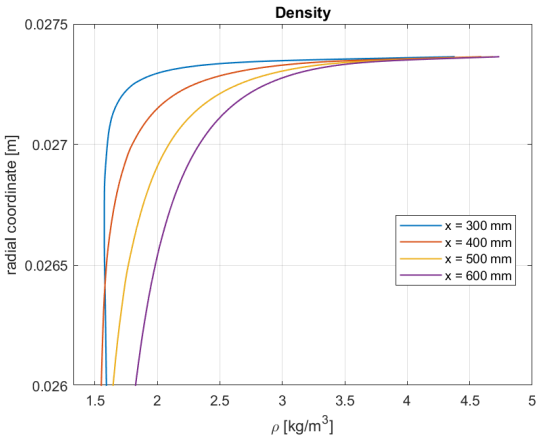

(b) Detail of the left graph

Figure 63. Density profiles - test 7

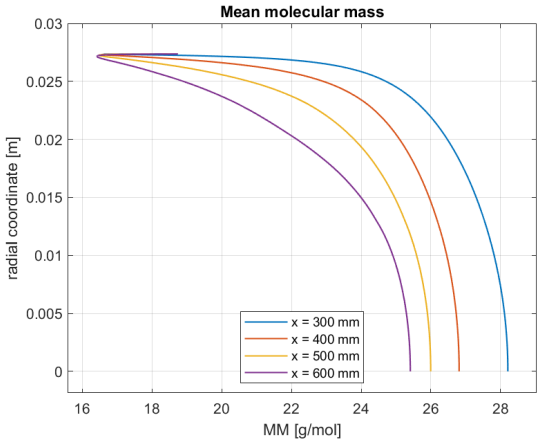

(a) Mean molecular mass vs. radial coordinate

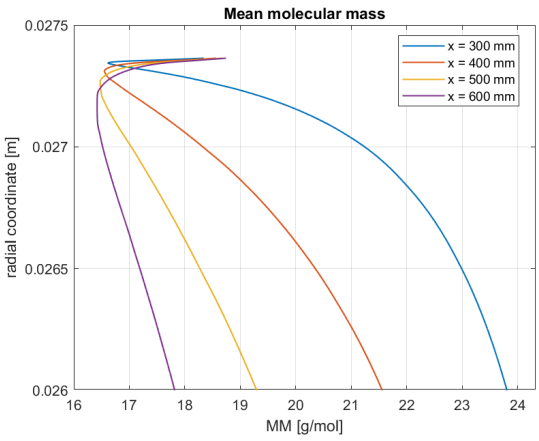

(b) Detail of the left graph

Figure 64. Mean molecular mass profiles - test 7

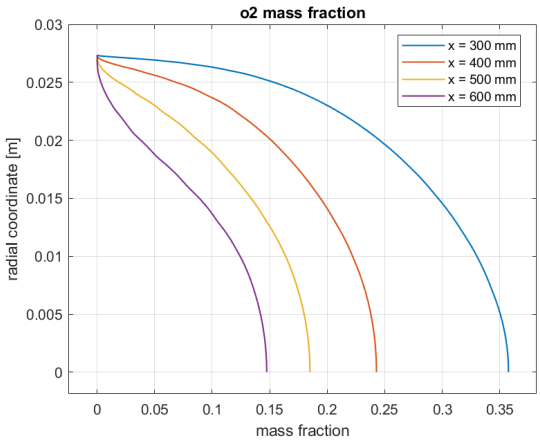

(a) O_2 mass fraction vs. radial coordinate

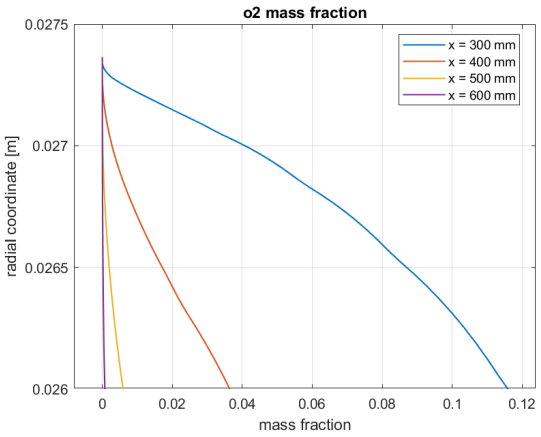

(b) Detail of the left graph

Figure 65. O_2 mass fraction profiles - test 7

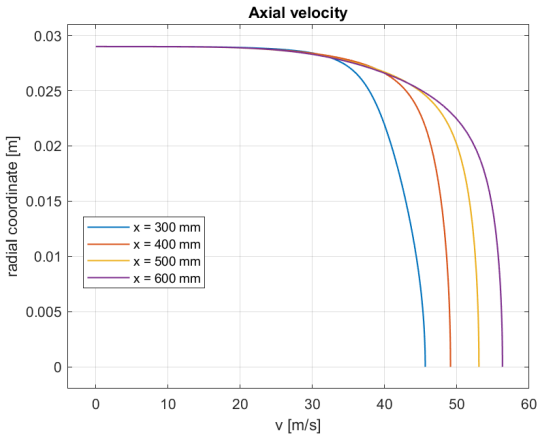

(a) Axial velocity vs. radial coordinate

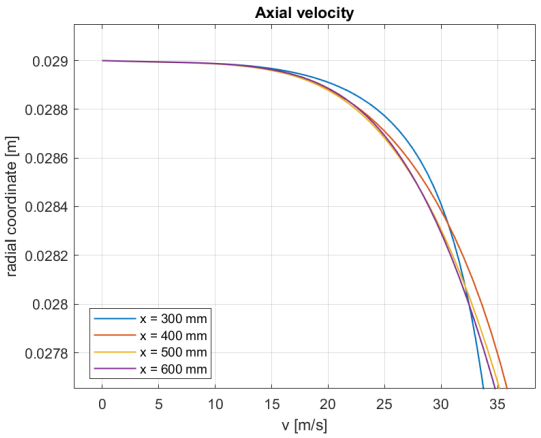

(b) Detail of the left graph

Figure 66. Velocity profiles - test 12

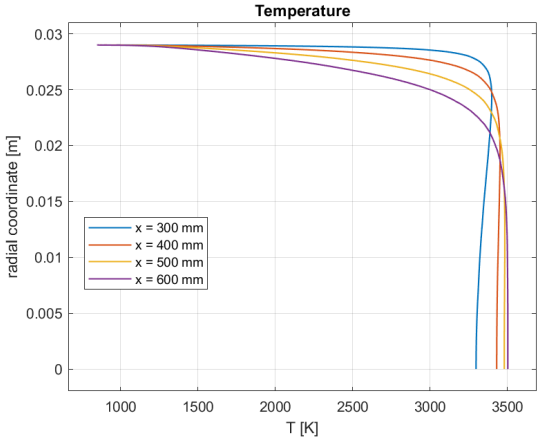

(a) Temperature vs. radial coordinate

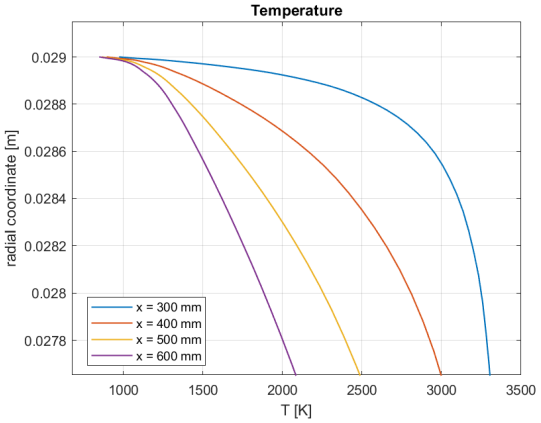

(b) Detail of the left graph

Figure 67. Temperature profiles - test 12

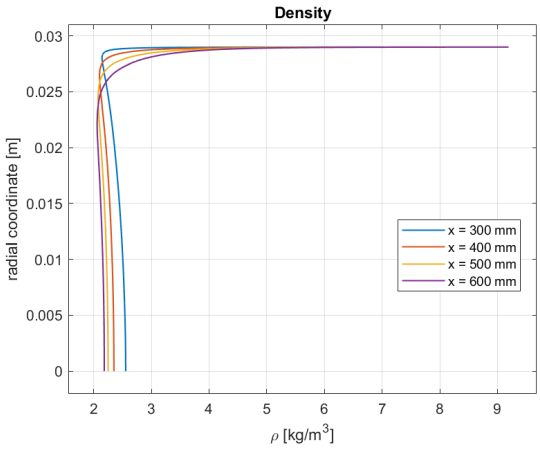

(a) Density vs. radial coordinate

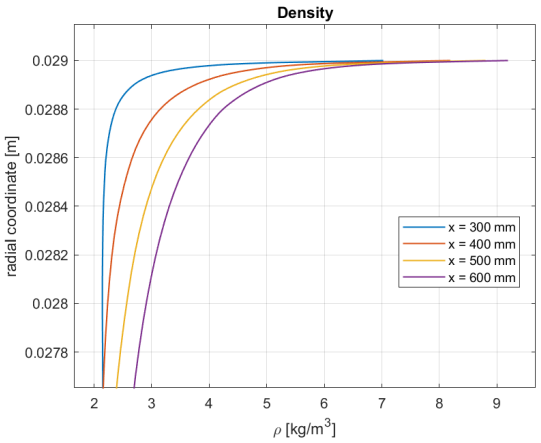

(b) Detail of the left graph

Figure 68. Density profiles - test 12

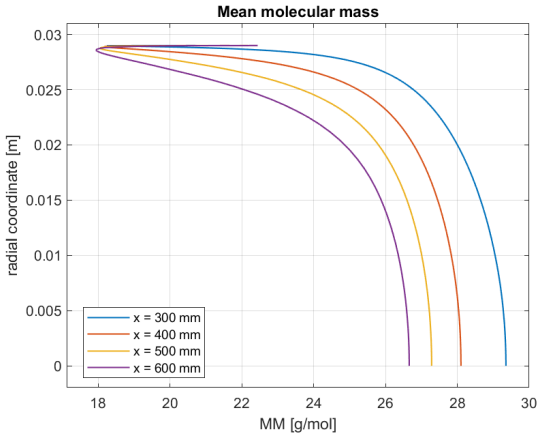

(a) Mean molecular mass vs. radial coordinate

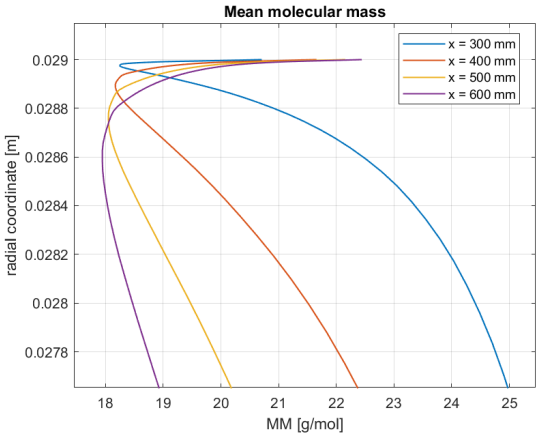

(b) Detail of the left graph

Figure 69. Mean molecular mass profiles - test 12

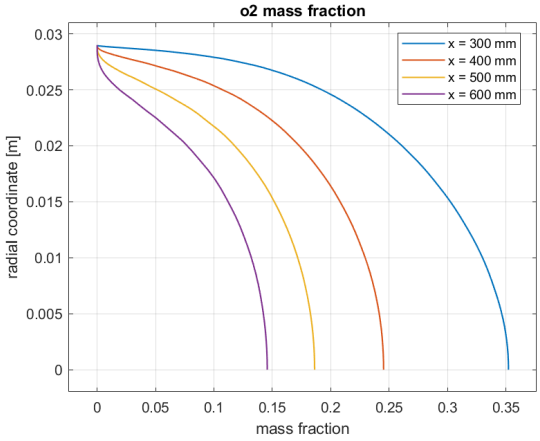

(a) O_2 mass fraction vs. radial coordinate - test 12

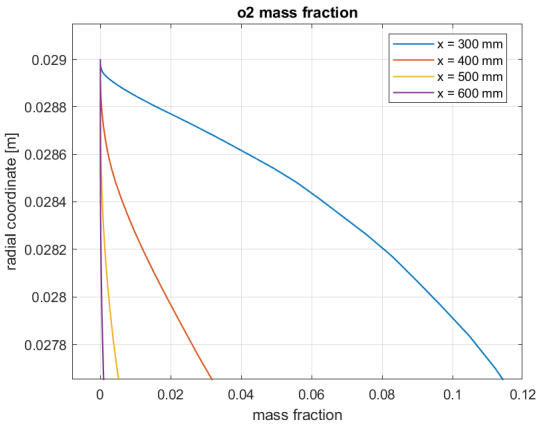

(b) Detail of the left graph

Figure 70. O_2 mass fraction profiles - test 12

In the above graphs we see a quite plausible development of the boundary layer and flame (identified as the peak in temperature profile). Some researchers ([1], [27]) observed different distributions as shown in **Fig. 71**, with peaks in density and velocity profiles or strong pressure gradients (especially in Wooldridge e Muzzy [27], probably due to an associated density gradient).
These have not been found in the present work, suggesting that the phenomenon is specific of some fuel combinations or, more likely, that it depends on the internal geometry of the combustion chamber. The simulations set up in the previous chapter involved a conical injector and gaseous oxygen, which produced a large amount of turbulence and mixing, leading to a more uniform field instead of a strong stratification as for example in **Fig. 72**.

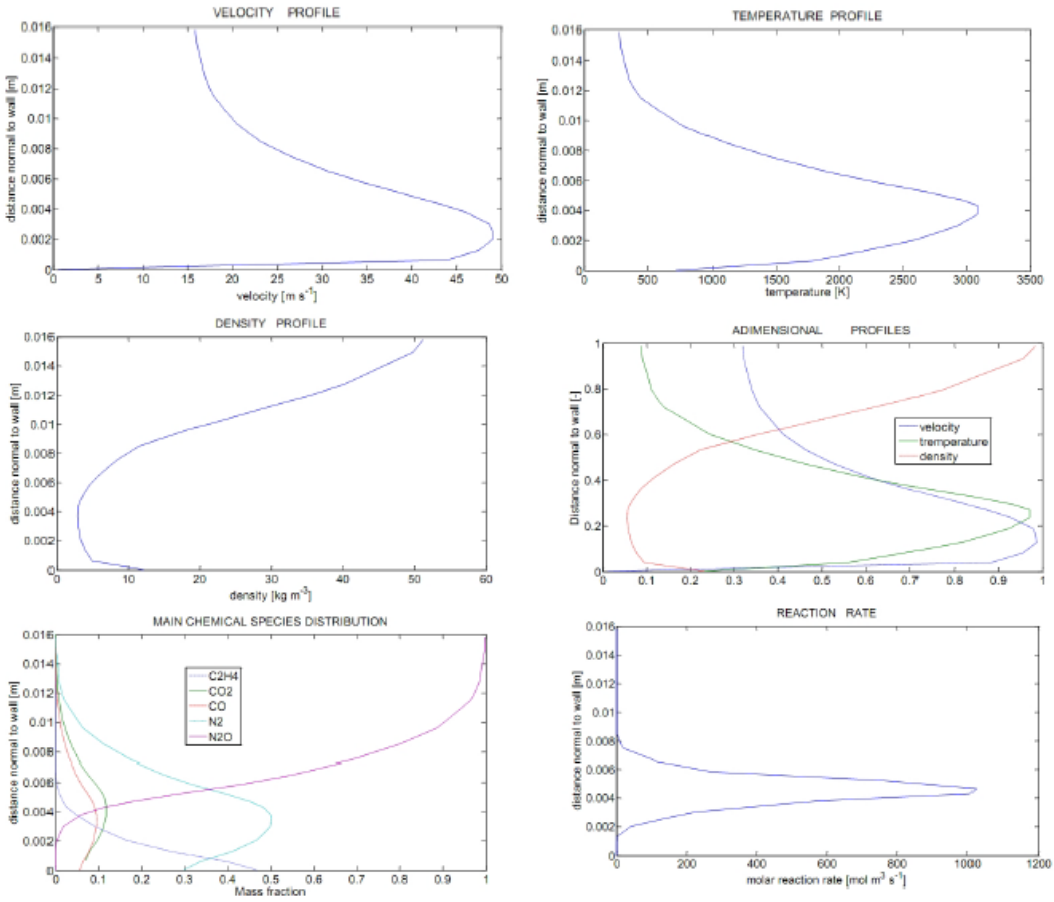

Figure 71. Wall profiles of some variables from Bellomo [2]

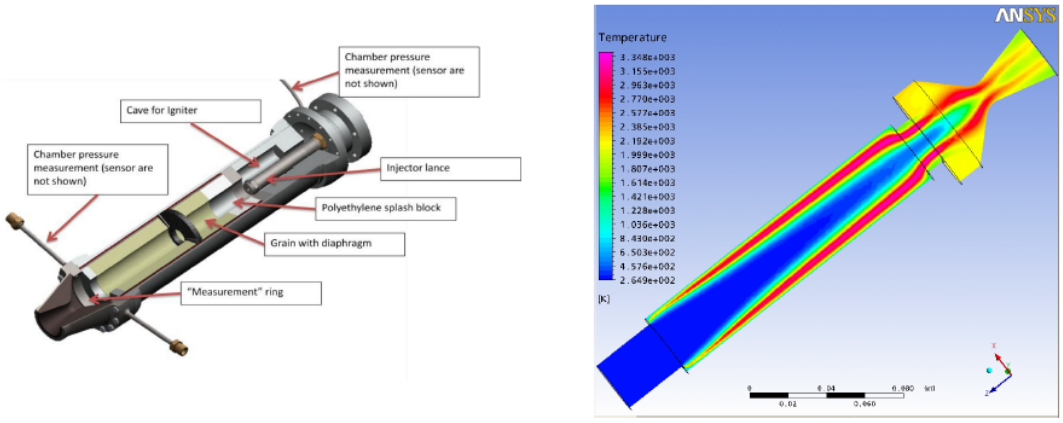

Figure 72. Motor geometry from [12] and CFD simulation from Bellomo [2]

5.4 Variable injection temperature

Other analyses have been conducted to confirm the results obtained in previously regarding the effects of a variable temperature main flow.
These simulations have been set up using the test 7 mesh and boundary conditions (including the fuel pyrolysis UDF), which showed the smallest error between all the cases, the only difference being the temperature of the main oxidizer jet, set to $300\,K$, $600\,K$, $1000\,K$ and $1500\,K$.

The results are here below.

Injection temperature [K]	$\dot{r}$ [mm/s]	$\dot{r}$ increase
300	0.598	0%
600	0.736	23.0%
1000	0.834	39.4%
1500	0.913	52.5%

As expected the regression rate undergo a significant increase, compatible with what found in the non-isothermal simulations section. This effect seen in the numerical analysis is not accounted in Marxman's theory. Δh_{w-b} should not change much since at high temperatures the gas dissociates, flattening the difference in injection temperature (**Fig. 74**). The possible explanation could be, as we are trying to demonstrate, the density difference between injected gas and main stream induced by a variation in oxidizer injection temperature.

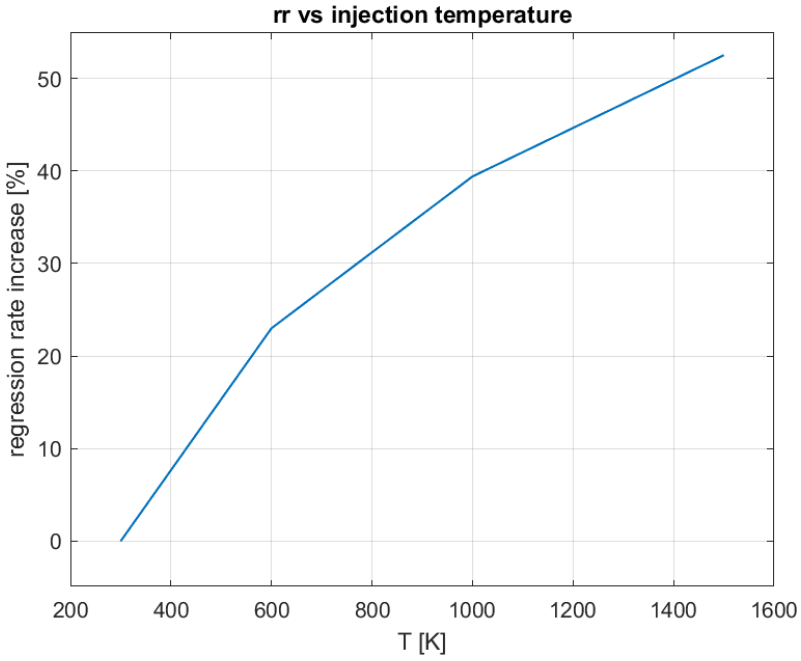

Figure 73. Regression rate increase vs. temperature - test 7

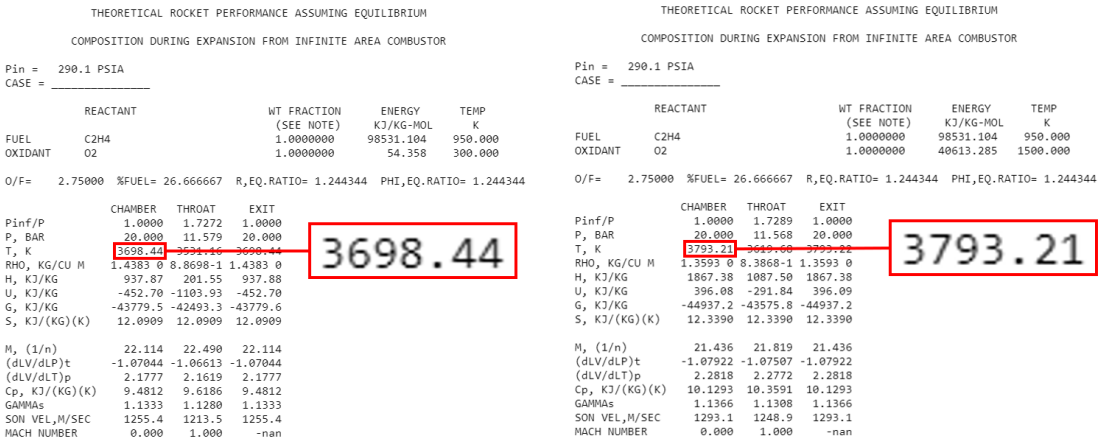

Figure 74. Temperature given by a Chemical Equilibrium Analysis (CEA) for cold (left, $300\,K$) and hot (right, $1500\,K$) oxygen injection into the combustion chamber

5.5 Estimation of regression rate ratio from data

The regression rate ratio between HDPE and HTPB could theoretically be derived from the $\frac{St}{St_0}$ data obtained in non-isothermal simulations chapter regarding blowing of O_2, C_2H_4 and C_4H_6 in a heated main stream of O_2 (if possible effects of combustion and other phenomena present in a rocket are neglected).

The only edit we need to make is on the temperature correction, which has been taken equal to $k_t^* = \left(\frac{3000}{950}\right)^{0.3} = 1.41$ as suggested in [18] (the exponent

is between 0.2 and 0.4). Although Meinert et al. advise against the use of such expression for the correction when the temperature ratio is above 1.5 (since it's out of range in their experimental setup), we try anyway to use it, since better formulations have not been found, taking the results with a grain of salt.

To find the theoretical regression rate ratio we proceed as following:

- Take a reference point from an existing test on a rocket. In this case the test 7 has been chosen as a sample.

- Estimate the St_0 with the following formula

$$Re_D = L * \frac{G}{\mu_{c2h4}}$$

$$Pr \simeq 0.7$$

$$St_0 = 0.037 * Re_D^{-0.2} * Pr^{0.67}$$

  The wrong determination of the St_0, in reality, does not pose a concerning problem, since the ratio is unaffected or weakly affected by it.

- Calculate $\frac{F}{St_0} k_t^*$

- Find the ordinate of the C_2H_4 curve (or C_4H_6) corresponding to the just calculated abscissa.

- Draw a half line from the origin and find the intersection with the other curve.

- Calculate the ratio of the two ordinates

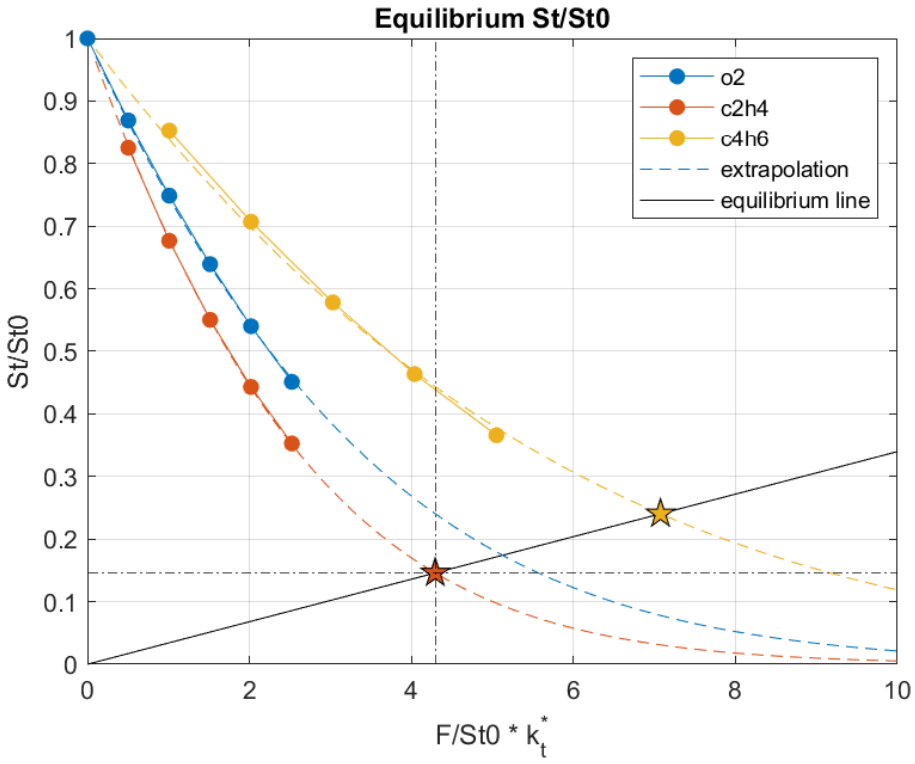

Figure 75. Heat transfer equilibrium, data have been extrapolated using a formula similar to Meinert et al's to reach out of range values

By doing the steps above the calculated F resulted 0.85% and the ratio for test 7 about 1.65, i.e 65% higher regression rate, compatible with the ranges presented in the previous chapters, especially for low values of G in which Carmicino's results fall in.

This method allows to calculate the heat transfer "equilibrium": if we would have gone straight up from the reference point, indeed, we would have reached a point where the the regression rate would have been higher but not corresponded by an increase in $\frac{St}{St_0}$. Being the relation between the latter and the regression rate linear, at every small step up corresponds a small step at the right ($F = \frac{\rho_{inj} v_{inj}}{\rho_e v_e} = \frac{\dot{r} \rho_{fuel}}{\rho_e v_e}$). The size of the second step is such to keep the ratio between x and y of the reference point constant, so all the equilibrium points for the given G stand in a line passing from the origin.

This procedure has been conducted also for other tests, obtaining the following results:

Test	5	7	10	200 N	1	3	12
Fuel	HDPE	HDPE	HDPE	HDPE	HTPB	HTPB	HTPB
$\dot{r}$ ratio	1.55	1.65	1.53	1.38	1.72	1.51	1.61

As we can see this procedure is quite solid for it gives coherent results also for the other cases. As said before, however, this procedure is still affected by some uncertainties and the exact numbers should be taken with a grain of salt.

6 Discussion

The data collected in this work show a strong correlation between $\frac{\rho_{inj}}{\rho_{stream}}$ and $\frac{C_f}{C_{f0}}$. This effect, as said before, could be the missing phenomenon that explains the great difference in regression rates between two very similar polymeric fuels such as HTPB and HDPE.
Many other factors, however, could have also contributed to the difference observed in the last chapter, for example:

- **effective vaporization enthalpy**: Since reliable and complete data about the h_v of HTPB have not been found in this work it has been taken as the same of HDPE. In reality it is probably a bit lower, which in turns raise the $\dot{r}$ (1.2).

- **Fuel densities**: The HTPB has a slightly lower density ($930\,kg/m^2$ vs. $960\,kg/m^3$ of HDPE), which increases the regression rate given the same amount of transferred heat flux (again from 1.2).

- **Radiative phenomena**: As said multiple times, HTPB shows higher soot production which increases the heat flux to the fuel grain. This was not taken into account however in the simulations with combustion so the effect shouldn't have contributed to the observed overall regression rate.
  Moreover the radiation is significant for uncommon operative condition (high pressures and low G (**Fig. 7**).

- **Particulate**: Particulate has another effect besides emitting thermal radiation: since its composed of solid particles it does not count in the blocking effect, making some fuels that already contain it burn slightly faster The content of particulate in solid HTPB and HDPE is generally negligible however, so this effect shouldn't be relevant.

Although these factors could seem to be strong enough to account for the searched difference, we didn't take into account the negative feedback blocking effect that flattens out all these contributions to much less than $1.5 \div 2$ on the regression rate.

In this study we explored the hypothesis claiming that the density of the injected gas over the stream one could have significant impact on the boundary layer shape and wall friction coefficient. Two reasons could be raised at his point: the variation of density along the boundary layer alters the transfer of momentum from the free stream to the wall, leading to greater C_f as claimed by Chiaverini and Kuo [14], or given a fixed mass flux the literal injection of lighter substances thickens more the boundary layer and move further the flame. This last hypothesis come from the following equation:

$$\dot{w} = \dot{r}\,\rho_{fuel}\,v = \frac{(\rho_{inj}\,v_{inj})}{\rho_{inj}} = v_{inj}$$

Which shows that the volumetric flux is exactly the velocity of the injected gas (v is the specific volume). The denser the substance, the less volumetric flux will produce and consequently less blowing will be perceived by the main stream.
From all the conducted analyses, however, we haven't been able to estimate the relative importance of an effect with respect to the other.

Both theses lead to several conclusions and predictions:

- **Molecular mass of injected gas**: the main effect explored in this study. As said multiple times molecular mass is correlated by the ideal gas equation to the density, so high molecular mass gases are heavier and viceversa. Fuels that decompose in heavier products are expected to have higher regression rates.

- **Main stream temperature**: Another effect explored in this work. High stream temperature raises the density ratio $\frac{\rho_{blowing}}{\rho_{stream}}$, making the perceived blown gas density higher.
  As studied in non-isothermal and combustion simulations, heating up the main flow resulted in high $\frac{C_f}{C_{f0}}$ or regression rates.

- **Wall temperature**: Fixing the heat transfer, fuels with low E_a are characterized by more variable surface temperature. In response to an increase in $\dot{Q}$ they tend to heat up more than high activation energy fuels. If the effective vaporization enthalpy increases with temperature (which is true for all fuels), than the dependence between regression rate and heat transfer is sub-linear, lowering the n coefficient of the fuel below the theoretical 0.8 and the overall

combustion velocity (1.2). This effect could be strengthened by the fact that higher surface temperatures lower the density of the injected gas, making it lighter and reducing further the $\dot{r}$.

- **Particulate**: It's possible that, on top the reduced blocking effect, the particulate could alter the mean molecular mass of the surrounding gas both raising or lowering it. Being mainly composed by solid agglomerates of heavy atoms which are seized from the decomposition gas, they leave a overall less denser substance. This effect, however, is expected to be relatively small compared to the first two.

- **High pressure**: Due to Le Chatelier principle, high pressure tend to shift the chemical equilibrium of the decomposition reaction towards high molecular mass products and viceversa, making the combustion physics slightly affected by pressure. This phenomenon is also probably more intense for low pressure than for high ones.

- **Liquefying fuels**: Entrainment of paraffin and other liquefying fuels shouldn't happen literally as described in the standard theory since they are supercritical under common pressures inside a combustion chamber, so no free surface or defined boundary exist (no surface tension is present in supercritical conditions). The hypothesis that density of injected gas alters the blocking effect, however, could explain nonetheless their high regression rates. The injected substance is supercritical and much denser than the external flow, producing a much lower blowing.
  Moreover, droplets shouldn't be really composed of liquid, but more likely they are lumps of supercritical vapor that detach from the surface by Kelvin–Helmholtz instability (**Fig. 76**), caused by the shear stress between a fast moving main flow and a relatively stationary fuel layer.
  This phenomenon too could be affected by the density ratio of injected gas over the main flow gas.

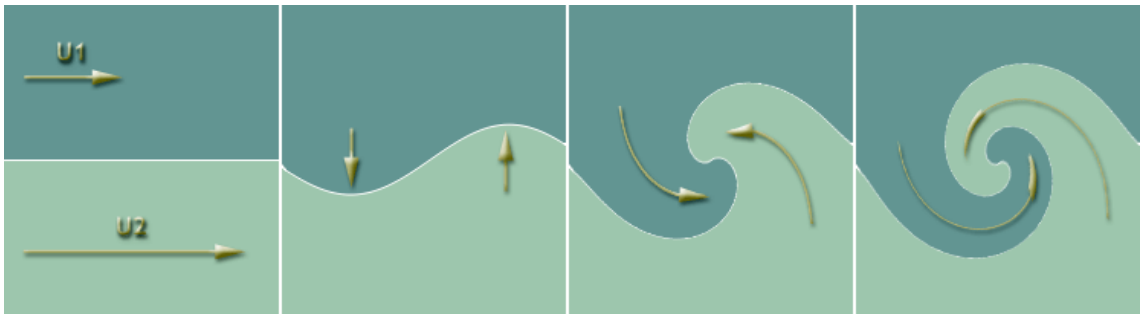

Figure 76. Kelvin - Helmholtz instability. It happens when a steep velocity gradient and an associated high shear stress exists across the boundary of two different fluids

All these phenomena are added to the already big set of physical phenomena that characterize a hybrid motor. A really complete theory should model all of them or at least capture the dependency on the main variables.

7 Conclusion

By employing commercial CFD software (Ansys) we have been able to simulate three increasingly complex cases, whose results show a strong correlation between density difference and wall friction coefficient (which is linked to the convective wall heat transfer). All of the cases have been validated successfully on data already present in literature, obtaining good agreement and raising the reliability of this work.

Cold-flow isothermal and non-isothermal simulations explored the core of the problem without the interference of a complex phenomenon like combustion, while the rocket simulations correctly modeled the internal gasdynamics of a hybrid motor and pyrolysis of a HTPB or HDPE-based fuel, which ultimately showed that CFD can capture this phenomenon in play in such conditions too.

Side analyses have also been conducted, to assure that the effect is present also in other conditions such as variable stream temperature and different main flow chemical species.

In this work a correction to Paul et al. work based on the collected data has been presented too, allowing in the future to continue this path and eventually find a good and simple expression for the effect to be integrated in the classical theory.

Finally in the discussion section a summary of the other possible explanation is listed and discarded since they hardly account for all the observed effect. This section than proceeds identifying several testable prediction for the density effect, which could be the topic of future works

Bibliography

[1] F. Barato. “Numerical and Experimental Investigation of Hybrid Rocket Motors Transient Behavior”. PhD thesis. Università degli Studi di Padova, 2013.

[2] Nicolas Bellomo et al. “Numerical Investigation of the Effect of a Diaphragm on the Performance of a Hybrid Rocket Motor”. In: *46th AIAA/ASME/SAE/ASEE Joint Propulsion Conference & Exhibit*. 2010, p. 7033.

[3] C. Carmicino. “Alcuni aspetti della balistica interna di un endoreattore a propellenti ibridi e del comportamento di ugelli a spina troncata”. PhD thesis. Università degli Studi di Napoli Federico II, 2002.

[4] Carmine Carmicino and Annamaria Russo Sorge. “Role of injection in hybrid rockets regression rate behaviour”. In: *Journal of propulsion and power* 21.4 (2005), pp. 606–612.

[5] Carmine Carmicino et al. “Basic aspects of the hybrid engine operation”. In: *45th AIAA/ASME/SAE/ASEE Joint Propulsion Conference & Exhibit*. 2009, p. 4937.

[6] Giuseppe D. Di Martino et al. “Computational fluid-dynamic simulations of hybrid rocket internal flow including discharge nozzle”. In: *53rd AIAA/SAE/ASEE Joint Propulsion Conference*. 2017, p. 5045.

[7] Giuseppe Daniele Di Martino. “Experiments and Simulations of Hybrid Rocket Internal Flows and Material Behaviour”. PhD thesis. Università degli Studi di Napoli Federico II, 2018.

[8] *Fluent manual - Continuity and Momentum equations*. URL: https://www.afs.enea.it/project/neptunius/docs/fluent/html/th/node11.htm.

[9] *Fluent manual - Energy equation*. URL: https://www.afs.enea.it/project/neptunius/docs/fluent/html/th/node107.htm.

[10] *Fluent manual - species transport equation*. URL: https://www.afs.enea.it/project/neptunius/docs/fluent/html/th/node128.htm.

[11] Susane Ribeiro Gomes, Leopoldo Rocco, and José Atílio Fritz F Rocco. “Swirl Injection Effects on Hybrid Rocket Motors”. In: *Journal of Aerospace Technology and Management* 7 (2015), pp. 418–424.

[12] Matthias Grosse. “Effect of a diaphragm on performance and fuel regression of a laboratory scale hybrid rocket motor using nitrous oxide and paraffin”. In: *45th AIAA/ASME/SAE/ASEE Joint Propulsion Conference & Exhibit*. 2009, p. 5113.

[13] *Hyimpulse Technologies*. URL: https://www.hyimpulse.de/en/technology.

[14] Kenneth K Kuo and Martin J Chiaverini. *Fundamentals of hybrid rocket combustion and propulsion*. American Institute of Aeronautics and Astronautics, 2007.

[15] R.B. Landis and A.F. Mills. “The calculation of turbulent boundary layers with foreign gas injection”. In: *International Journal of Heat and Mass Transfer* 15.10 (1972), pp. 1905–1932.

[16] G Lengelle et al. “Condensed-phase behavior and ablation rate of fuels for hybrid propulsion”. In: *29th Joint Propulsion Conference and Exhibit*. 1993, p. 2413.

[17] Timohty Marquardt and Joseph Majdalani. “A Primer on Classical Regression Rate Modeling in Hybrid Rockets”. In: *AIAA Propulsion and Energy 2020 Forum*. 2020, p. 3758.

[18] Jens Meinert et al. “Turbulent boundary layers with foreign gas transpiration”. In: *Journal of Spacecraft and Rockets* 38.2 (2001), pp. 191–198.

[19] Florian R. Menter, Martin Kuntz, and Robin Langtry. “Ten years of industrial experience with the SST turbulence model”. In: *Turbulence, heat and mass transfer* 4.1 (2003), pp. 625–632.

[20] *NIST Chemistry WebBook*. URL: https://webbook.nist.gov/chemistry/.

[21] DD Ordahl and WA Rains. “Recent developments and current status of hybrid rocket propulsion.” In: *Journal of Spacecraft and Rockets* 2.6 (1965), pp. 923–926.

[22] PJ Paul, HS Mukunda, and VK Jain. “Regression rates in boundary layer combustion”. In: *Symposium (International) on Combustion*. Vol. 19. 1. Elsevier. 1982, pp. 717–729.

[23] Daniel Prokein and Jens von Wolfersdorf. “Numerical simulation of turbulent boundary layers with foreign gas transpiration using OpenFOAM”. In: *Acta Astronautica* 158 (2019), pp. 253–263.

[24] P.N. Romanenko and V.N. Kharchenko. “The effect of transverse mass flow on heat transfer and friction drag in a turbulent flow of compressible gas along an arbitrarily shaped surface”. In: *International Journal of Heat and Mass Transfer* 6.8 (1963), pp. 727–738.

[25] Raisa Theba, Kirsty Veale, and Clinton Bemont. “Development of a Combustion Visualisation Hybrid Rocket Motor”. In: *R&D Journal* 33 (Dec. 2017), pp. 97–104.

[26] J.P. De Wilde. “The heat of gasification of Polyethylene and Polymethilmethacrilate”. In: *Delft University of Technology* (1988).

[27] C.E. Wooldridge and R.J. Muzzy. “Measurements in a turbulent boundary layer with porous wall injection and combustion”. In: *Symposium (International) on Combustion*. Vol. 10. 1. Elsevier. 1965, pp. 1351–1362.

[28] C.E. Woolridge and Rae J. Kier. *An investigation of combustion instability in hybrid rockets*. Tech. rep. 1970.

[29] Gregory Zilliac and M. Karabeyoglu. “Hybrid rocket fuel regression rate data and modeling”. In: *42nd AIAA/ASME/SAE/ASEE Joint Propulsion Conference & Exhibit*. 2006, p. 4504.